Wood Microwave Dielectric Heating and Measurement of Material Properties

Morris Rimbi

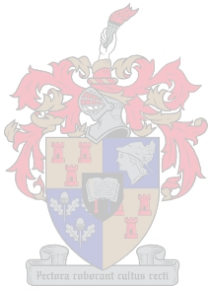

Dissertation presented for the Degree of Doctor of Philosophy
in Engineering at the University of Stellenbosch

Promoter: Prof. H.C. Reader

Date: April, 2004

Declaration: I, the undersigned, hereby declare that the work contained in this dissertation is my own original work, and has not previously in its entirety or in part been submitted at any university for a degree

Abstract

Keywords: *Dielectric property, Dielectric heating, Fixtures, Applicator, Choke, Calibration standards*

Microwave heating technology is extensively used in households, is well-established in certain industries and is being explored in others. Its attraction is that it is quick, energy efficient, clean and can be used to heat materials of both high and low thermal conductivities. Successful application of the technology requires knowledge of both material properties and microwave equipment. Commercial fixtures for measuring dielectric properties are not widely available and are usually created in-house. The domestic oven magnetron is easily available and can be used in prototype microwave systems but applicators for specific applications need development.

This thesis covers three main areas, namely; dielectric measurement fixtures, microwave applicators and chokes, and drying of wood.

The first part of the thesis presents four dielectric measurement fixtures, one commercial and the others in-house. The design and calibration of the in-house fixtures is presented. An intercomparison of the performance of the four fixtures is carried out by measuring the permittivities of well characterised dielectrics: teflon and perspex. The most convenient fixture is used to measure the dielectric properties of wood at different moisture contents.

The second part covers the design of a slotted waveguide fed microwave applicator and a choke. The design of the slotted feed is carried out analytically with and without mutual coupling between the slots. A semi-empirical design using a finite element package is done independent of the analytical approach and the results are compared. The choke is rigorously characterised using a procedure which avoids de-embedding.

The third and last section reports on the wood drying experiments carried out in the applicator, simulated and mapped heating patterns of drying wood, and a mock-up industrial wood drying facility.

Opsomming

Sleutelwoorde: *Diëlektriese eienskap; Diëlektriese verhitting; Toevoeger; Smoorder; Kalibrasie standaarde*

Mikrogolfverhittingstegnologie word wyd gebruik in huishoudings, is goed gevestig in sekere nywerhede en moontlike gebruike daarvan op ander gebiede word gedurig ondersoek. Die vernaamste voordele is dat dit vinnig, energiedoeltreffend en skoon is en dat dit gebruik kan word om materiale van beide hoë en lae termiese geleidingsvermoë te verhit. Suksesvolle toevoeging van die tegnologie vereis kennis van beide materiale-eienskappe en mikrogolf toerusting. Kommersiële apparaat vir die meet van diëlektriese eienskappe is nie wyd beskikbaar nie en word gewoonlik "binnenshuis" ontwikkel. Die huishoudelike mikrogolfoond magnetron is geredelik beskikbaar en kan in prototipe mikrogolfstelsels gebruik word, maar toevoegers geskik vir spesifieke gebruike moet ontwikkel word.

Hierdie proefskrif dek drie hoofgebiede, naamlik: diëlektriese metingsapparaat, mikrogolf toevoegers en smoorders, en die droging van hout.

Die eerste deel van die proefskrif handel oor vier diëlektriese metingsapparate, een kommersiëel en die ander "binnenshuis". Die ontwerp en kalibrasie van die "binnenshuis" apparate word aangebied. 'n Tussenvergelyking van die verrigtinge van die vier apparate word gedoen deur die meting van baie bekende diëlektrikums: teflon en perspex. Die mees gerieflike apparaat word gebruik vir die meet van die diëlektriese eienskappe van hout teen verskillend voginhoude.

Die tweede deel dek die ontwerp van 'n smoorder en 'n mikrogolf toevoeger wat deur 'n gegleufde golfgeleier gevoer word. Die ontwerp van die gegleufde golfgeleier word beide met en sonder wedersydse koppeling tussen die gleuwe, analities gedoen. 'n Semi-empiriese ontwerp wat van 'n eindige-element pakket gebruik maak, is onafhanklik van die analitiese benadering gedoen. Die resultate word dan vergelyk. Die smoorder word deur 'n prosedure wat "de-embedding" vermy, streng gekarakteriseer.

Die derde en laaste afdeling behandel die eksperimentele droging van hout binne die toevoeger. Simulasies en verhittingspatrone van die hout wat gedroog word, sowel as die "mock-up(model van die voorgestelde)" nywerheids houtdroogkamer, word gegee.

Acknowledgements

Many people have contributed in various ways to this dissertation. I would firstly like to express my sincere gratitude to Prof. H.C Reader, my supervisor, for his bravery in taking me as his student, guidance and encouragement through the course of this study.

To Prof. J.de Swardt for writing the data logging program, Prof. H. Vermaas and Dr. D.Steinmann of the Wood Science department for various discussions, supplying wood and making available their laboratories and equipment.

On the technical front, my gratitude goes to Wessel Croukamp, Urich Buttner of SED for manufacturing the fixtures, applicator and choke used in this study. Wilmour Hendrikse of the Wood Science department for helping in the preparation of the wood samples.

To colleagues I shared room E212 with for providing a conducive working environment.

Finally, to Hilary, Mary and Patricia, mwakaita basa, kutenda kwakitsi kuri mumwoyo.

Contents

List of Figures

List of Tables

Chapter 1

INTRODUCTION

The electromagnetic spectrum is and has been widely studied, researched and utilized. We all use or benefit from the use of electromagnetic energy in one form or the other, from medical diagnosis through communication, sensing (including seeing) to heating. The spectrum is so widely used that regulations and laws have been gazetted by governments and professional bodies to allocate frequency bands and monitor adherence to them [1]. Research has produced innovative applications in the industrial, scientific and medical (ISM) fields.

The ISM uses of radio-frequency (RF) and microwaves have been described by several authors including [1][2]. The multitude of applications is a result of an understanding of the propagation of electromagnetic waves and their interaction with matter. The macroscopic behaviour of the waves is, for most purposes, modelled by Maxwell's equations and the constitutive relations. Solving Maxwell's equations is fundamental to the study of electromagnetics on which many books have been written.

In this dissertation, the RF and the microwave regions of the electromagnetic spectrum are studied from the most elementary of applications - drying wood. Human beings have always heated things and have experimented with different sources and methods such as fire, solar, nuclear, induction and microwave heating.

Microwave (MW) dielectric heating has been actively investigated over the past few years by several researchers including the electro-heating group at the University of Stellenbosch. The electromagnetic field distribution in loaded and unloaded microwave applicators has been the subject of a recent PhD [68]

It was then decided to extend the available knowledge to applicators for heating dielectrics such as wood. The wood interest led to consultations with Wood Science academics in the Forestry department of the University of Stellenbosch and a wide review of wood drying literature. Through the reading and the consultations, it emerged that:

- the wood industry has and is still searching for a fast and reliable high technology technique for drying wood and measuring the moisture content during the drying process [72]
- studies have been conducted on RF, RF with vacuuming (RFV) and combinations of RF and conventional drying of mostly softwoods. Only one near-commercial scale RFV system was reported in the 90s [89-90]. It uses a capacitive arrangement of metal electrodes to launch RF energy generated by a triode oscillator. It is necessary to explore other methods of launching RF and MW energy into applicators.
- moisture meters have been designed, built and commissioned but their performance in determining wood moisture content has been described by one wood science researcher as "unreliable". Fast and reliable online moisture meters are highly sought after by the wood industry.

- models of RF and MW induced drying processes have been developed and simulated but hardly validated experimentally.

Addressing some of the above issues requires an understanding of dielectric properties of materials, microwave applicators and the interaction of electromagnetic energy with dielectrics. The objectives of this study are to

- develop and investigate fixtures for measuring the dielectric properties of anisotropic materials such as wood.
- develop a microwave system for drying wood in an industrial environment
- relate the wood-drying process to the dielectric properties.

An overview of the theoretical and practical work undertaken in the study of microwave dielectric heating follows:

Chapter 2: Fixtures for measuring dielectric properties.

Four fixtures: Marconi jig, stripline fixture, open-ended coaxial probe and the waveguide system are used to measure the dielectric properties of the same samples. This is aimed at comparing the performance and suitability of each fixture for the measurement of the dielectric properties of wood.

A panel mount SMA female connector is modified to make a coaxial probe. The calibration kit of the coaxial probe is new. The design of the stripline fixture is original and the algorithm used to process the stripline acquired data is a novel adaptation of a widely accepted method.

Chapter 3: Design of a slotted waveguide feed for a microwave applicator.

A slotted waveguide feed for a microwave applicator is designed using an analytical method and a finite element (FEM) computer package. The analytical design is carried out with and without mutual coupling. Though based on well established theory and design procedures for slots on the broadside of a rectangular waveguide, the design is unique. The procedure is shown to produce slot offsets and lengths which are comparable to those obtained by Elliott [51] and independently through the FEM package.

Chapter 4: Waveguide-fed microwave applicator.

A microwave applicator fed by two slotted waveguide feeds and with several operational options is characterised. One of the options is the use of an open-ended choke. The performance of the choke in a working environment is measured using a technique which is largely original.

Chapter 5: Wood drying and moisture content measurement.

Dielectric properties of wood at various moisture contents are measured using a stripline fixture. This is the first time that the material properties of wood at different moisture contents have been measured over a wide frequency range using a stripline fixture connected to an automatic network analyser (ANA). The properties are used to simulate electromagnetic field patterns and

therefore, heat and moisture distribution in wood as it dries. The simulated patterns are compared with experimentally obtained fax paper patterns.

Drying schedules for wood are established and an industrial continuous wood drying process using combined microwave and air at various temperatures is demonstrated. The wood is inspected visually and its moisture content measured gravimetrically in between drying runs.

Chapter 6: General conclusions and recommendations.

Chapter 2

Fixtures for Dielectric Property Measurement

2.1 Introduction

Permittivity values of materials have been measured in the frequency and time domains [3][4][5] and used to infer the interaction of RF and microwaves with many materials, notably, biological [3][6][7] and geological materials [8] since the 1940's. Reviews have been published on the measurement techniques for permittivity in biological systems [3][7][9][10] and measurement techniques in general[48]. The most commonly used methods in the RF and microwave regions utilise various fixtures ranging from open-ended coaxial lines [6][10][11][12], coaxial transmission lines [5][6][13], rectangular waveguides [14], striplines [15], capacitive plates [16], cavity resonators and free space [37]. The strengths and limitations of each method are widely reported in the literature.

In this chapter, the use of a capacitive plate, a coaxial probe, a waveguide system and a stripline system in dielectric property measurements are examined. The design of a new stripline fixture and a calibration kit for an open-ended coaxial probe are presented. The fixtures are tested against each other by using them to measure the permittivities of well studied dielectric materials: teflon and perspex. The samples used with each fixture are from the same batch. Their dielectric properties can therefore be assumed uniform.

2.1.1 Permittivity

Complex permittivity and permittivity have been defined in various ways in the literature. Zhang et al.[42] define the complex permittivity ε^* by

$$\varepsilon^* = \varepsilon' - j\left(\varepsilon'' + \frac{\sigma}{\omega\varepsilon_o}\right) \tag{2.1}$$

where ε' is the real part of the complex permittivity. It represents the ability of a material to store electromagnetic energy.

$\left(\varepsilon'' + \frac{\sigma}{\omega\varepsilon_0}\right)$ is the effective dielectric loss factor. It is a measure of the material's ability to transform microwave energy into heat.
σ is the electrical conductivity.
ω is the radian frequency.
ε_0 is the permittivity of free space.

For dielectric materials, the conductive term in equation (2.1) is negligible, in which case $\varepsilon^* = \varepsilon$. It is on this assumption that the

- terms complex permittivity and permittivity are used interchangeably in dielectric literature.
- permittivity is often defined as

$$\varepsilon = \varepsilon' - j\varepsilon'' \tag{2.2}$$

It should be noted that Zhang et al. used a positive sign for the imaginary part, however, the convention used in equations (2.1) and (2.2) is more widely used.

Also commonly used is the relative permittivity ε_r defined as

$$\varepsilon_r = \frac{\varepsilon}{\varepsilon_o} \tag{2.3}$$

Thus equation (2.2) can be written as

$$\varepsilon_r = \varepsilon_r' - j\varepsilon_r'' \tag{2.4}$$

The r subscript is often dropped resulting in equations (2.2) and (2.4) looking the same with parameters described differently, a great source of confusion adding to that caused by referring to both ε and ε' as permittivity. In this dissertation, the term real part of permittivity is used to describe ε'.

Equation (2.2) in the form $\varepsilon = \varepsilon' - j\varepsilon''$ is used throughout this dissertation. The imaginary part of the complex permittivity, ε'', is referred to as the loss factor and the ratio of loss factor to permittivity is called the loss tangent.

2.1.2 Dielectric Measuring Systems

Four dielectric measuring fixtures: one commercial and three fabricated for this project at the University of Stellenbosch are used to measure the dielectric properties of teflon and perspex. The fixtures have different structures, principles of operation and geometrical requirements for the samples. These differences might manifest themselves as different values of some of the measured properties but would not hinder comparison.

Each fixture measurement system will now be described in turn, starting with the Marconi capacitive fixture in Section 2.2

2.2 Marconi Dielectric Test Set

Of all the abovementioned dielectric measurement fixtures, the capacitive plate is probably the simplest in design, construction and use. A capacitive plate fixture is usually realised using either rectangular plates or disc plates. Disc plates are preferred because they are free from the corner effects which are present in rectangular plates [16, pp 247].

The Marconi dielectric test set is a precision instrument for measuring the permittivity of dielectrics in the frequency range 0.04 - 50.00 MHz.

The major parts of the test set are a 0.04 - 50.00 MHz type TF 1246 oscillator and a type TF 1245 circuit magnification meter. Figure 1.1 is a picture of the set.

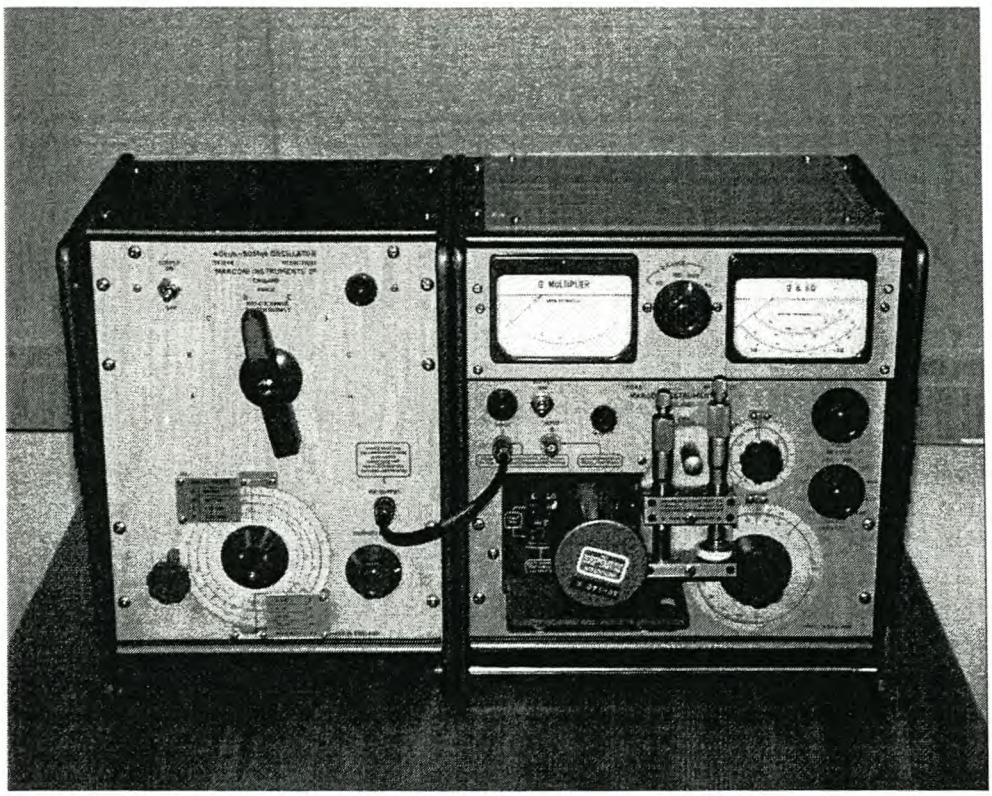

Figure 2.1 Marconi dielectric test set.

The test set also includes a kit of tuning inductors and a dielectric test jig. The inductors covering the 0.02 - 50.00 MHz frequency range are used for resonating the circuit. The test jig consists of two micrometer capacitors: a parallel disc plate capacitor for holding samples and a cylindrical linear law capacitor with a very small capacitance range. The small range capacitor is used as a vernier for measuring the sharpness of resonance of the tuned circuit. The edges of the electrodes are bevelled to reduce fringing.

2.3.1.1 Measurement of Permittivity Using the Marconi Test System

The Marconi test system has certain geometrical requirements for the test materials. The preparation of the samples is covered in Section 2.3.1.1.1, the measurement procedure and analysis of measured data is given in Section 2.3.1.1.2.

2.3.1.1.1 Preparation of specimen

Disc specimens of a diameter slightly greater than those of the capacitive plate circular electrodes are prepared. The size of the specimen is made larger than the electrodes in order to reduce fringing errors. For accurate results, a sample thickness of 1-5 mm is recommended [44].The available machining resources allowed a minimum thickness of 5 mm only. Therefore, samples of a thickness of 5 mm are used in these measurements. The surfaces of the plates are made as flat as possible in order to reduce the air gaps between sample and electrodes. Air gaps reduce the measured capacitance and therefore lead to inaccuracies in the dielectric properties.

2.3.1.1.2 Measurement procedure

The measurements are carried out as follows:

- oscillator frequency is set to a desired value.
- inductor of a frequency range which includes the set frequency is plugged into the TF1245.
- linear law incremental capacitor is set to half its range, the 12.50 mm point.
- sample is placed between the plate electrodes using a pair of forceps and the micrometer is screwed down until a tight grip is confirmed by the ratchet. To ensure repeatability in the contact between sample and electrodes, the position of the sample relative to the electrodes is marked.
- thickness of the sample, d_1, is read on the main capacitor vernier scale.
- Q - meter is zeroed.
- TF 1245 main (large dial) and vernier (small dial) capacitors are tuned for resonance.
- resonance is fine tuned by adjusting the linear capacitor for maximum deflection of Q-meter
- deflection, Q, of Q-meter is read.
- linear law capacitor is moved in a clockwise direction until the Q-meter reads 0.5Q and then anticlockwise until Q-meter reads 0.5Q. The difference between these readings is designated m_1
- resonance is restored by adjusting the linear law capacitor back to its resonance reading.
- specimen is removed and an air capacitor remains.
- air capacitor is adjusted for resonance and its thickness d_2 is read.
- air capacitor resonance Q-meter reading is taken.
- linear law capacitor is detuned clockwise and anti-clockwise as in the case with the sample. The difference between the clockwise and the anti-clockwise readings is m_2

A new frequency is set and the procedure is repeated.

2.3.1.1.3 Calculation of ε′ and ε′′

The real part of the permittivity is given by [44]

$$\varepsilon' = \frac{C_2 + C_{F2} + C_{F1}}{C_1} \tag{2.6}$$

where

$C_2 = 4.48/d_2$ is the capacitance with a sample of thickness d_2.
C_{F2} is the effective fringing capacitance when the separation of the disc electrodes is d_2.
$C_1 = 4.48/d_1$ is the capacitance when electrode separation is d_1.
C_{F1} is the effective fringing capacitance when the separation of the electrodes is d_1.

The loss tangent of the samples is given by

$$\tan\delta = \frac{0.09376(m_1 - m_2)}{C_2 + C_{F2} - C_{F1}} \tag{2.7}$$

from which

$$\varepsilon'' = \frac{0.09376\varepsilon'(m_1 - m_2)}{C_2 + C_{F2} - C_{F1}} \tag{2.8}$$

The fringing capacitance terms can be obtained from the manufacturer's correction graph shown in Appendix 2A. Data sourced from the graph was applied to a MATLAB second order polyfit function to produce

$$C_{Fi} = 0.0023d_i^2 - 0.0676d_i + 0.4576 \tag{2.9}$$

A spreadsheet was then used to calculate the real and the imaginary components of the complex permittivity. Figures 2.2 and 2.3 are plots of ε′ (real) and ε′′ (imaginary) for teflon and perspex respectively. In the interest of detail, the real and imaginary parts have been plotted on different scales.

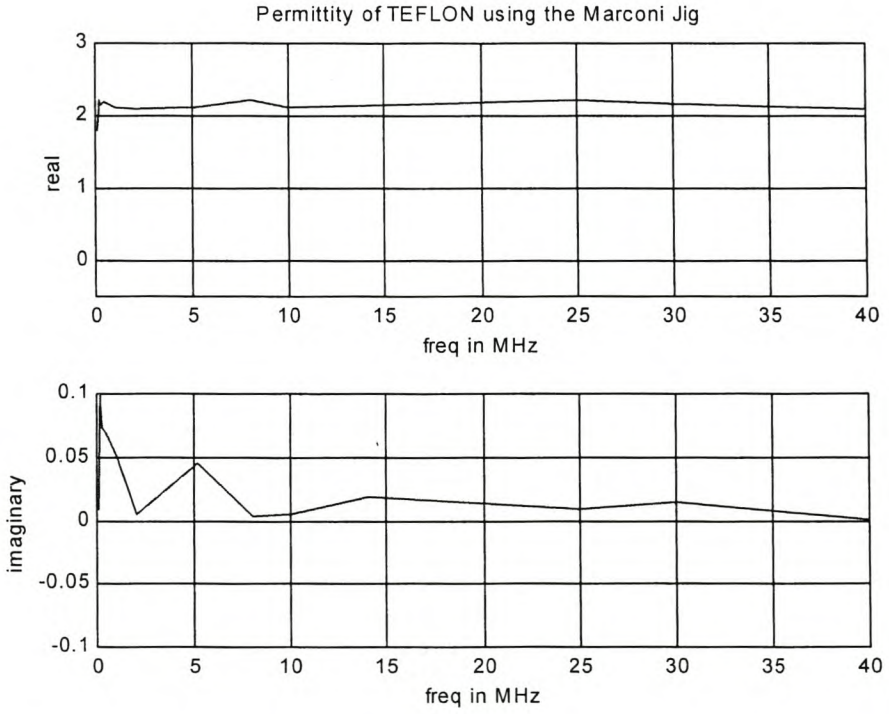

Figure 2.2 Permittivity of a 5 mm disk of teflon as measured with the Marconi jig

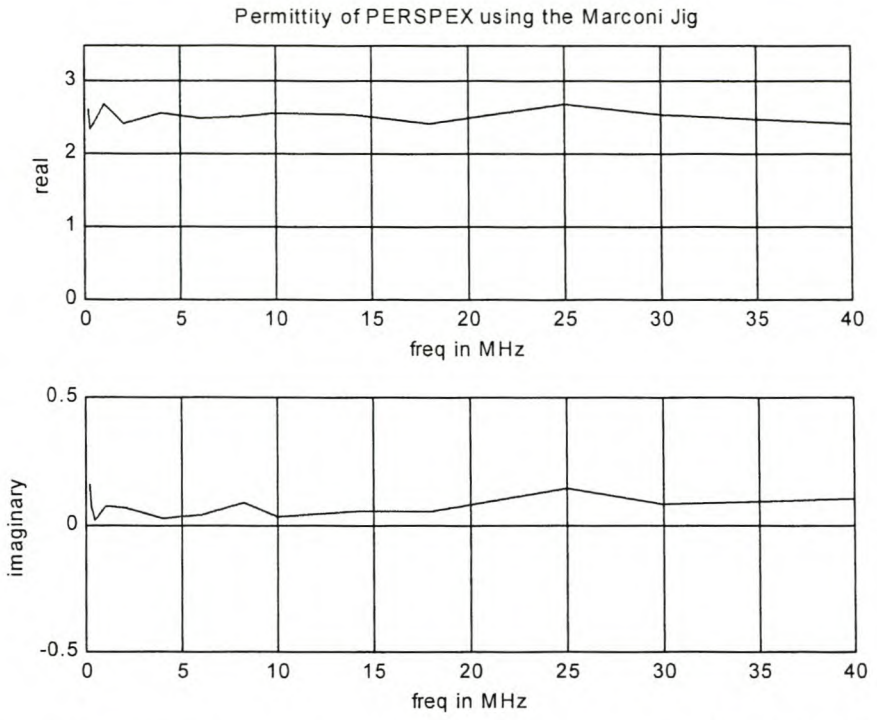

Figure 2.3 Permittivity of a 5 mm disk of perspex as measured with the Marconi jig

Dielectric property values are usually quoted in the literature [30][43] in terms of ε' and $\tan\delta$. It was therefore necessary to calculate $\tan\delta$ from the measured ε' and ε'' in order to facilitate comparison. The measured (average) and reported [43] dielectric values in the frequency range 5 to 35 MHz are compared in Table 2.1.

Table 2.1 Comparison of Marconi measured (averaged in the range 5 to 35 MHz) and reported values for teflon and perspex [43]

Material	ε' (measured)	ε' (reference)	$\tan\delta$ (measured)	$\tan\delta$ (reference)
Teflon	2.1	2.1	0.0027	< 0.0002
Perspex	2.6	2.6	0.0108	0.0300

From Table 2.1, it can be concluded that the real part is more accurately determined with the Marconi jig than the imaginary part.

From Section 2.3.1.1.2, it is clear that the Marconi jig is not a continuous measuring system. Discrete frequency ranges and frequencies are selected on the oscillator and appropriate inductors are plugged in for tuning. The lack of flatness in the plots can be attributed to these operational

characteristics of the system and measurement errors. The sources of error can be identified as

- air gaps between sample and electrodes.
- resolution of Q-meter.
- resolution of vernier scales.
- use of samples of 5 mm thickness.

Repeatability of contact between sample and electrodes was ensured by marking the position of a point on the sample relative to a position on the electrodes.

2.4 The Coaxial Probe

Open-ended coaxial probes have been used to measure dielectric properties at radio and microwave frequencies by Stuchly et al. since the 1970's [7]. Many constructions have been reported in the literature using various types and sizes of coaxial cable. The two major variants can be summarised:

- a small length (about 50 mm) of semi-rigid coaxial cable machined flush and polished with a piece of cloth [3][6][18][19]. A high quality connector is placed at the other end. The general structure is shown in Figure 2.4(a).
- a structure with a flange on the outside [10][11][19]. The flange serves as an extended ground plane for the fringing field and also as a support for the material under test [12].The basic structure is shown in Figure 2.4(b).

(a) basic coaxial probe (b) coaxial probe with a flange

Figure 2.4 Geometries of coaxial probes

The probe used in this investigation is made by machining the centre conductor and the PTFE (teflon) dielectric of a female SMA 50 ohm receptacle panel mount connector so that they are flush with the flange. Conversion of a panel mount connector into a coaxial probe has not been seen in the accessed literature. The probe is of similar structure to figure 2.4(b) and is shown in Figure 2.7.

2.4.1 Models of the Open-ended Coaxial Probe

When high frequency energy is launched into the probe, a fringing quasi-TEM electromagnetic field is formed in the probe dielectric and in air as shown in Figure 2.5(a). The determination of the probe fringing fields using various experimental and mathematical formulations, ranging from lumped element[6][11][18][21] to sophisticated full wave formulations [22][23], has been the

subject of many publications.

The lumped parameter model is widely reported [6][10][18][21]. It consists of two parallel capacitors, C_o which represents the fringing field in air and C_f, which represents the field in the probe dielectric and the resistance R which represents the radiation losses. The field pattern and the equivalent circuit model are shown in Figure 2.5.

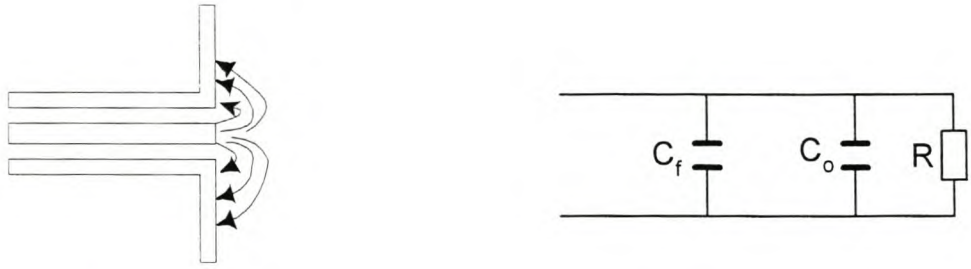

(a) schematic view indicating fringing field pattern

(b) electrical equivalent circuit

Figure 2.5 Fringing field and lumped parameter model of coaxial probe

The admittance of the probe in Figure 2.5 is given by [10][19] as

$$Y_o = j\omega\left(C_f - C_o\right) \tag{2.10}$$

where Y_o is the admittance of the unloaded probe
ω is the radian frequency

According to Stuchly and Stuchly [7], the resistance R, can be ignored if the ratio of the radius of the probe centre conductor to the wavelength is less than one. This is the case in the following probe experiments.

When the probe is loaded with a sample (material under test - MUT) the sample will absorb some of the signal and reflect the remainder. The amount of absorption and reflection depends on the electrical characteristics of the sample and the extent of the fringing field in front of the probe. The reflection coefficient or the admittance of the loaded probe is then measured using an ANA. The lumped parameter electrical equivalent circuit of a loaded probe [10][19] is shown in Figure 2.6.

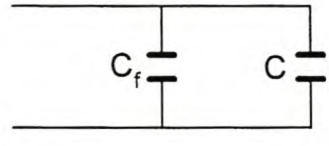

Figure 2.6 The lumped parameter model of a loaded coaxial probe

The admittance of the loaded probe Y_L is given by [10][19] as

$$Y_L = j\omega(C_f + \varepsilon_r^* C_o) \tag{2.11}$$

To remove the $j\omega$ terms from the admittances of the probe and get the capacitance ratio, equation (2.11) is divided by (2.10) to give

$$\frac{Y_L}{Y_o} = \frac{j\omega[C_f + \varepsilon_r^* C_o]}{j\omega(C_f + C_o)}$$

$$= \frac{1 + \varepsilon_r^* \frac{C_o}{C_f}}{1 + \frac{C_o}{C_f}} \tag{2.12}$$

In using equation (2.12) to determine the capacitance ratio, it is assumed that ε_r^* is constant. This assumption is the major weakness of the model. A different approach was used by Grant et al. [10] in their critical study of the open-ended coaxial probe. They concluded that the fringing capacitance as given in the lumped parameter model is only approximate and the model fails at higher frequencies. They attributed the failure of the model to the complicated dependence of the fringing capacitances on the frequency, sample permittivity and loss. Misra [18] attributed the failure to the development of higher order modes and radiation effects. Raicu [3] carried out an experiment to determine the effect of the fringing field on the accuracy of measurements by immersing the end plane of the probe at various distances from the liquid surface. The only significant dependence of the calculated capacitance and conductance on distance, was observed with distilled water. This review shows that there is no widely accepted method for determining the capacitance ratio.

Another issue of concern when measuring solid samples with the probe is that of probe-sample contact. The solid sample must be as flat as possible. Arai et al. [25] studied the effect of sample flatness (or roughness) and they found that a roughness of less than 0.5 μm was necessary for accurate complex permittivity measurements using a coaxial probe. A flat surface is needed to minimise the air gap between the probe and the solid sample [12][24]. Barker-Jarvis et al. [20] modelled in detail the air gap problem. They arrived at the same conclusion. Ideally there should be no air gap. Special attention was paid to minimise the air gap during measurements presented in this study. This was achieved by clamping two opposite flanges of the probe to the sample using purposefully designed nylon clamps.

2.4.2 Probe Calibration - Review

Before a probe is used in a measurement it must be calibrated. Calibration is done in order to remove systematic uncertainties. Two calibration methods are widely used:

- calibrating at the end of a test cable using the HP-ANA one port calibration procedure and kit, then connecting the probe and establishing the reference plane by shorting the end of

the probe with a foil of conducting material as described by [18]. A variant of this procedure involves a one port calibration at the end of connecting cable and then computationally rotating the calibration plane to the measurement plane of the probe.

- calibrating at the end of the probe using the following standards:
  open: measurements are made in air [18][24]
  short: a conducting foil such as aluminium is pressed on the end of the probe [3][18][24]
  load: the probe is dipped in a liquid with well characterised dielectric properties such as de-ionised water [7]

Stuchly et al. [6] used the second calibration method. Misra [18] then simulated errors due to such a calibration procedure, found them to be minimal and concluded that the procedure is satisfactory. However, Otto and Chew [11] pointed out that the use of a material standard in the second method leads to too many source errors due to the imperfection of the standards themselves (the properties of the standards are not accurately known). They, therefore, suggested the use of a short, open and short cavity termination as the load. They claim that the use of the cavity as the load results in a better calibration because it relies "only on the geometry of the probe". Their results were not very different from those obtained when a material standard was used.

The reference liquid problem is also discussed by Evans and Michelson [19]. They propose the use of a large number of reference materials, the properties of which must be obtained from many independent sources in the literature. The calibrations can then be averaged and used for error correction when measuring a sample. They justified the multi-reference point calibration procedure by formulating a linear model equation for the process and solving it using a least squares method.

With no satisfactory calibration standards for the probe available, a decision was taken to make some. Initial thinking was to calibrate at the probe face. This led to the fabrication of the following novel calibration kit:

- short: the probe is screwed on a machined brass block as shown in Figure 2.7. The brass block was made maximally flat for minimum air gap when connected to probe.
- load: A 50 ohm load was placed in a tight fitting hole machined in a brass block as shown in Figure 2.7. The load structure was then machined so that it is flush with the brass block. For calibration, the block is screwed on the block in the manner of the short. The contact pressure between the inner conductor of the probe and that of the load is further maintained by the spring on which the load rests (spring is not shown in the diagram).
- open: measurements are made in air

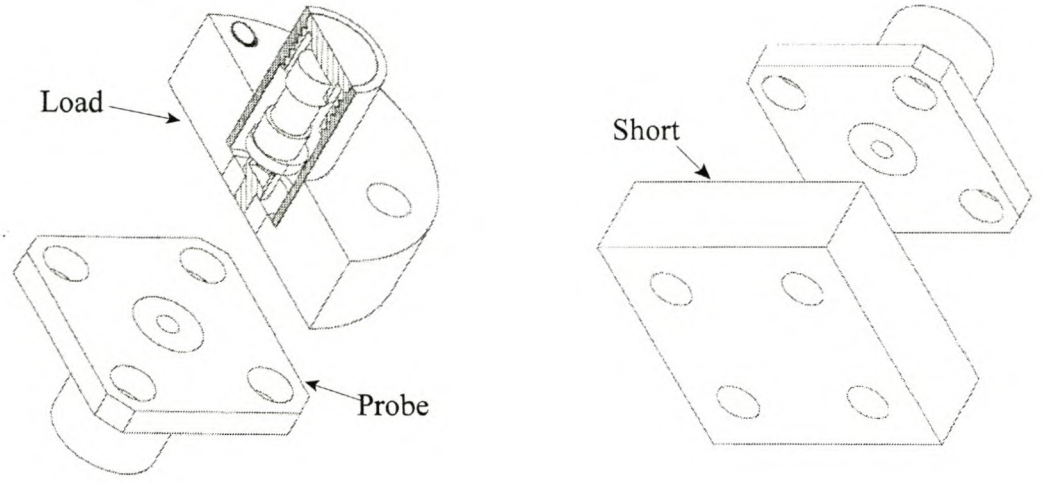

Figure 2.7 Connection of probe to new load and short calibration standards

2.4.3 Specification of the New Probe Calibration Standards for the HP8510C ANA

Before calibrating the ANA using the standards, the parameters of the standards must be specified in the ANA's software. The default values of a coaxial load were used. The short was assumed to be perfect, so the inductances were entered as zero. In the first instance, the open was also defined in the ANA as perfect.

Post-calibration plots on the Smith chart appeared to validate the specifications of the standards as can be seen in Figure 2.8. (A linewidth of 7 was used for the plots in the Matlab code in order to distinguish the plotted points from the lines of the Smith chart).

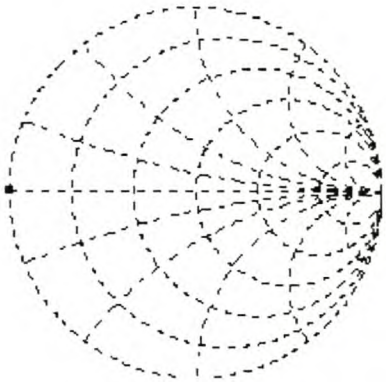

(a) short

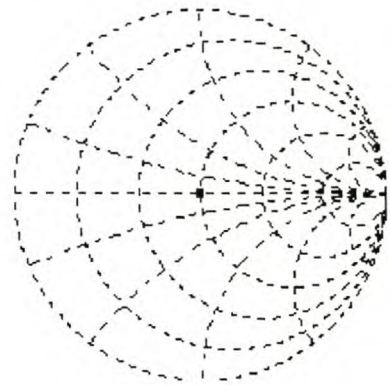

(b) load

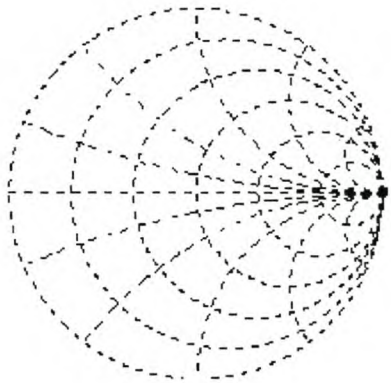

(c) open

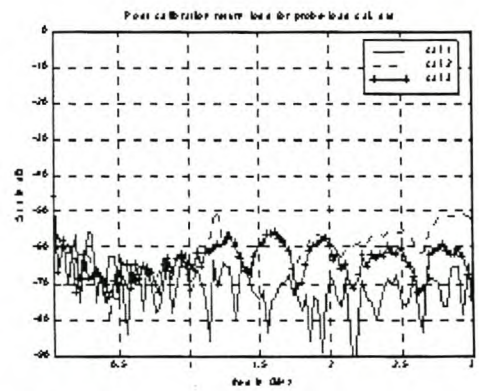

(d) magnitude of return loss of load standard

Figure 2.8 Post-calibration magnitude and phase of standards as seen on the Smith chart and a clearer view of return loss of load

The return loss of the load is 50 dB down throughout the measurement band. The fixed nature of the single load limits the return loss to 20 dB higher than the 70 dB down of commercially available coaxial calibration kits such as the 3.5 mm HP-85052B. The post-calibration loss measured on three matched loads gave a worst case difference of 30 dB. This variation can be attributed to the manufacturing tolerances of the load resistor which had a nominal value of 50 Ω. The spring nature of the pin contact of the load can also limit the return loss of the matched load.

Interest in the new calibration standards was generated at NIST by my promoter. Michael D. Janezic, a reseacher at NIST who was among a team that developed a code for a coaxial probe offered to run the data measured using the probe. The results indicated a phase ambiguity which was eventually traced to the capacitances entered for the open standard.

Using the physical geometry and material specifications of the probe and the measured data, Janezic used the NIST code to generate the expected S-parameters of the open standard. From the NIST predicted S-parameters, a phase response of the open standard was obtained.

The effective fringing capacitance C_o was obtained from the phase response using the equation given in [95] as

$$C_o = \frac{\tan\left(\frac{\phi}{2}\right)}{2\pi f Z_o} \tag{2.13}$$

where φ is the phase angle
f is the frequency

The fringing capacitance as a function of frequency was deduced from [95] to be

$$C_o = c_3 f^3 + c_2 f^2 + c_1 f + c_0 \tag{2.14}$$

where c_i is the capacitance to be entered into the calibration kit

A MATLAB polyfit function was used to obtain the coefficients which were then entered in the ANA.

2.4.4 Measurement of Permittivity Using the Calibrated Probe

As soon as calibration is complete, the response of the probe (open standard) followed by samples of interest are measured. This is done to ensure that the fringing field seen by the MUT is as modelled by the effective capacitance. The post-calibration S-parameters of the probe are used in equation (2.13) to calculate C_o. Several procedures for finding C_o have been reported, some of which can be found in [26][47]and [94].

The real and the imaginary parts of the permittivity of measured samples are obtained from functions given by Stuchly and Stuchly [7] as

$$\varepsilon' = \frac{2S_{11}\sin(-\phi)}{\omega Z_o C_o (1 + 2S_{11}\cos\phi + S_{11}^2)} - \frac{C_f}{C_o} \tag{2.15}$$

$$\varepsilon'' = \frac{1 - S_{11}^2}{\omega Z_o C_o (1 + 2S_{11}\cos\phi + S_{11}^2)} \tag{2.16}$$

C_f is obtained by subtracting C_o from the total capacitance of the probe, C_T. The total capacitance is deduced from Marcuvitz's [23] equation for the normalised admittance of a coaxial line radiating into semi-infinite space. The equation for the total capacitance is

$$C_T = \frac{8(a+b)}{\omega Z_o \lambda \ln(\frac{a}{b})}\left[\xi\left(\frac{2\sqrt{ab}}{a+b}\right) - 1\right] \tag{2.17}$$

where ξ is the complete elliptical integral of the second kind
a is the radius of the outer conductor of the probe
b is the radius of the inner conductor of the probe
$a/\lambda << 1$ and $b/\lambda << 1$,
Z_o is the characteristic impedance of the line

A MATLAB routine, Appendix 2B, was then used to implement equations (2.15), (2.16) and (2.17). Figures 2.9 and 2.10 are plots of the real and imaginary parts of the permittivity of teflon and perspex respectively.

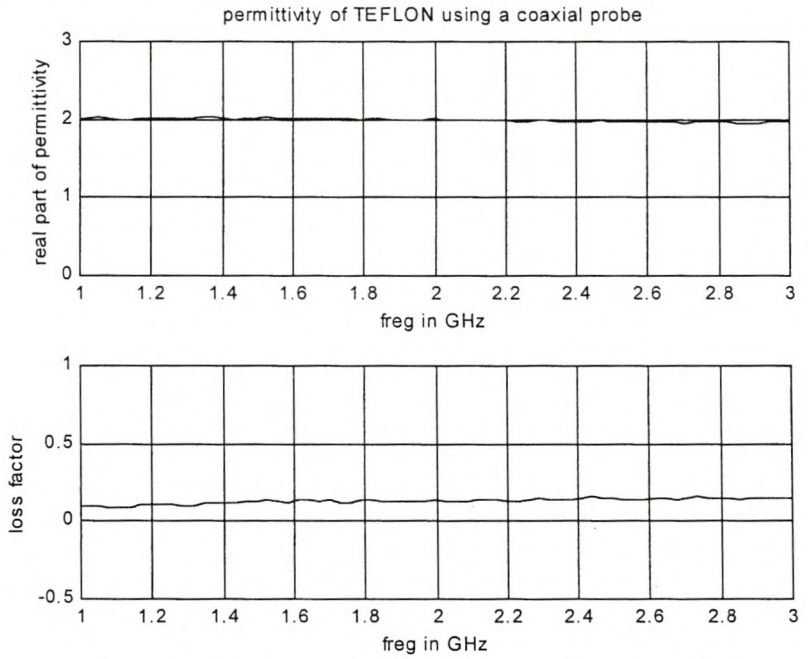

Figure 2.9 Permittivity of teflon as measured by the coaxial probe

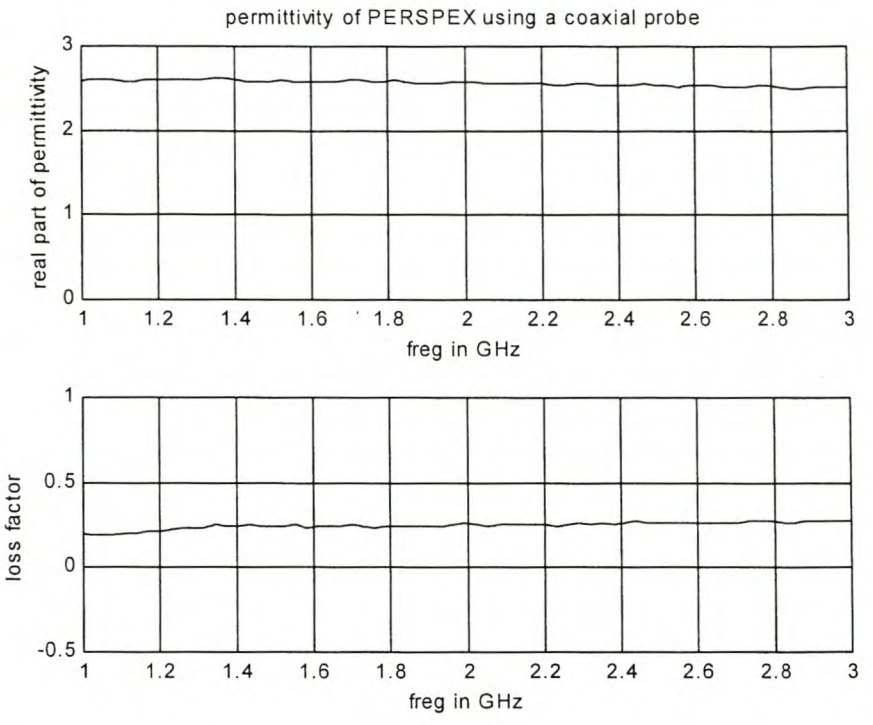

Figure 2.10 Permittivity of perspex as measured by the coaxial probe

As in the case of the Marconi jig, the real and the imaginary parts are plotted on different scales. The average of the measured values taken in the range 1 to 3 GHz, are compared with literature ones in Table 2.2.

Table 2.2 Comparison of probe measured (averaged in the range 1 to 3 GHz) and reported values [43]

Material	ε' (measured)	ε' (reference)	$\tan\delta$ (measured)	$\tan\delta$ (reference)
Teflon	2.0	2.1	0.0625	< 0.0002
Perspex	2.6	2.6	0.096	0.0300

Again, the real part is more accurately determined than the imaginary part. In probe measurements, the low limit in the loss factor is constrained by our inability to model loss accurately in the standards. It is further constrained by contacting problems and the restricted calibration achievable with the springy matched load. The imaginary values do show that teflon and perspex are low loss materials.

2.5 Stripline Fixture

Stripline resonators were developed in the sixties using the principles of stripline design in order to overcome the problems encountered with coaxial transmission line techniques [27] when measuring the dielectric properties of a material sample. The advantages of stripline measurement systems over coaxial and waveguide systems given by Hanson et al. [28] are:

- they are broadband.
- they can be used to infer anisotropic effects by rotating the sample.
- in principle they do not have a cutoff frequency because they maintain a TEM wave.

Their main disadvantage is that there are no commercial calibration standards available. These have to be developed in-house and will be discussed in section 2.5.2.

2.5.1 Design of a Stripline Fixture

There are many methods which can be used in the design of stripline fixtures. Jones et al. [27] used the complete elliptic integral of the first and second kind and Schwarz-Christoffel mapping functions to calculate dimensions of the resonator. They then used perturbation theory to derive expressions for permittivity and permeability. This approach is too complicated for practical implementation, so approximate design equations of a stripline are used. The fixture can be regarded as a blown-up stripline. The approach used in the design of the stripline fixture will now be discussed.

In the design, shown in Figure 2.11, the characteristic impedance Z_0 of the centre-strip is chosen to be 50 Ω. This matches that of the EZ86 semirigid coaxial cable used to connect the fixture to the ANA. The thickness, t, of the brass centre strip is 1.2 mm and the separation of the ground planes, b, is 20 mm. The decision on the 20 mm separation is based on the ease with which prospective dielectric samples would be machined. The 1.2 mm thickness provides enough rigidity to the centre-strip without excessive thickness (and therefore mass) which would otherwise strain the connector-centre-strip junction.

The thickness to separation ratio of 0.06, satisfies the condition for computing the width of the centre-strip using a closed form equation. The condition as given by Cohn [29] requires that the ratio, t to b, is less than 0.25 in order to avoid excessive attenuation. From equations (2.19) and (2.20) below, the effect of the ratio on the impedance and the fringing capacitance of the fixture can be deduced.

The design must also fulfil the condition [30, pp 156]

$$\frac{w_{eff}}{b} = \frac{w}{b} - \begin{cases} 0 \; for \; \frac{w}{b} > 0.35 \\ \left(0.35 - \frac{w}{b}\right)^2 \; for \; \frac{w}{b} < 0.35 \end{cases} \tag{2.18}$$

where w is the width of the centre-strip

w_{eff} is the effective width of the centre-strip.

At this point, either the wide or narrow centre-strip design is chosen. For the wide centre-strip design, the ratio w to b is greater than 0.35. This is chosen because the resulting strip is more easily fabricated and the design expressions are widely accepted [40]. The Z_0 equations have been given in several alternate forms [31][41]. The version due to [31] is more compact and is, therefore, presented in equations (2.19) and (2.20). The impedance Z_o is given by

$$Z_o = \left(\frac{30\pi}{\sqrt{\varepsilon_r}}\right) \frac{(1 - \frac{t}{b})}{(\frac{w_{eff}}{b} + \frac{C_f}{\pi})} \tag{2.19}$$

where C_f is the fringing capacitance per unit length between the centre-strip and the adjacent ground plane.

C_f is given by

$$C_f = 2\ln\left(\frac{1}{1 - \frac{t}{b}} + 1\right) - \frac{t}{b}\ln\left\{\frac{1}{\left(1 - \frac{t}{b}\right)^2} - 1\right\} \tag{2.20}$$

By substituting t = 1.2 mm and b = 20 mm into (2.20) a value of $C_f = 1.57$ F is obtained. Using these values together with $Z_0 = 50\ \Omega$ and $\varepsilon_r = 1$ in (2.19) gives 25 mm as the effective width of the centre-strip. The centre-conductor is tapered at 20 degrees for impedance matching at the connector plane. The unique feature of this fixture is that its centre-conductor is not continuous and the fixture can be split into two. The schematic of the fixture in exploded form is shown in Figure 2.11

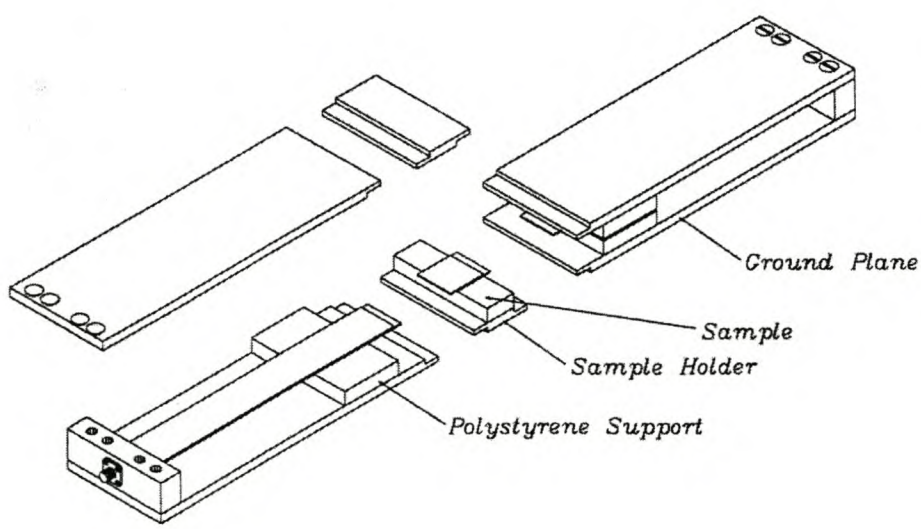

Figure 2.11 Components of the Stripline Fixture

2.5.2 Calibration of the Stripline Fixture

There are no precise calibration standards for the continuous centre conductor stripline fixtures reported in the literature [27][28][33].The algorithm which is normally used to calculate the complex permittivity and permeability using the measured S-parameters is the Nicolson-Ross-Weir (NRW) algorithm [28][34]. The algorithm requires that the fixture be calibrated at the front and back planes of the sample [28]. In the fixtures reported, such planes are inaccessible and, therefore, the calibration procedures mainly involve the use of either offset shorts or a single short in conjunction with sliding loads [33]. The S-parameters of the sample are then obtained from the measured parameters using a de-embedding procedure. Various de-embedding procedures in both the time and frequency domains have been proposed [4][5][15][28].

In this design the front and the back planes of the sample are accessible. The fixture is calibrated using the "Thru-Reflect-Line" (TRL) previously known as the"Thru-Short-Delay"(TSD) technique. The theoretical basis of the TRL calibration technique has been formulated in detail by [33] and the practical implementation is described by [30]and [32].

Conductive tape is used to align the calibration lines, including the Thru, during calibration and the sample holder during measurements. By using the conductive tape, the continuity and alignment of the continuous centre- strip variants is obtained in addition to the accessibility of the calibration planes.

A description of the calibration standards follows:

- reflect: the centre-strip of each half fixture is sandwiched between two aluminium blocks which short it to the ground planes.
- zero-length thru: the two halves of the fixture are connected together.
- line: a line together with grounding bars is placed between the two halves of the fixture. The width, thickness and material of the line standard is the same as that of the centre-strip. The length of the standard was chosen so that it fulfills the criteria set in the HP product note 8510-8 [35] on TRL calibration. The criteria requires that the insertion phase difference between the thru and the line be between (20° and 160^0) $\pm$ ($n\times180^\circ$), where n is an integer. An insertion phase difference outside these limits leads to a significant measurement uncertainty.

The beauty of TRL calibration emanates from the use of transmission lines as standards. The advantages of line standards stated in [35] are:

- they are easily realised in many non-coaxial media.
- their impedance can be determined accurately from physical dimensions and material properties.
- their operational behaviour is well understood.

The options which are available in the HP8510B implementation of the TRL calibration include [35]:

- using either zero-length or non-zero length thrus.
- using an unknown reflective termination such as an open, short and offset short.
- using multiple lines to cover a frequency band in which the stop frequency is eight times the start frequency.
- setting the reference plane relative to the thru or reflect.
- combining TRL calibration with open-short-load calibration for lower frequencies where line standards are too long to be practical.

2.5.2.1 Evaluation of the Calibration Technique

The quality of the calibration of the fixture was tested by measuring the post-calibration return loss, insertion loss and phase of the Thru. Representative post-calibration curves obtained after reconnecting the Thru on three separate measurement sessions are shown in Figure 2.12.

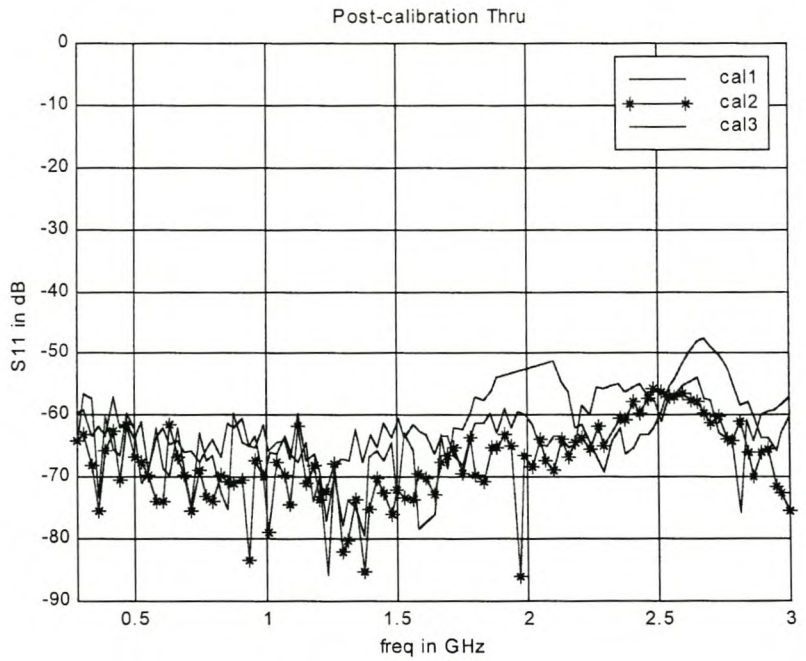

Figure 2.12(a) Post-calibration Thru: S_{11} in dB

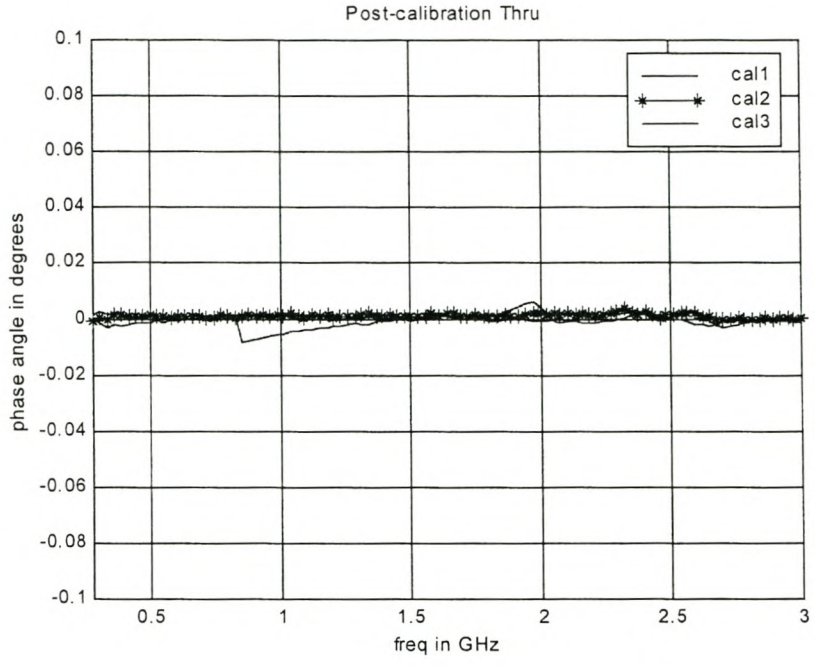

Figure 2.12(b) Post-calibration Thru: S_{21} phase in degrees

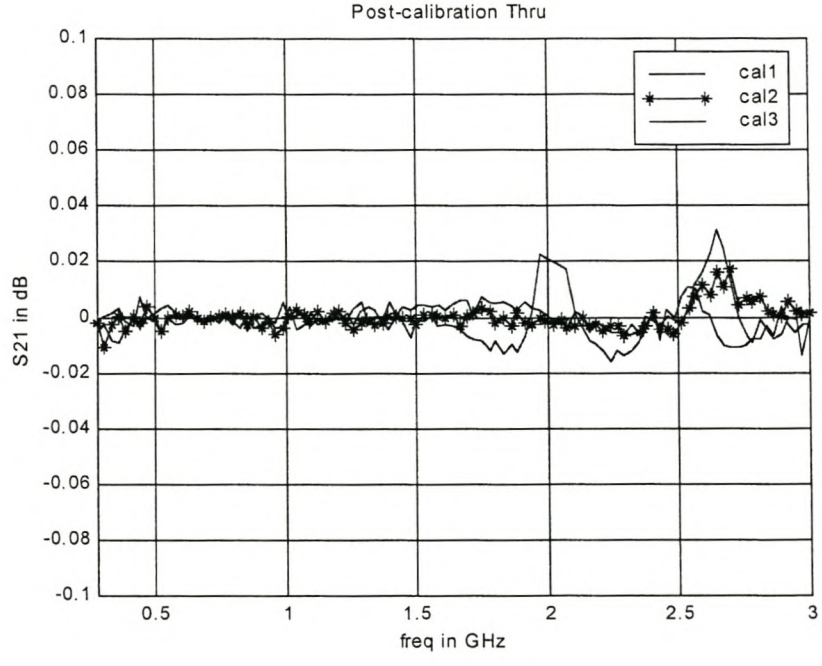

Figure 2.12(c) Post-calibration Thru: S_{21} in dB

From Figure 2.12, it can be seen that the insertion loss is less than -50 dB throughout the measurement band. This indicates a good match and it compares well with values quoted in the literature for well designed continuous centre-conductor stripline fixtures [15][28]. Even on a zoomed in scale, the post-calibration insertion phase and loss for the thru is zero across the measurement frequency band. This shows that the relative phase shift between the input and the output signals has been calibrated out properly. Removal of discontinuities of measurement system through calibration is evident in Figure 2.12(c). The mostly lower than -50 dB post-calibration return loss is better than that obtained for the matched load of the probe. This suggests that the stripline fixture is best suited for measuring the loss factor of low loss materials.

The fixture was calibrated on several separate occasions and the calibration curves differed by less than one percent.

2.5.3 Verification Measurements for the Split-Centre-Conductor Stripline Fixture

To test the system, the permittivities of PTFE and perspex samples were measured. Two blocks of each material were machined to a length of 70 mm, width of 30 mm and height of 10 mm. Each material sample was then placed in a sample holder with the length transverse to the centre strip. The loaded fixture was then connected to the ANA and measurements were taken.

The measured S-parameters were stored for further processing. The parameters were then used to calculate the complex permittivity of the samples using a MATLAB implementation of the modified Boughriet's [36] version of the NRW algorithm. The modification is discussed below.

2.5.3.1 Boughriet's Formulation and its Adaptation for Processing Stripline Fixture Data

Boughriet et al. [36] formulated the NRW algorithm for Transmission / Reflection (TR) measurements as follows:

$$K = \frac{S_{11}^2 - S_{21}^2 + 1}{2S_{11}} \tag{2.21}$$

$$\Gamma = K \pm \sqrt{K^2 - 1} \tag{2.22}$$

$$T = \frac{S_{11} + S_{21} - \Gamma}{1 - (S_{11} + S_{21})\Gamma} \tag{2.23}$$

$$\frac{1}{\Lambda^2} = \left[\frac{j}{2\pi d}\ln(T)\right]^2 \tag{2.24}$$

where d is the length of sample
Γ is the reflection coefficient
T is the transmission coefficient.
Λ is defined by equation 2.24

Up to this point this is the standard NRW formulation. Boughriet et al. [36] then introduced the idea of effective complex permittivity ε^*_{eff} and μ^*_{eff} permeability defined as

$$\mu^*_{eff} = \frac{\lambda_{og}}{\Lambda}\left(\frac{1+\Gamma}{1-\Gamma}\right) \tag{2.25}$$

$$\varepsilon^*_{eff} = \frac{\lambda_{og}}{\Lambda}\left(\frac{1-\Gamma}{1+\Gamma}\right) \tag{2.26}$$

where λ_{og} is the wavelength in the empty fixture.

They then calculated the complex permittivity ε^* and permeability μ^* using the following expressions

$$\mu^* = \mu^*_{eff} \tag{2.27}$$

$$\varepsilon^* = \left(1 - \frac{\lambda_0^2}{\lambda_c^2}\right)\varepsilon^*_{eff} + \frac{\lambda_o^2}{\lambda_c^2 \mu^*_{eff}} \tag{2.28}$$

where λ_o is the wavelength in free space
λ_c is the cutoff wavelength of the fixture

Equation (2.24) has a phase ambiguity which has been discussed by Weir [5]. The ambiguity can be corrected for, by adding a $2\pi nj$ term [34]. Various methods for determining n, reported as an integer, have been proposed. Weir [5] proposed the calculation of two group delays, one from theoretical considerations and the other from practical measurements. The value of n is obtained when the difference between the two group delays is approximately zero. The problem with Weir's proposal is that the theoretical delay uses the permittivity and the permeability of the sample to be measured. He used the unknown to find the unknown. This does not solve the problem.

Smith [37, appendix B] proposed that the integer n can be determined by differentiating T with respect to the phase angle. Theron [38, pp 45] adopted a slightly different approach to Smith's and showed that

$$n \approx \frac{j}{2\pi}\left[\frac{\omega}{\mathrm{T}}\frac{\partial\omega}{\partial\mathrm{T}} - \ln(\mathrm{T})\right] \tag{2.29}$$

where

$$T = e^{-j\gamma_o d} \tag{2.30}$$

From equations (2.29) and (2.30), it is shown in Appendix 2D that

$$n = \frac{j}{2\pi}\left[\frac{\pi f d}{15} - \ln(T)\right] \tag{2.31}$$

A MATLAB routine of Boughriet's version of the NRW formulation with $\lambda_c = 0$ was then run. The $2\pi nj$ term was added to ln(T) at the point where the permittivity had an abrupt change. The abrupt change was taken to be indicative of the phase ambiguity and therefore need for correction. The MATLAB routine is given in Appendix 2D and the results of runs for teflon and perspex are shown in Figure 2.13. The results are discussed in section 2.7.

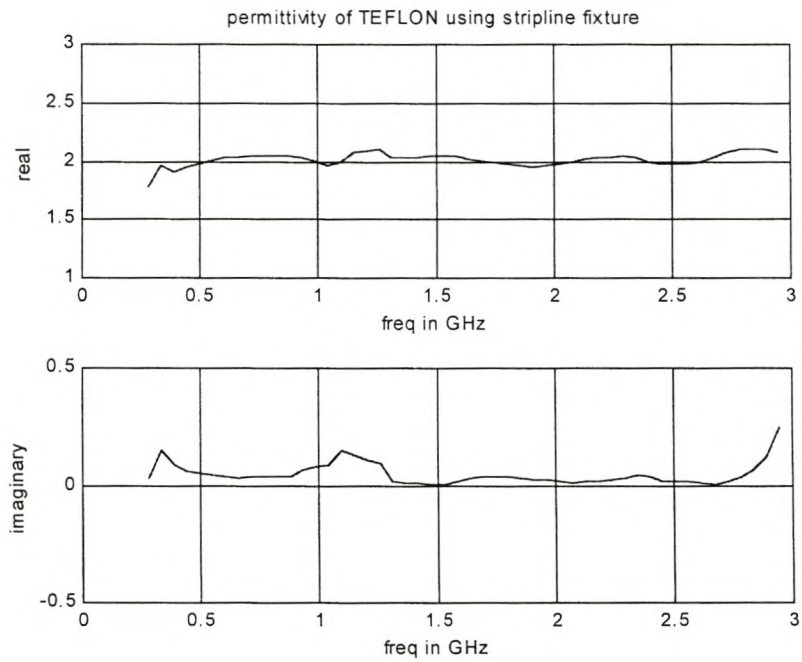

Figure 2.13(a) Pemittivity of teflon as measured by the new stripline fixture

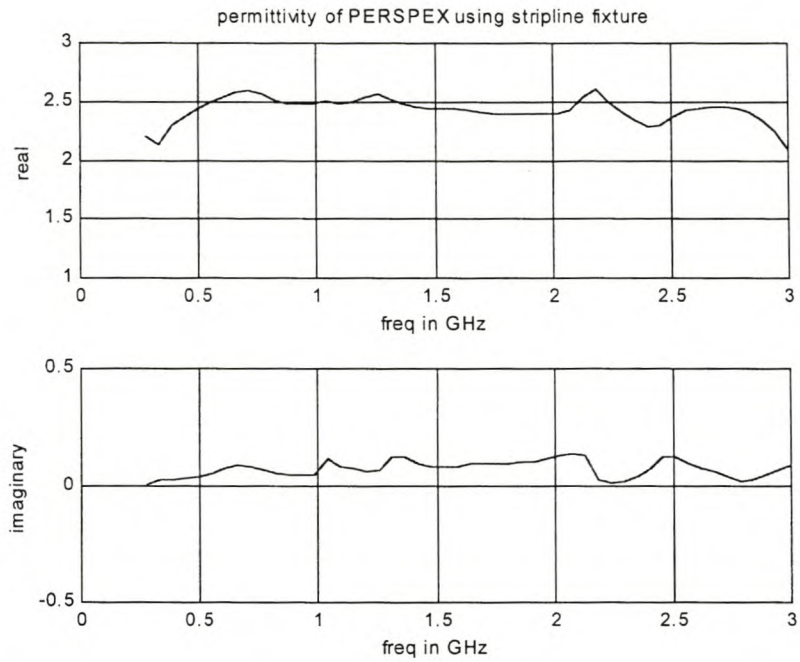

Figure 2.13(b) Permittivity of perspex as measured by the new stripline fixture

As with the Marconi jig and the coaxial probe, the average of the stripline measured values are compared with literature ones by way of Table 2.3. The average is taken in the range 0.5 to 2.5 GHz.

Table 2.3 Comparison of stripline measured (averaged in the range 0.5 to 2.5 GHz) and reported values [43]

Material	ε' (measured)	ε' (reference)	$\tan\delta$ (measured)	$\tan\delta$ (reference)
Teflon	2.0	2.1	0.0138	< 0.0002
Perspex	2.5	2.6	0.0320	0.0300

As anticipated from the post-calibration return loss, the loss factor (and, therefore, $\tan\delta$) is more accurately determined from the stripline measured data than from either the probe or the Marconi jig.

The plots have glitches which are more pronounced at the frequencies where phase ambiguity was corrected for. The other sources of glitches are:

- discontinuities of the stripline fixture especially the centre strip. The conductive tape does not provide the same continuity as the continuous strip.
- errors due to imperfect contact between sample and fixture
- experimental errors

To obtain further insight into the performance of the stripline fixture, it was necessary to carry out an uncertainty analysis. The analysis is shown in Appendix 2E and typical results are given in Figure 2.14.

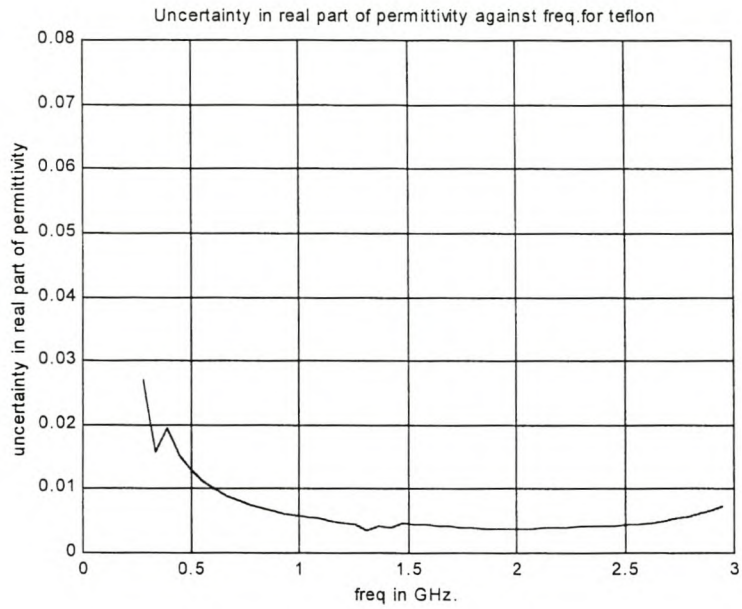

Figure 2.14 (a) Uncertainty in real part of permittivity of teflon as measured by stripline fixture

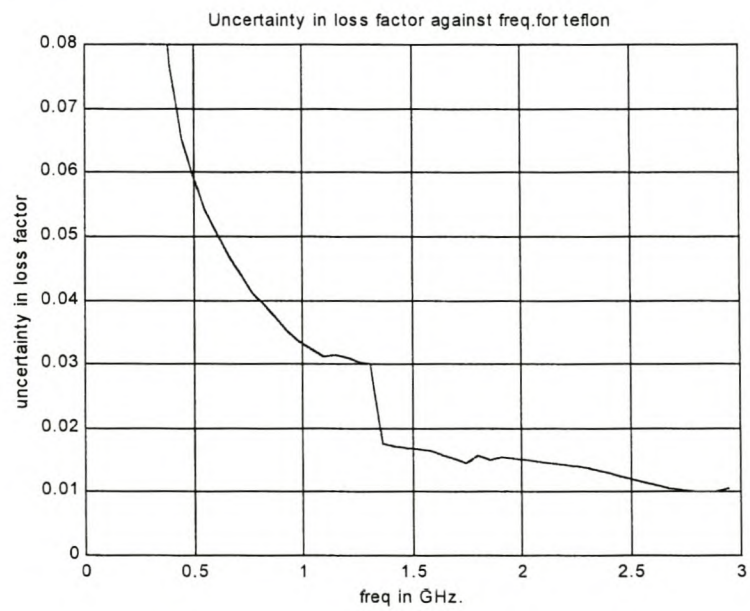

Figure 2.14(b) Uncertainty in the loss factor of teflon as measured by stripline fixture

Figure 2.14 shows a general decrease of uncertainty with frequency, a trend also observed by [46] in the uncertainty analysis of a transmission / reflection system. The large uncertainty at lower frequencies is attributed to the starting frequencies specified in the calibration kit of the ANA. The uncertainty in ε' is dominated by phase uncertainties and that in ε'' by the magnitude of the reflection coefficient. The uncertainty in ε'' is greater than that in ε'. This implies that ε' is measured more accurately than ε'' on a stripline fixture. When uncertainties are included (plus or minus), the difference between the Von Hippel[43] and the measured values is narrowed.

2.6 Waveguide Fixture

Transmission lines (coaxial and waveguide) are widely used to measure the dielectric properties of materials [5]. The technique is based on transmission or reflection measurements on an ANA. A waveguide system is employed in this investigation.

A number of measurements on two different waveguide fixtures were carried out before acceptable results were obtained. In the first set of measurements, a WR340 waveguide fixture was employed. The following calibration kit was used:

- offset shorts: 21.5 and 43.4 mm shorts.
- fixed load: waveguide section with an optimally shaped conductive foam.
- thru: waveguide sections are bolted together.

After a full-2-port TRL calibration (with isolation omitted), the S-parameters of teflon and perspex test samples were measured. Figure 2.15 illustrates the measurement setup.

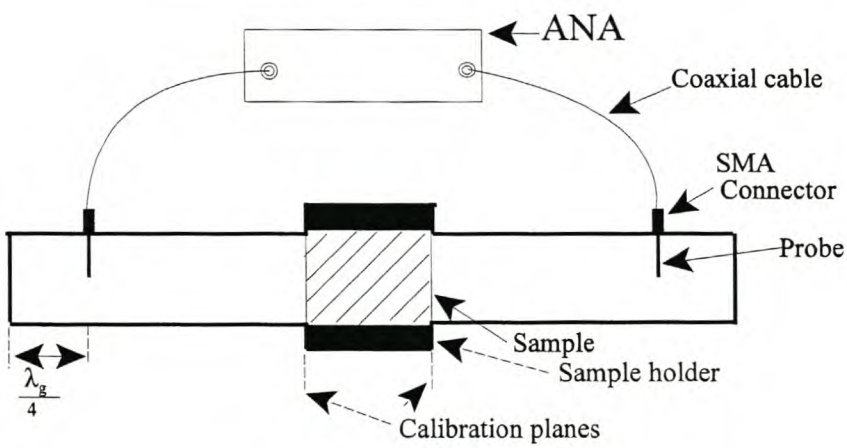

Figure 2.15 Setup for S-parameter measurement using a waveguide fixture

A MATLAB routine (Appendix 2F), implementing the NRW algorithm, was used to calculate the dielectric properties of teflon and perspex from the measured S-parameters. The values of ε' and ε'' obtained for each of the samples were consistently below those tabulated by Von Hippel [43].

The fixture was changed to one based on a WR284 waveguide but the results did not improve. A discussion session (Prof. H.C. Reader, M. Rimbi and W. J.Louw present) identified the load calibration standard as the possible 'weak standard'. An open-ended waveguide section of length 500 mm, with a tapered absorbing foam, was used as the sliding load.

Representative results obtained after using the sliding load in a full-2-port calibration which included isolation are shown in Figures 2.16 and 2.17.

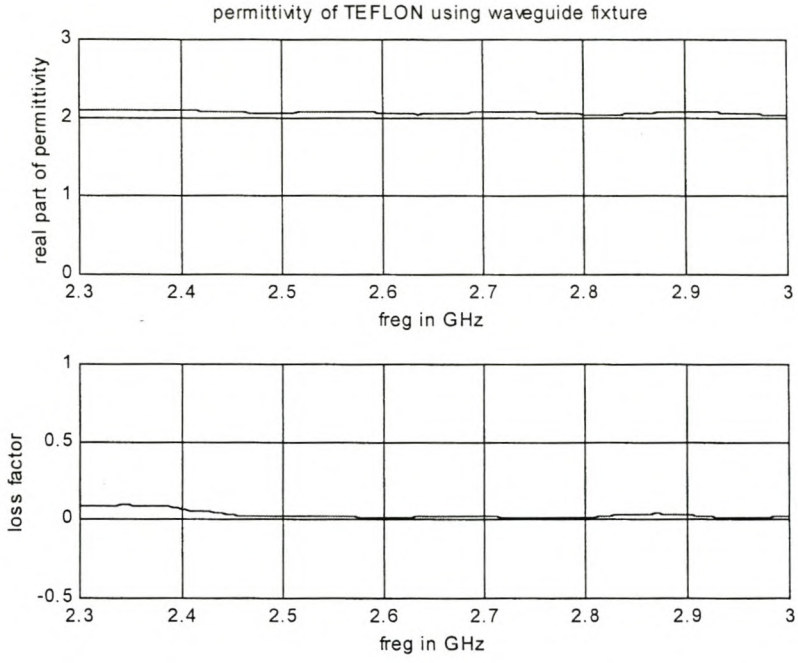

Figure 2.16 Permittivity of teflon as measured in a waveguide system

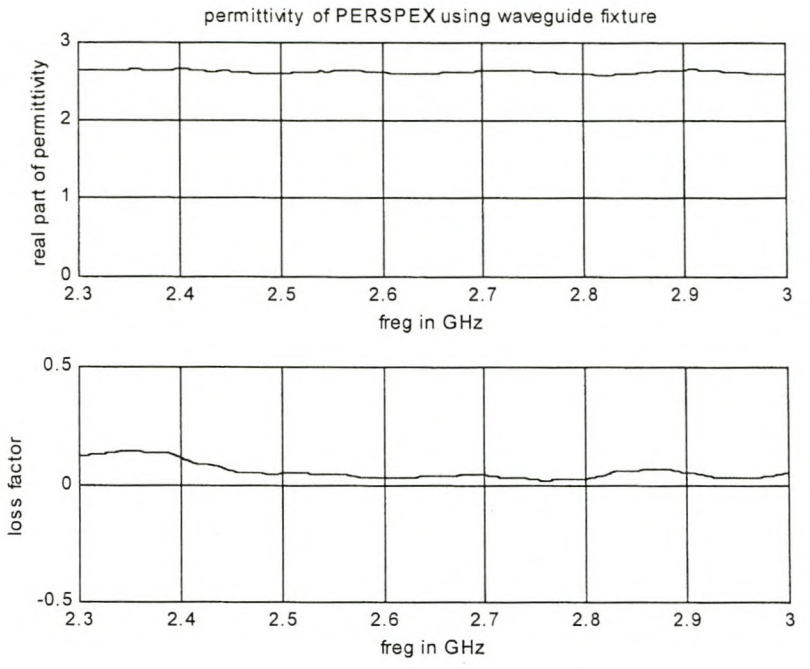

Figure 2.17 Permittivity of perspex as measured in a waveguide system

The waveguide measured values are compared with the literature values in Table 2.4

Table 2.4 Comparison of waveguide measured (averaged in the range 2.3 to 3 GHz) and reported values [43]

Material	ε′ (measured)	ε′ (reference)	tanδ (measured)	tanδ (reference)
Teflon	2.1	2.1	0.0198	< 0.0002
Perspex	2.6	2.6	0.0296	0.0300

These results are very pleasing. It shows that for a waveguide fixture:

- a sliding load is better than a fixed load standard.
- isolation must be implemented in the calibration procedure.

2.7 Discussion

The real part of permittivity for both teflon and perspex obtained using the ANA-based systems are of the same magnitude as the values quoted by Von Hippel [43]. However, the loss factors are not. This is because the S-parameters of low loss materials are dominated by tiny mismatches at the connections of various components of the measuring system. These small mismatches could not be calibrated out adequately by the impedance matching standards. For the capacitive plate, air gaps and fringing effects are the major limitations.

Loss factors less than 10^{-2} are best measured using cavity perturbation methods. Resonant cavities require very small samples and are narrowband. For the material of interest in this study, wood, an inhomogeneous anisotropic material, one would need to measure a very large number of small samples in order to come up with a value which is representative of the bulk. Perturbation methods were considered unsuitable for wood studies.

It should also be noted that the frequency range of the capacitive plate is not the same as that of the other systems. The frequency range of the capacitive plate is limited by the resonating circuit and accessories. The lower frequencies of the probe and stripline fixtures are limited by the calibration standards. The combination of the capacitive plate and the ANA based systems provides a useful way of obtaining wide band permittivity measurements. The Marconi and the ANA based systems compliment each other as can be seen for the teflon sample in Figure 2.18.

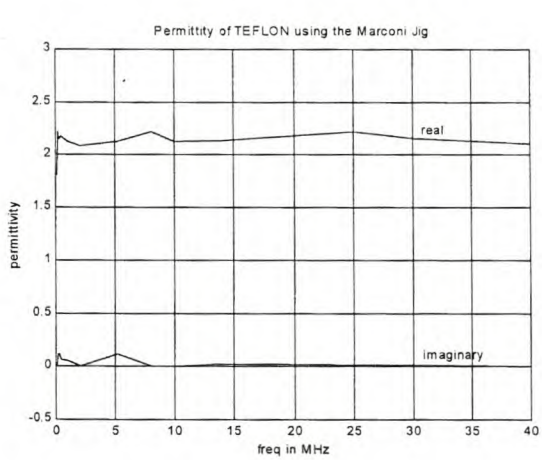

(a) Teflon as measured by Marconi jig

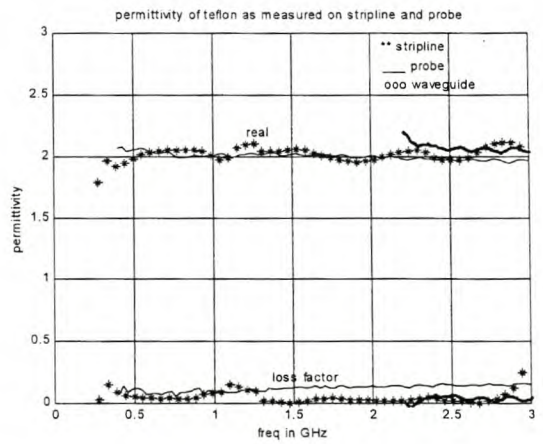

(b) Teflon as measured by probe (_____) stripline (***) and waveguide(ooo)

Figure 2.18 Relationship between Marconi and ANA based systems

Use of the open-ended probe produces reflected data. The reflections occur within a small area and depth of the MUT. Thus, the probe gives specific spot data if this is so required. For results obtained in this manner to be representative, the MUT must be isotropic and homogeneous.

For anisotropic materials such as wood, transmission measurements are more appropriate than reflection. The Marconi test jig, the waveguide system and the stripline fixture are transmission measuring systems. However, the Marconi jig is bandwidth limited and is slow (measurements are done at one frequency at a time). The preparation of waveguide samples which takes into consideration the anisotropy of wood was constrained by the size of available wood and machining resources. This leaves the stripline fixtures as the most suitable choice for measuring the dielectric properties of wood. The measurements are given in Chapter 5.

From the fixtures used, the real part can be determined accurately but not the imaginary part. Theoretically, the imaginary part can be determined from the real part using the Kramers-Kronig relationship. Practical attempts at using the full Kramers-Kroning relationship have so far been unsuccessful for reasons given in [87].

2.8 Conclusion

Four fixtures have been tested against each other by using them to measure the permittivities of teflon and perspex. The obtained permittivities have been compared with those quoted by Von Hippel [43]. The results indicate that electric dielectric properties are not easy to measure because the values obtained depend on the measurement method among other factors.

Algorithms for extracting dielectric properties from measured data have been developed from existing ones. For application to the stripline fixture, the algorithm presented by Boughriet et al. needed substantial modification.

It has been shown that in waveguide calibration, a sliding load performs better than a fixed load standard. Excellent results are obtained when isolation is included in the calibration.

A panel mount SMA female connector has been modified into a coaxial probe for the first time. A new calibration kit for a coaxial probe has been designed, built and tested. Through a collaboration with a researcher at NIST, the capacitive coefficients of the open standard were accurately determined.

A novel split-stripline fixture with easily accessible calibration planes for repeatable TRL calibration was designed, built and tested. The stripline lends itself to easy sample insertion. The data acquired using this stripline fixture does not need de-embedding. A differential uncertainty analysis was done on the measurement errors of the stripline. The uncertainty was found to be frequency dependent. The fixture is used to measure the dielectric properties of wood in Chapter 5.

Chapter 3

DESIGN OF THE SLOTTED WAVEGUIDE FEED FOR A MICROWAVE APPLICATOR

3.1 Introduction

The electromagnetic field in the vicinity of a source (such as a magnetron) is characteristically non-uniform. When drying wood, a high degree of heating uniformity is required. To achieve heating uniformity using a microwave system, the applicator must present a uniform electromagnetic field to the load. This challenge can be addressed partially by using a multimode applicator with an appropriate feeder and microwave source. The choice of the feed and the microwave generator depends on whether the workload processing is batch or continuous [39].

For high power generators, slotted waveguides and horn feeds can be used in either processing mode to achieve high uniformity. The horn feed tends to be larger and incompatible with equipment layout. The slotted waveguide is, therefore, used more often. This chapter describes the analytical and computer aided design (CAD) of a slotted waveguide feed for a microwave applicator.

The design is validated experimentally using a purpose-built WR340 aluminium waveguide structure with six adjustable slots, to be referred to as the dummy. A real aluminium waveguide with a removable slotted plate is then designed, constructed and characterized. Its radiation properties are compared with those of the dummy and with simulations.

3.2 Analytical Design of a Slotted Waveguide Feeder for a Microwave Applicator

The theory of slots in rectangular waveguides is well developed. Among the most referenced contributions are the works of Elliott [49-52]. Elliott derived, at length, equations and proposed procedures for designing slot arrays in rectangular waveguides with and without mutual coupling. The use of the formulas is widely discussed but rarely used in a complete design example. Those who have attempted to apply the formulas have often resorted to the Stegen design graphs at some point in their procedure [49-52]. The tendency is to scale the results of the RG52/U waveguide, the slot dimensions and the 9.375 GHz frequency used by Stegen.

The formulas given by Elliott [49-52], Collin [53], Milligan [54] and Balanis [55] are combined here to produce a systematic method for designing a slotted waveguide feed for a microwave applicator.

3.2.1 Induced Currents in the Walls of a Waveguide and Location of Broadside slots

When an electromagnetic wave propagates in a rectangular waveguide, currents are induced in the inner walls of the guide. The surface density of the induced currents depends on the side of the guide. For the broad wall under consideration the density is [53 pp265]

$$J_s = \left[-j\frac{EY}{ka}\cos\left(\frac{\pi x}{a}\right)\mathbf{x} - \frac{EY\beta}{k}\sin\left(\frac{\pi x}{a}\right)\mathbf{z}\right] e^{-j\beta z} \tag{3.1}$$

where

J_s is the surface current density
E is the maximum electric field
Y is the maximum admittance of the propagating mode
x is the unit vector in the x-direction
z is the unit vector in the z-direction

For the slots to radiate, they must be located at points where they shunt the surface currents. Figure 3.1 depicts the surface current distribution and locations of broadside slots for a TE_{10} mode.

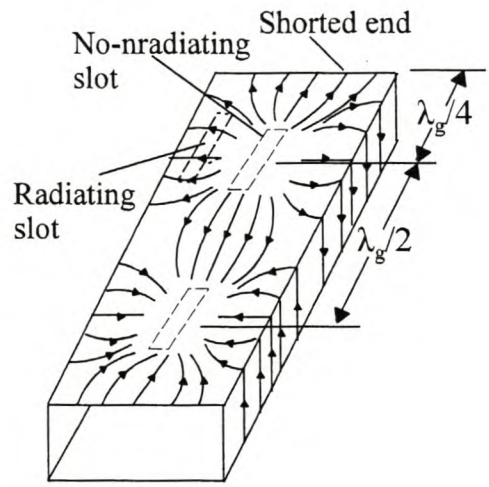

Figure 3.1 Current distribution and location of broadside slots (after [68])

It should be noted in Figure 3.1 that the centre of the first slot is a quarter waveguide wavelength from the shorted end. This is done in order to radiate the first maximum of the resultant standing wave.

3.2.2 Design Without Mutual Coupling

This design has been described by many authors including [49-53]. A brief description of the procedure as implemented in this study follows.

The design is initiated by choosing the number of slots n and the relative excitation level of each slot, a_n. The excitation can be uniform or non-uniform. Maximum power is radiated by the slot array when

$$K\sum_{n=1}^{N} a_n^2 = 1 \tag{3.2}$$

where K is a constant. After computing K using equation (3.2), the normalized nth slot equivalent circuit conductance g_n, shown in figure 3.2, is calculated using

$$g_n = Ka_n^2 \tag{3.3}$$

The average radiated power is proportional to g_n.

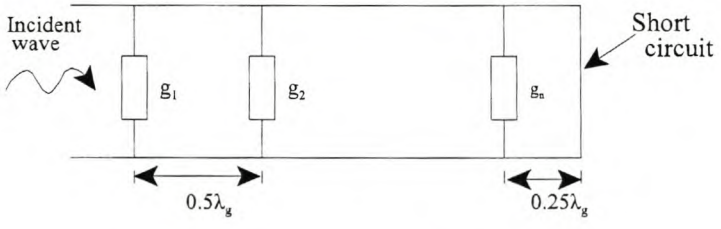

Figure 3.2 Equivalent circuit for slots on the broadside of a waveguide (after [53])

A rectangular waveguide of dimensions a and b is then chosen. The propagation wavelength in the guide, λ_g, of a specified mode, for example TE_{10}, is calculated from

$$\frac{1}{\lambda_g^2} = \frac{1}{\lambda^2} - \left(\frac{m}{2a}\right)^2 - \left(\frac{n}{2b}\right)^2 \tag{3.4}$$

where

λ is the free space wavelength
m and n are integers

The values of g_n obtained from equation (3.3) are then used to calculate the offsets x_n of the slots from the centre-line of the waveguide using the Stephenson expression for the TE_{10} mode [53 pp 266] expressed conveniently as

$$x_n = \frac{a}{\pi}\sin^{-1}\left[\sqrt{\frac{g_n \lambda b}{2.09\lambda_g a\cos^2\left(\frac{\pi\lambda}{2\lambda_g}\right)}}\right] \tag{3.5}$$

The length l_n of a rectangular rounded slot of width w and negligible thickness is determined from an empirical relationship given by Cohn [56] as

$$l_n = \frac{\lambda}{2}\sqrt{1+\left(\frac{2aw}{b\lambda_g}\right)^2} \tag{3.6}$$

In equation (3.6), a choice between length and width must be made. A length of $\lambda/2$ is usually used. The width is then chosen such that

$$2\log\left(\frac{length\,of\,slot}{width\,of\,slot}\right) >> 1 \text{ . [57]}$$

In most cases, the width is made equal to 0.1 of the length. The above condition not-withstanding, the actual width of the slot is dictated by available machining resources.

Equations (3.2) to (3.6) were used in the design of a slotted waveguide feed to the following specifications:

- frequency of operation equal to 2.45GHz
- waveguide dimensions of a = 86.36 mm and b = 43.19 mm
- propagating mode TE_{10}
- six slots
- uniform excitation of slots

The computations produced offsets x_n of 11.5 mm and lengths l_n of 61.8 mm.
A slot width of 6 mm was used.

This design does not include mutual coupling. Mutual coupling is considered in Section 2.4. A comparison of the two design approaches is also given in that section.

3.2.3 Design which Includes Mutual Coupling

The design without mutual coupling determines the lengths and offsets of isolated slots. In an array, the performance of each slot is influenced by the presence of its neighbours. It is, therefore, necessary to investigate the effect of mutual coupling between the slots. This is done by optimizing the lengths and offsets using a procedure which will now be described.

Elliot [49] showed that the normalised active admittance of a longitudinal shunt slot is given by

$$\frac{Y_n^A}{G_o} = \frac{1}{Z_n^A/73}\left[\frac{4(a/b)}{0.61\pi(\beta/k)}\left\{\cos(\beta l_n)-\cos(kl_n)\right\}^2\sin^2\left(\frac{\pi x_n}{a}\right)\right] \tag{3.7}$$

where

Z_n^A is the active impedance of the nth complimentary cylindrical dipole defined by

$$Z_n^A = Z_n + Z_n^L + \sum_{m=1}^{N} \frac{I_m}{I_n} Z_{mn} \tag{3.8a}$$

or

$$Z_n^A = Z_n + Z_n^L + \sum_{m=1}^{N} \frac{V_m^s}{V_n^s} Z_{mn} \tag{3.8b}$$

where

Z_n is the self-impedance of a cylindrical wire dipole

Z_n^L is the impedance of the load placed in series with the slot. For a perfect match, this normalised impedance is taken to be equal to one.

Z_{mn} is the mutual impedance between dipoles

V_m^s is the voltage of the mth slot to be designed

V_n^s is the voltage of the nth slot to be designed

In a uniform radiation design being reported, the voltages and the lengths of the coupling devices are equal, therefore

$$Z_n^A = Z_n + Z_n^L + \sum_{m=1}^{N} Z_{mn} \tag{3.9}$$

To find the mutual coupling at dipole n, n is kept constant and m is varied from 1 to $(n+1)$. The situation where m is equal to n is not permissible because it gives self-impedance.

The self impedance of a wire dipole is given by [51 pp 301]

$$Z_n = \frac{j60}{\sin^2(kl)}\left[4\cos^2(kl)S(kl) - \cos(2kl)S(2kl) - \sin(2kl)\{2C(kl) - C(2kl)\}\right] \tag{3.10}$$

where

$$C(ky) = \ln(2y/\Omega) - 0.5C_{in}(2ky) - 0.5jS_i(2ky)$$

$$S(ky) = 0.5S_i(2ky) - 0.5C_{in}(2ky) - k\Omega$$

in which

$$C_{in}(x) = \int_0^x \frac{1-\cos(u)}{u}\,du$$

$$= -\sum_{n=0}^{\infty} \frac{(-x^2)^n}{2n(2n)!}$$

$$S_i(x) = \int_0^x \frac{\sin(t)}{t} dt$$

$$= \sum_{n=0}^{\infty} \frac{(-1)^n x^{(2n+1)}}{(2n+1)(2n+1)!}$$

$$C_i(x) = -\int_x^{\infty} \frac{\cos(t)}{t} dt$$

$$= \xi + \ln x - C_{in}(x)$$

$$= \xi + \ln x + \int_0^x \left[\frac{\cos(t)-1}{t}\right] dt$$

$$= \xi + \ln x + \sum_{n=1}^{\infty} \frac{(-1)^n x^{2n}}{(2n+1)(2n+1)!}$$

where ξ is Euler's constant.

The cross-sectional area of the complementary cylindrical dipole Ω, is related to the width w and the thickness t of a strip removed when making the slot by [56]

$$\Omega = 0.25(w+t) \tag{3.11}$$

It is assumed that the length and width of the strip dipole are equal to those of the slot.

Expressions for the mutual impedance between slender dipoles are derived in several books on "Antenna Theory and Design" such as [51][55] and are given in various alternate forms. The mutual impedance at antenna m due to current flowing in antenna n is denoted by Z_{mn}. Z_{nm} is defined similarly. Reciprocity theorem holds, so Z_{mn} is equal to Z_{nm}. The mutual impedance, Z_{nm}, referred to the current at the input terminals for two wire parallel dipoles is given by [55 pp 229][51 pp 332] as:

$$Z_{nm} = jQ\int_{-l_n}^{l_n} \left[\frac{e^{-jkR_1}}{R_1} + \frac{e^{-jkR_2}}{R_2} - 2\cos(kl_m)\frac{e^{-jkr}}{r}\right] \sin(kl_n - |z|)dz \tag{3.12}$$

where

R_1 is the distance travelled by the wavefront of the wave emanating from the top end of dipole m to the point of observation on dipole n

R_2 is the distance travelled by the wavefront of the wave originating from the bottom end of dipole m to the point of observation of dipole n

r is the distance travelled by the wavefront from the centre of dipole m to the point of observation on dipole m

k is the propagation constant

l_m is half the length of dipole m
l_n is half the length of dipole n
z is the distance of the observation point from the reference level, usually the centre of the dipole

$$Q = \frac{30}{\sin(kl_m)\sin(kl_n)}$$

The path lengths are shown in Figure 3.3.

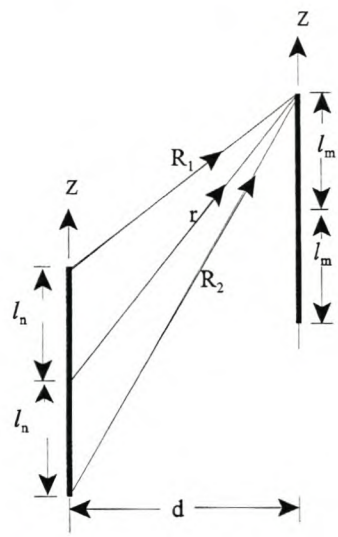

Figure 3.3 Path lengths between sources and observation point on two parallel wire dipoles

Casting the numerators of the Green functions into trigonometric form and writing the real and imaginary parts of Z_{nm}, yields

$$R_{nm} = Q\int_{-l_n}^{l_n}\left[\frac{\sin(kR_1)}{R_1} + \frac{\sin(kR_2)}{R_2} - 2\cos(kl_m)\frac{\sin(kr)}{r}\right]\sin\{k(l_n - |z|)\}dz \qquad (3.13)$$

$$X_{nm} = Q\int_{-l_n}^{l_n}\left[\frac{\cos(kR_1)}{R_1} + \frac{\cos(kR_2)}{R_2} - 2\cos(kl_m)\frac{\cos(kr)}{r}\right]\sin\{k(l_n - |z|)\}dz \qquad (3.14)$$

The mutual coupling resistance and reactance can be evaluated directly using a symbolic computational utility such as MATHEMATICA. In the absence of such a package, the integrals can be written in a simpler form, the derivation of which is shown by [58 pp 537-540]. Simplified form expressions for the side-by-side, collinear and parallel in echelon configurations are given by [55 pp 299-300]. To use the simplified equations, tabulated values of sine and cosine integrals

should be consulted. In this study, look-up tables were created as MATLAB functions, Appendix 3.A.

3.2.3.1 Evaluation of R_{nm} and X_{nm}

A key step in the evaluation of R_{nm} and X_{nm} is the determination of the path lengths of the waves. The path lengths depend on the dipole configuration. For two dipoles in parallel echelon, the lengths from the wavelet sources on dipole one to the observation point on dipole two are as shown in Figure 3.4*a*.

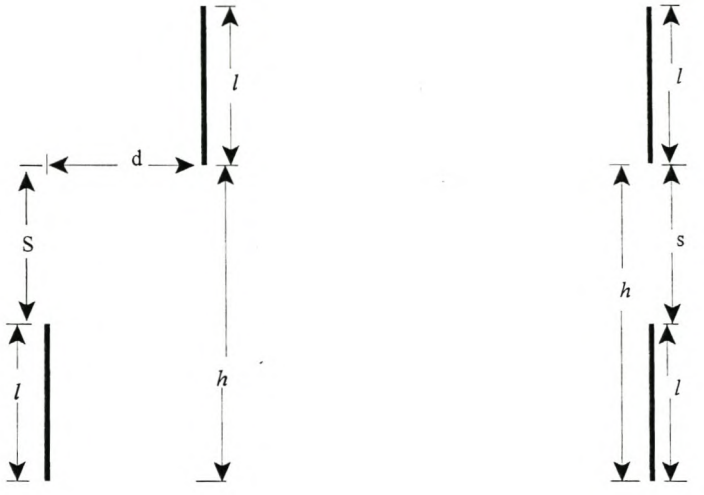

(a) parallel echelon (b) Collinear

Figure 3.4 Configuration of dipoles

From Figure 3.4*a* the electrical path lengths, w_n, can be defined in terms of geometry and wave number, k:

$$w_0 = k(l + s) \tag{3.15a}$$

$$w_1 = k\left[\sqrt{d^2 + (l + s)^2}\right] \tag{3.15b}$$

$$w_2 = k\left[\sqrt{d^2 + (l + s)^2}\right] \tag{3.15c}$$

$$w_3 = k\left[\sqrt{d^2 + s^2}\right] \tag{3.15d}$$

$$w_4 = k\left[\sqrt{d^2 + s^2}\right] \tag{3.15e}$$

$$w_5 = k\left[\sqrt{d^2 + (2l + s)^2}\right] \tag{3.15f}$$

$$w_6 = k\left[\sqrt{d^2 + (2l+s)^2}\right] \tag{3.15g}$$

The path lengths can be substituted into the parallel echelon equations given by [55 pp 300] as:

$$R_{nm} = -15Q\cos(w_0)[-2C_i(w_1) - 2C_i(w_2) + C_i(w_3) + C_i(w_4) + C_i(w_5) + C_i(w_6)]$$
$$+ 15Q\sin(w_0)[2S_i(w_1) - 2S_i(w_2) - S_i(w_3) + S_i(w_4) - S_i(w_5) + S_i(w_6)] \tag{3.16}$$

$$X_{nm} = -15Q\cos(w_0)[2S_i(w_1) + 2S_i(w_2) - S_i(w_3) - S_i(w_4) - S_i(w_5) - S_i(w_6)]$$
$$+ 15Q\sin(w_0)[2C_i(w_1) - 2C_i(w_2) - C_i(w_3) + C_i(w_4) - C_i(w_5) + C_i(w_6)] \tag{3.17}$$

The mutual resistance and reactance obtained from equations (3.16) and (3.17) are used to calculate the mutual impedance using

$$Z_{nm} = R_{nm} + jX_{nm}$$

A similar approach can be followed to calculate the mutual impedances due to other parallel echelon configured dipoles.

For the collinear configuration, figure 3.4*b,* the relevant electrical path lengths are:

$$v_0 = k(l+h) \tag{3.18a}$$

$$v_1 = k(2l+h) \tag{3.18b}$$

$$v_2 = kd \tag{3.18c}$$

The electrical path lengths are entered into the collinear equations given by [55 pp 300] as

$$R_{nm} = -15Q\cos(v_0)[-2C_i(2v_o) + C_i(v_1) + C_i(v_2) - \ln(v_3)]$$
$$+ 15Q\sin(v_0)[2S_i(2v_0) - S_i(v_2) - S_i(v_1)] \tag{3.19}$$

$$X_{nm} = -15Q\cos(v_0)[2S_i(2v_0) - S_i(v_2) - S_i(v_1)]$$
$$+ 15Q\sin(v_0)[2C_i(2v_o) - C_i(v_1) - C_i(v_2) - \ln(v_3)] \tag{3.20}$$

The mutual resistance and reactance are added to give the mutual impedance of the collinear dipoles. The mutual impedances of the collinear and parallel in echelon array elements are added to give Z_{mn}. The slotted waveguide feed contains both collinear and parallel in echelon coupling elements. The path lengths are found by applying Pythagoras theorem.

3.2.3.2 Evaluation of Slot Lengths and Offsets with Mutual Coupling

The length of the slot when mutual coupling is taken into account is obtained by invoking Babinet-Booker principle. The principle gives the relationship between the impedance of the slot , Z_{slot} , and that of the complimentary dipole, Z_{dipole} , as [54 pp 71]

$$Z_{slot} Z_{dipole} = \frac{\eta^2}{4} \tag{3.21}$$

where η is the impedance of free space

For the problem at hand, the impedances in equation (3.21) are mutual impedances. It follows that the normalised input impedance of the slotted waveguide array with mutual coupling, g_m , is given by

$$g_m = \frac{1}{Z_{slot}} \tag{3.22}$$

Milligan [54 pp 69] gives the relationship between the radiation and input conductance of a slot as

$$G_i = \frac{G_r}{\sin^2\left(\frac{kL}{2}\right)} \tag{3.23}$$

where G_r is the radiation conductance of a slot
G_i is the input conductance of a slot

Normalising the input conductance by the radiation conductance gives an alternative expression for g_m as

$$g_m = \frac{1}{\sin^2\left(\frac{kL_m}{2}\right)} \tag{3.24}$$

where L_m is the length of the slot.

Thus

$$L_m = \frac{2\sin^{-1}\left(\frac{1}{\sqrt{g_m}}\right)}{k} \tag{3.25}$$

The slotted waveguide feed design procedure with mutual coupling, implemented as a MATLAB routine, Appendix 3.B is summarised by the flow diagram below.

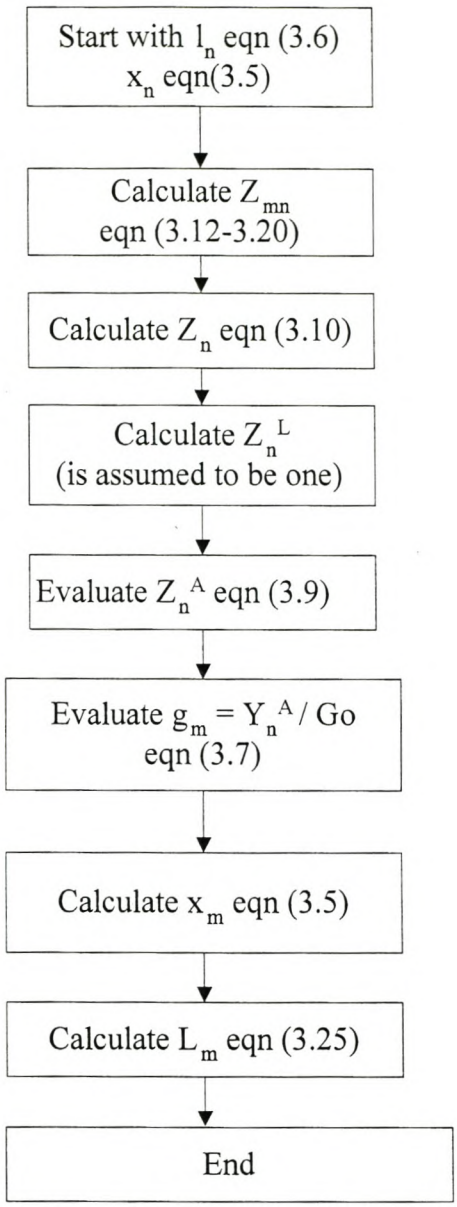

Figure 3.5 Flow chart for slot design which includes mutual coupling

3.2.4 Results, Discussion and Conclusion

The mutual coupling design given in section 3.2.3 was applied to a four-slotted waveguide example given by Elliott [51 pp 412-414]. The example has relative excitation levels of 1:2:2:1. The design without mutual coupling was also carried out using the four-slotted waveguide example. The results are tabulated in Table 3.1

Table 3.1 Offsets and Lengths of Slots as Calculated by Elliott and the Author (inches are used as the unit of length)

	Elliott (without mutual coupling)	Author (without mutual coupling)	Elliott (with mutual coupling)	Author (with mutual coupling)
x_1	0.082	0.082	0.086	0.081
x_2	0.180	0.174	0.176	0.181
x_3	0.180	0.174	0.176	0.181
x_4	0.082	0.082	0.086	0.081
L_1	0.613	0.629	0.620	0.630
L_2	0.631	0.629	0.637	0.630
L_3	0.631	0.629	0.637	0.630
L_4	0.631	0.629	0.620	0.630

Table 3.1 shows the good agreement between Elliott's and the author's results for both design cases. It also shows that the differences in offsets and lengths obtained by the two methods are insignificant. The differences between the author's and Elliott's results can be attributed to:

- g_n values used are different. Values of 0.093 and 0.407 are used by Elliott and the author uses 0.1 and 0.4.
- Elliott used approximate formulae obtained from regression analysis of Stegen's data.
- rounding errors

This example shows that slots with the same excitation level have the same offsets. It also shows that the design can be accomplished adequately without considering mutual coupling. Because of the lengthy computations involved in the analytical design, a computer-aided design was investigated. It is covered in Section 3.3.

3.3 Computer-Aided Design (CAD)

To get insight into the magnitude and pattern of the radiation emitted by the slots and for comparison with offsets and lengths obtained in the analytical design, a design with a CAD package was undertaken. Packages implementing the Finite Difference Time Domain (FDTD) (first version) and the Finite Element Method (FEM) (seventh version) were investigated. The investigation compared simulated and experimental results. The correlation between FEM simulations and experiments were consistently better than those with FDTD, so FEM became the package of choice. FEM is among the most popular of a group of numerical techniques which have become indispensable tools in electromagnetic field analysis. Following [59] the position of FEM in the group is best indicated on a tree diagram shown in Figure 3.6

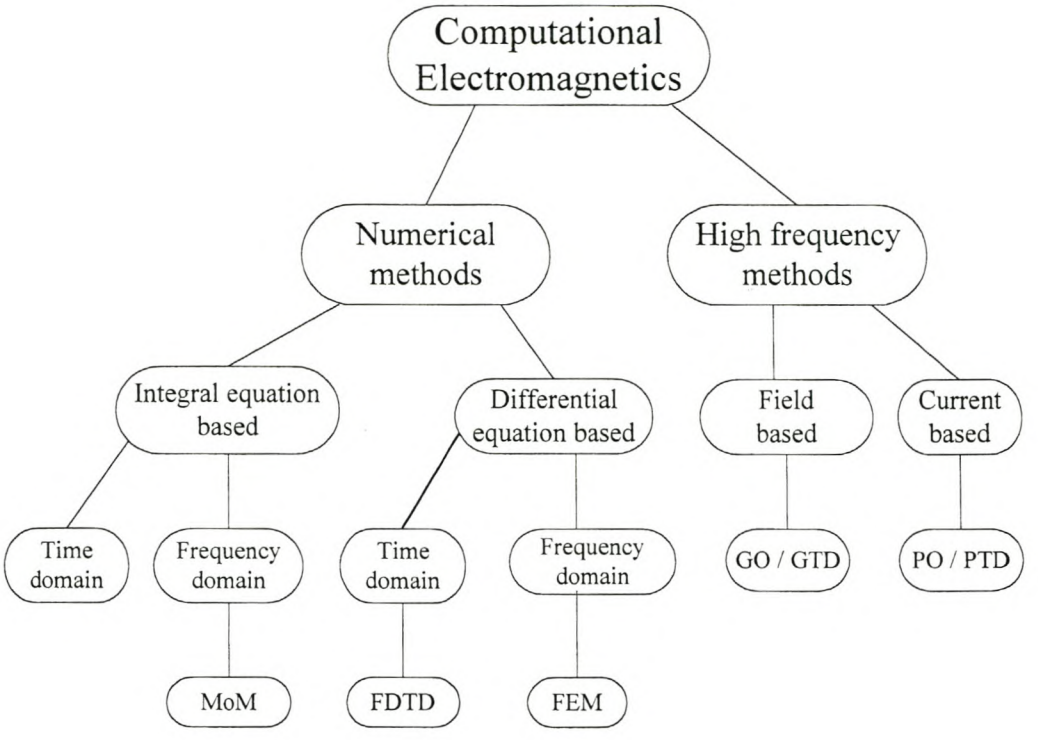

Figure 3.6 Computational techniques in electromagnetics

A brief review of FEM is given in Section 3.3.1.

3.3.1 Brief Overview of FEM

The Finite Element Method is normally applied to a volumetric problem domain, however, it has also been applied to one and two dimensional cases mostly for introductory purposes. The geometric domain is discretised into elementary geometries called finite elements. The elements can be regular or irregular. Geometries of the most commonly used elements are shown in Figure 3.7 [60 pp 408].

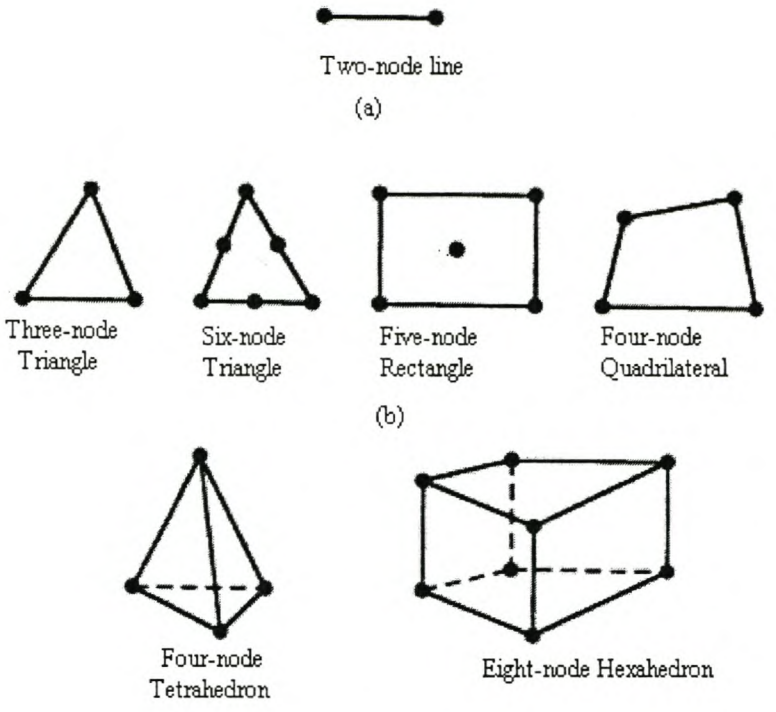

Figure 3.7 Most commonly used finite elements

A collection of elements is referred to as a mesh. The larger the mesh size (i.e the smaller the elements) the greater the accuracy and the longer the computational time. Thus a trade-off is usually made between accuracy and computational time. The field quantities in a FEM element are stored at

- the vertices of the element
- the midpoint of the edges of the element.

Typical storage points and field components in a tetrahedral finite element are shown in Figure 3.8 [61]

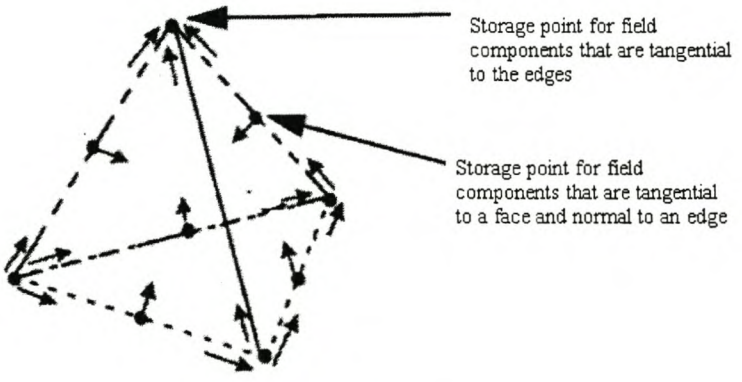

Figure 3.8 Field storage points on a tetrahedron finite element

The field distribution of the elements are described by a Maxwell type differential equation with specified boundary conditions. A functional of the governing differential equation is written. In most cases the integration of the functional is not easily realizable. It is, therefore, recast into a manageable form by using basis or shape functions. This amounts to finding field values at points of the element other than those shown in Figure 3.8 by interpolation. The basis functions are the interpolating functions, they convert the functional into a function.

The simplification of the integrand can be accomplished in several ways giving rise to various formulations of FEM, of which the Galerkin and the Rayleigh-Ritz are among the most widely known.

The expanded integrand is integrated by parts. The resulting equation is either minimized at this stage or is cast into matrix form without minimization. The minimization yields a set of algebraic simultaneous equations. The algebraic equations are written as element matrix equations. The element matrices are used to construct a global matrix equation. If minimization was not carried out earlier, it is done on the global matrix equation. The minimized global matrix equation is solved using conventional methods. The varied views on what constitutes the FEM procedure and the many applications of FEM can be found in an anthology compiled by Silvester and Pelosi [62].

One can write an in-house FEM program or use a commercial one. The ANSOFT HFSS7.0 FEM package was employed in this study.

3.3.1.1 Overview of ANSOFT HFSS7.0 Package [61]

ANSOFT's HFSS is a high frequency structure simulator. It uses the FEM technique to calculate full-wave electromagnetic fields inside a structure. Like most FEM packages, it is composed of three main functional sections namely; pre-processor, processor and post-processor.

The finite element for HFSS is a tetrahedron in which the fields are stored at locations shown in Figure 3.8. Field values are interpolated from the nodal values using zero and first order basis functions. To generate a solution, various software modules which execute special tasks are invoked. The modules, their functions and a few comments are listed below:

- Executive — Coordinates the solution process and provides access to other modules
- 3D modeller — Provides the interface for creating the geometry of the structure under study
- Material manager — Provides the interface for assigning material parameters from the material data base. The most commonly used parameters are: relative permittivity, relative permeability, conductivity, electric loss tangent and magnetic loss tangent. There is provision for defining new materials.

- 3D boundary manager — Provides the interface on which boundaries and sources are defined. The available boundaries are: perfect E, perfect H or natural, finite conductivity, impedance, radiation, symmetry, master and slave. The sources are: port, incident wave, voltage drop, current and magnetic bias.
- Mesh 3D — Generates the initial mesh, refines existing meshes and provides the interface for refining the mesh manually.
- Wave — Computes the excitation modes at each port by solving a wave equation which is derived from Maxwell's curl equation. The port is assumed to have the same cross section as the uniform waveguide to which it is connected.
- abc3d — Computes the 3D solution inside the structure. The solution procedure can be adaptive or non-adaptive and can be a single frequency or a sweep frequency type.
- eigen — Calculates eigenmodes. The solution can be adaptive or non-adaptive and is found at a single frequency.
- Three post processors
  - Fields — For viewing fields as contour, shaded, vector, value versus distance and animated plots
  - Matrix data — For viewing S-parameters, impedance and propagation constant matrices generated during each adaptive process
  - Matrix plot — For time and frequency plots of various parameters.

To run a simulation, the environment for the software modules is created in more or less the order in which the modules have been listed. However, some of the modules are not directly accessible to the user. A summary of the process in which the user is directly involved, is given sequentially as follows:

- Geometry of project is created in the 3D modeller
- Material properties are assigned
- Sources and boundary conditions are defined
- Solution criteria are set up
- Solution is generated
- Post-processing is activated.

More information can be found in the HFSS7 documentation.

This then is the FEM package which is used in the FEM design and simulations described in the following sections.

3.3.1.2 FEM Design

As described in Section 3.3.1.1 above, the first step in the ANSOFT FEM design is the creation of the geometry of the project. A WR340 waveguide of length 610 mm is created in accordance with the procedures of the package. One end of the waveguide is shorted and a port is placed at the other. The port acts as the electromagnetic energy source of frequency 2.45 GHz. One broadside of the waveguide shares a portion of the face of the radiation boundary. The radiation boundary models the cavity of the applicator. Slots are placed on the shared broadside of the waveguide.

From the analytical design, the length of the slot is found to be equal to half a wavelength in the guide. This length is used as the length of the slots. Assuming a sinusoidal wave to be propagating in the guide, the first slot is placed at such a position that its centre coincides with the wave maximum. A slot separation of half a wavelength is used. The design for uniform excitation is then started with two slots at the centre of the broadside axis of the waveguide. A simulation is run and either the return loss or the radiated field pattern is calculated and displayed. Although insertion loss can be used, it is more convenient to measure return loss in the practical stage. For purposes of comparing radiated energy at different offsets, return loss and field patterns are used in this design. The slots are then displaced 5 mm in opposite directions of the broadside axis and a further simulation is run. The opposite displacement is done so that the slots radiate in phase for reasons given in [51]. The displacement-simulation cycle is continued until a maximum in the loss is attained and passed. Displacements of a millimetre are then carried out around the relative maximum in order to get the absolute maximum. A resolution of greater than a millimetre was considered unmachinable with the available resources.

The apparent simplicity of this procedure makes it accessible to non-microwave engineers. However, behind this simplicity is a lengthy complicated FEM computation executed by HFSS.

The FEM design can also be started by placing the slots at the analytically obtained offsets. The slots can then be displaced above and below these offsets in order to optimize for maximum loss. This second procedure does not require as much computer time as the first and is, therefore, recommended. For purposes of comparison, the progressive slot displacement design described above was carried out independently from the analytical design.

With the experience of the two slot design, four, six and ten slot arrays were similarly designed. The results are tabulated in Appendix 3C and are plotted in Figure 3.9.

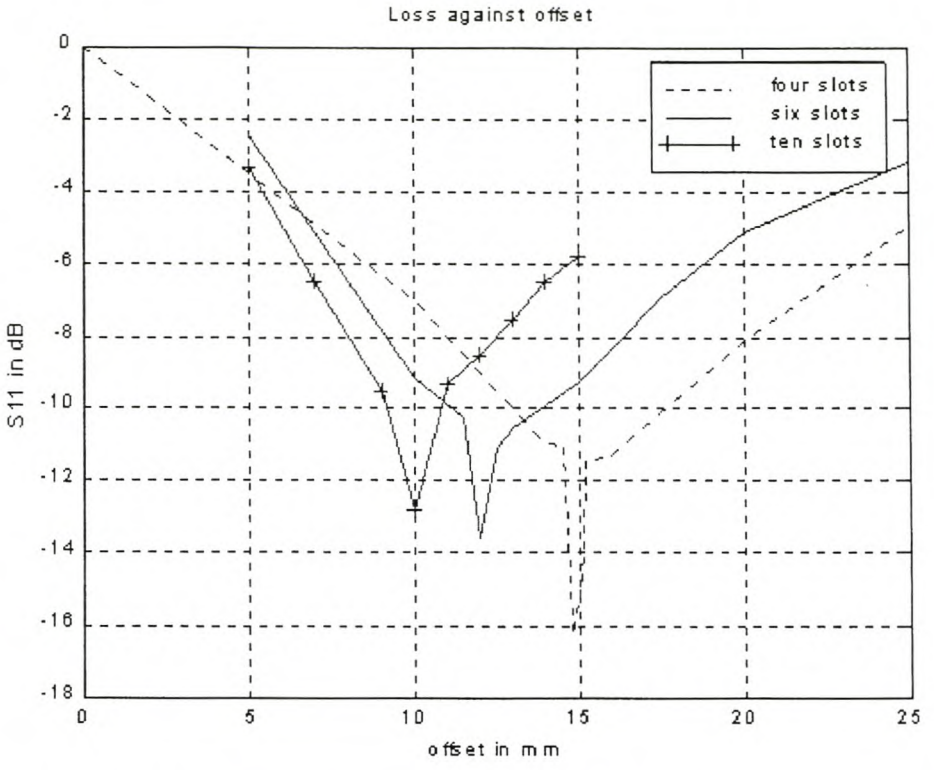

Figure 3.9 Simulated graphs of loss against offset for four, six and ten slots at 2.45 GHz

It is observed in Figure 3.9 that the greatest loss and, therefore, the greatest radiation occurs at an offset of 14.8 mm for four slots, 12 mm for six slots (11.5 mm was obtained analytically without mutual coupling) and 10 mm for ten slots. It can be concluded, therefore, that the greater the number of slots with the same excitation level, the less the displacement required for maximum loss.

The electric field radiation profile for the six slot array near the optimum offset is shown in Figure 3.10. In order to focus attention on the field patterns, the slotted waveguide and the radiation boundary were rendered invisible in Figure 3.10.

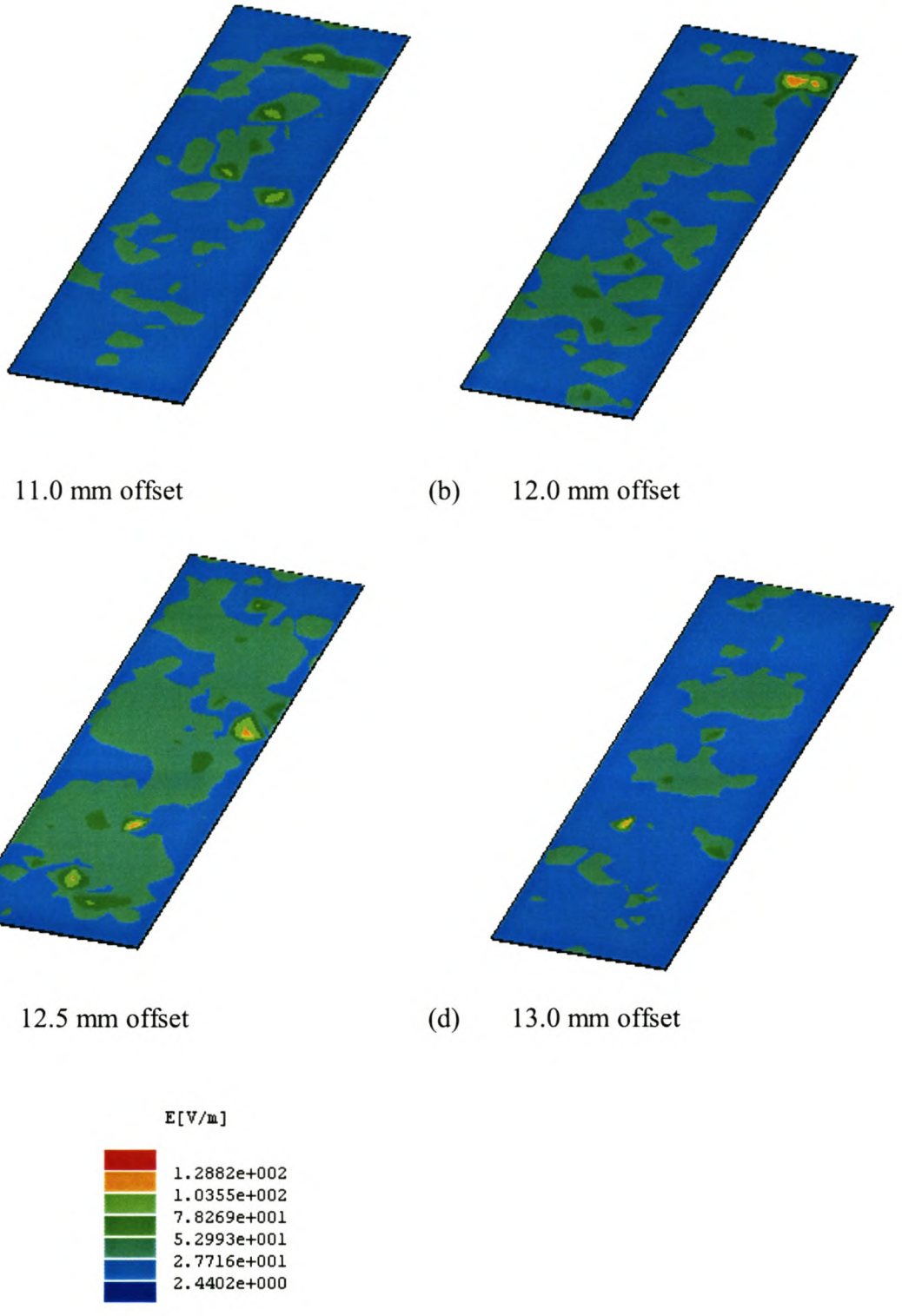

(a) 11.0 mm offset

(b) 12.0 mm offset

(c) 12.5 mm offset

(d) 13.0 mm offset

(e) colour code

Figure 3.10. Electric field pattern radiated by a six slotted waveguide feed designed using FEM displacement method

The field patterns shown in Figure 3.10 are developed on the surface of a thin, lossy and uniform dielectric sheet placed 100 mm from the slots. The sheet is used to aid observation. The patterns are colour coded. The higher the numerical value of the colour the greater the electric field intensity and, therefore, power being represented.

The field profile with a lossy dielectric load shows a maximum radiation at an offset of 12.5 mm. The maximum loss without a load is obtained at an offset of 12.0 mm. This difference can be attributed to the load. Thus each load has a specific slot offset requirement. (One needs to know the dielectric properties of the load before designing a slotted waveguide feeder for it). Since the dielectric properties of a load change with microwave processing, it means that HFSS design of the slotted waveguide feeder must be based on some reference load. The slot offsets in this design are based on radiation in a vacuum.

3.3.1.3 Comparison of the Three Design Methods

For purposes of comparison, three, four-slotted waveguide arrays were designed. The first using an analytical method without mutual coupling, the second using an analytical method with mutual coupling and the third using FEM. Since the analytical methods do not led themselves to easy visualisation, the field patterns of the analytically designed slots were obtained by simulation using HFSS. The patterns developed on the surface of a lossy uniform dielectric sheet placed 100 mm from the slots of the same excitation levels are shown in Figure 3.11.

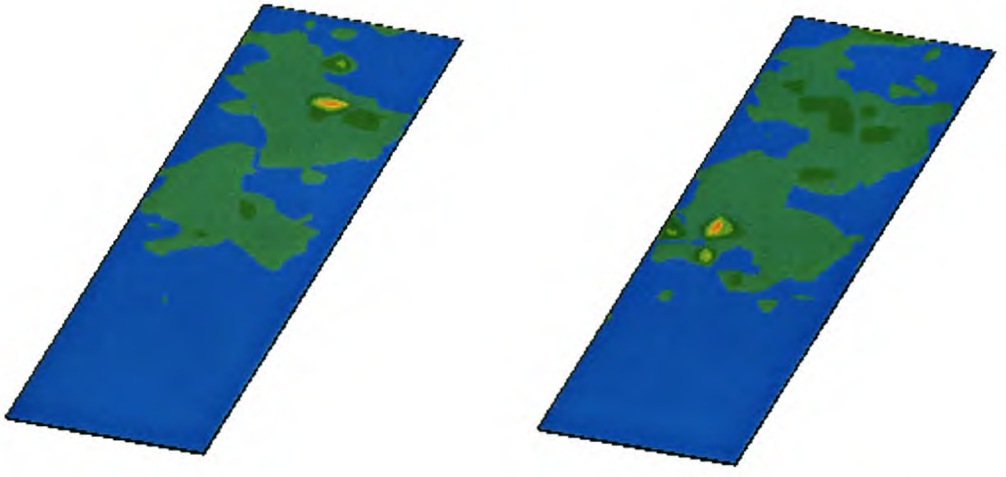

(a) analytical design without mutual coupling; offset 12.7 mm

(b) analytical design with mutual coupling; offset 13.0 mm

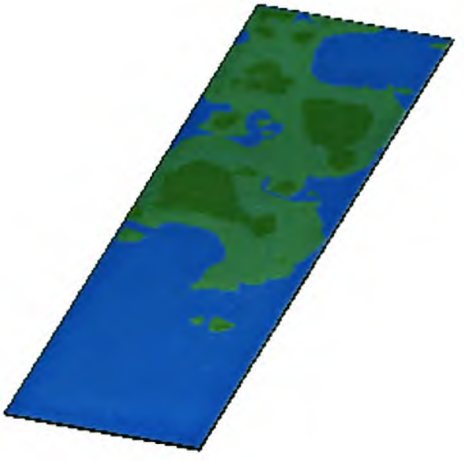

(c) FEM design, offset 14.8 mm

Figure 3.11 Field patterns obtained from three design methods for four slots of the same excitation levels.

The similarity of the patterns in Figure 3.11 show that the three design methods produce offsets which differ by 2.10 mm at most. An accurate design can therefore be started with an analytical procedure without mutual coupling and then optimise for maximum radiation using HFSS. It should, however, be noted that the analytical design does not take the length of the feed guide and the material properties of the guide into consideration. This explains the 1.8 to 2.1 mm offset difference between the analytical and the FEM successive displacement procedures.

Figures 3.10(d) and 3.11(c) are also useful in seeing the effect of four and six slots (at optimum offsets) on the field distribution on a lossy dielectric sheet.

3.4 Dummy Six Slotted Waveguide Feed

To validate the simulations, a dummy slotted waveguide feed designed by Chan [68] was used .The dummy is made from a WR340 aluminium waveguide of length 610 mm with one broadside wall removed. The open-ended edges of the sidewalls of the guide were extended using L-shaped angle brackets. Slots of design specifications were cut on the narrow side of six plates of dimensions 188 × 79 ×1 mm. The plates were placed across the open broadside of the guide with the slots parallel the guide's longitudinal axis. They were secured in place with 141 ×10 mm metal strips screwed down into the angle brackets. The securing was such that the plates and therefore the slots can be displaced from the guide centre-line. Radiating gaps other than the slots were minimized. Figure 3.12 is a picture of the structure. A description of the measurement of radiation from the dummy follows in Section 3.4.1

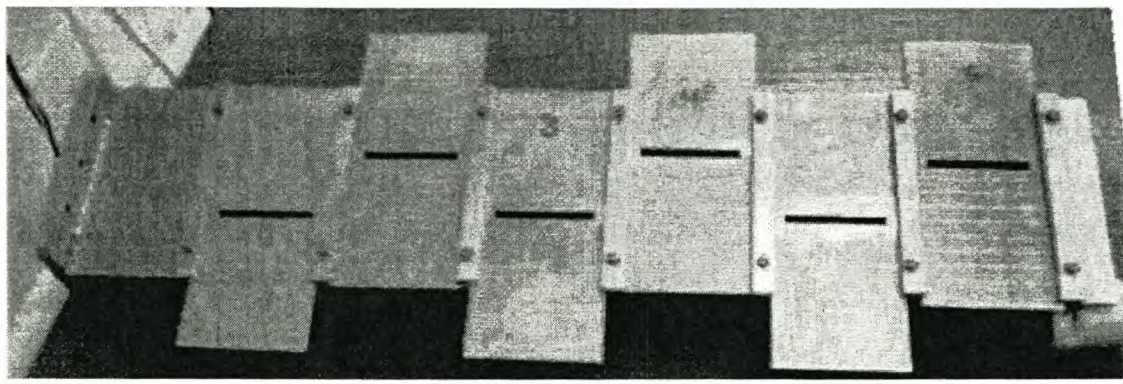

Figure 3.12 Picture of the six slotted dummy waveguide feed.

3.4.1 Experimental Measurement of the Radiation of the Dummy Waveguide Feed

The measurement procedure consisted of calibrating the HP8510C ANA using waveguide standards. A frequency range of 2 to 3 GHz was used. The slots were displaced 12 mm on either side of the centre-line starting with the slot at the shorted end of the waveguide. After making the necessary connections, the return loss was measured while the structure was radiating into space. The plot is shown in Figure 3.14 together with the measured and simulated responses of the real waveguide feed.

3.5 Real Slotted Waveguide Feed for Applicator

A WR340 aluminium waveguide of length 1 120 mm with one broadside open was made on the same lines as that used for the dummy.

Six slots were considered adequate for a continuous process applicator. The slots were designed for uniform excitation using the 61.8 mm length and 6 mm width obtained analytically without coupling. The FEM displacement method was then used to find the offsets. The six slots were cut on an aluminium sheet of length 1 119 mm, width 110 mm and thickness 1.6 mm. The slotted sheet was placed on the open broadside of the guide. The sheet was held in place by screwing it onto the edge of the waveguide so that it was flat with the L-shaped angle bracket. A large aluminium sheet (1 510 mm x 257 mm x 1.6 mm) with a rectangular hole in which the slotted sheet could fit tightly was also screwed on the L-shaped angle bracket. This arrangement, shown in exploded form in Figure 3.13, constitutes one feed side of the applicator. The feed was fabricated as a general purpose one with flexibility for use with other designs and numbers of slots.

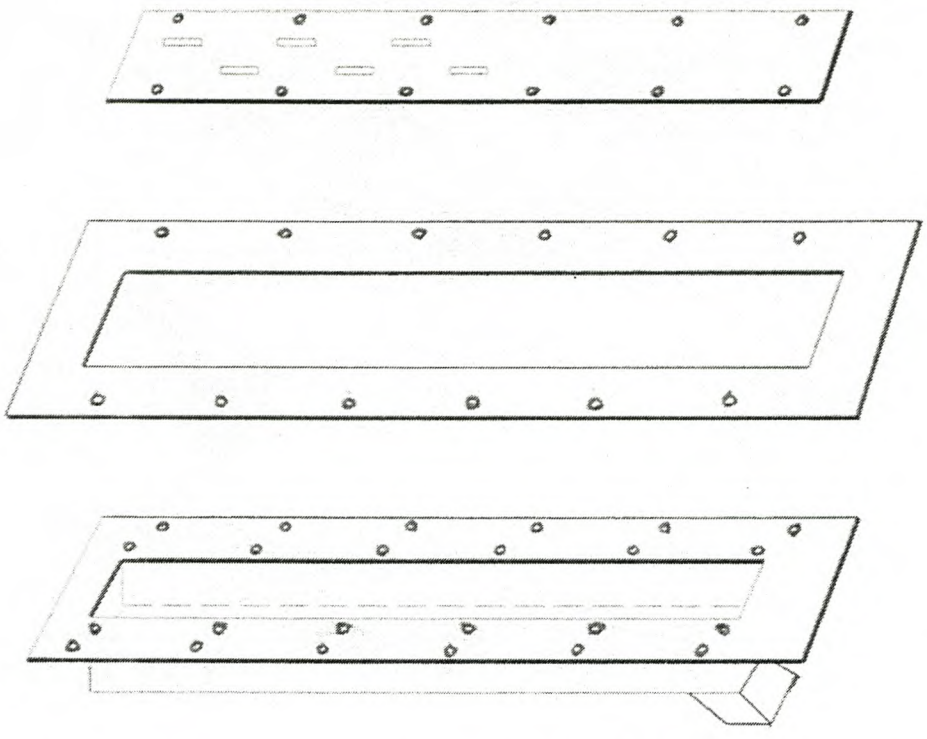

Figure 3.13 Schematic diagram of the exploded feed side of the applicator

The gaps between the assembled sections of the feed side were sealed using an aluminium conductive tape. The slotted sheet can easily be removed and replaced by another.

The loss of the real waveguide feed was measured using the procedure reported for the dummy feed. The response is shown in Figure 3.14.

3.6 Comparison of Measured and Simulated Losses of the Real and Dummy Waveguide Feeds

The simulated and the measured return losses for the six slotted real and dummy waveguide feeds are compared graphically in Figure 3.14.

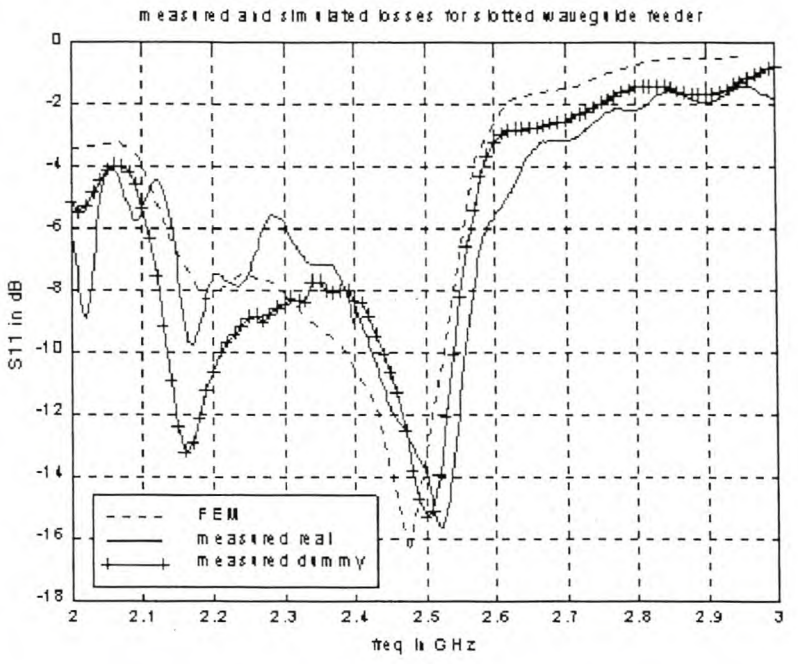

Figure 3.14 Comparison of measured and simulated losses of the dummy and real six slotted waveguide feeds

For the real waveguide feed, the loss at 2.45 GHz is -11.80 dB and the maximum loss is -15.61 dB at 2.52 GHz. This compares well with the loss of -10.66 dB at 2.45 GHz and -15.30 dB at 2.50 GHz for the dummy. In both devices, the measured maximum loss is frequency shifted from the design frequency and is lower in magnitude than the maximum simulated loss. The differences between measurements and simulation can be attributed to measurement errors and the inherent differences between HFSS7.0 and the measurement system. The differences between the real and dummy can be attributed to their differences in construction detail.

3.7 Experimental Investigation of the Field Distribution of the Slotted Waveguide Feed.

The field distribution of the feeds were investigated using two methods: the antenna and the fax paper approaches. The antenna method is used to characterise the "free" feeder and the fax paper method is used when the feeder is connected to the applicator. The antenna approach is described in Section 3.7.1 and the fax paper technique is given in Chapter 4.

3.7.1 Antenna Method.

The performance of the feeder as an antenna was tested by measuring its field pattern using an antenna test facility which consisted of:

- HP 8510C automatic network analyser
- HP 3852A control unit
- stepper motor control unit
- PC for controlling the various sub-systems

- positioner unit housed in an anechoic chamber

The setup in the anechoic chamber is shown in Figure 3.15.

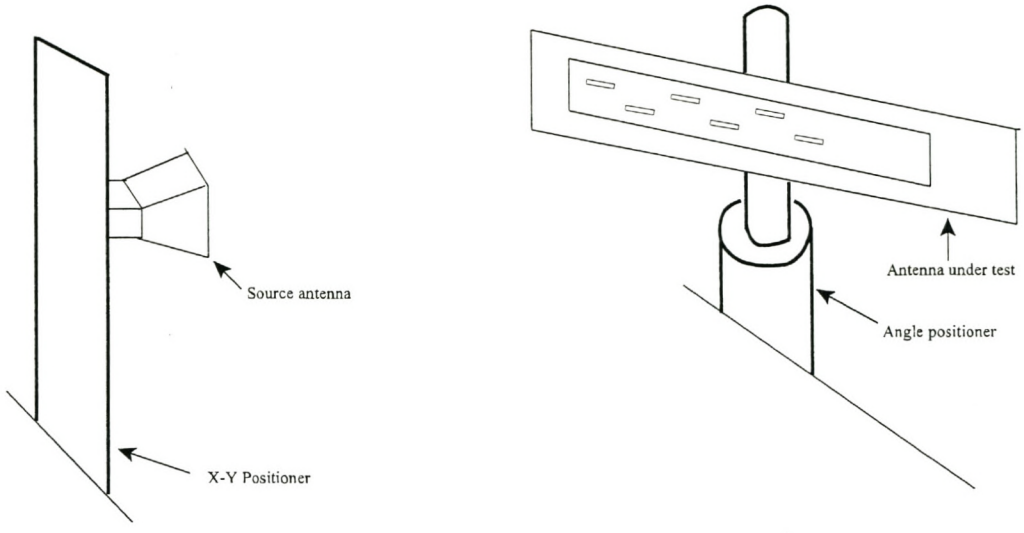

Figure 3.15 Measurement setup in the anechoic chamber

Figure 3.16, page 3.26, is the field pattern which was cut and Figure 3.17 is the HFFS simulated result.

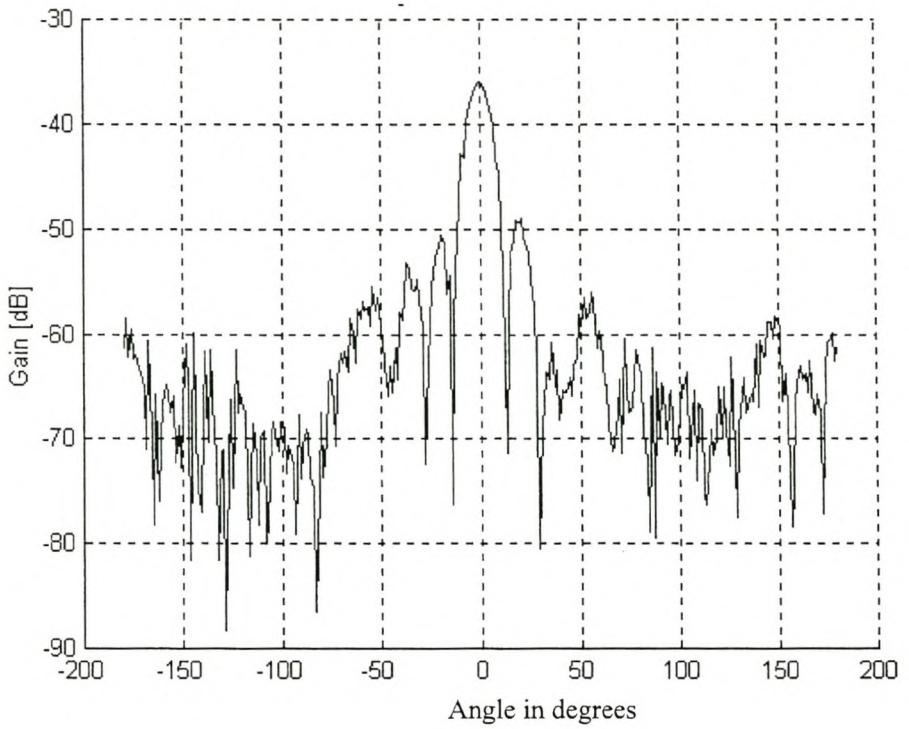

Figure 3.16. Measured gain pattern of the slotted waveguide feed at 2.45 GHz.

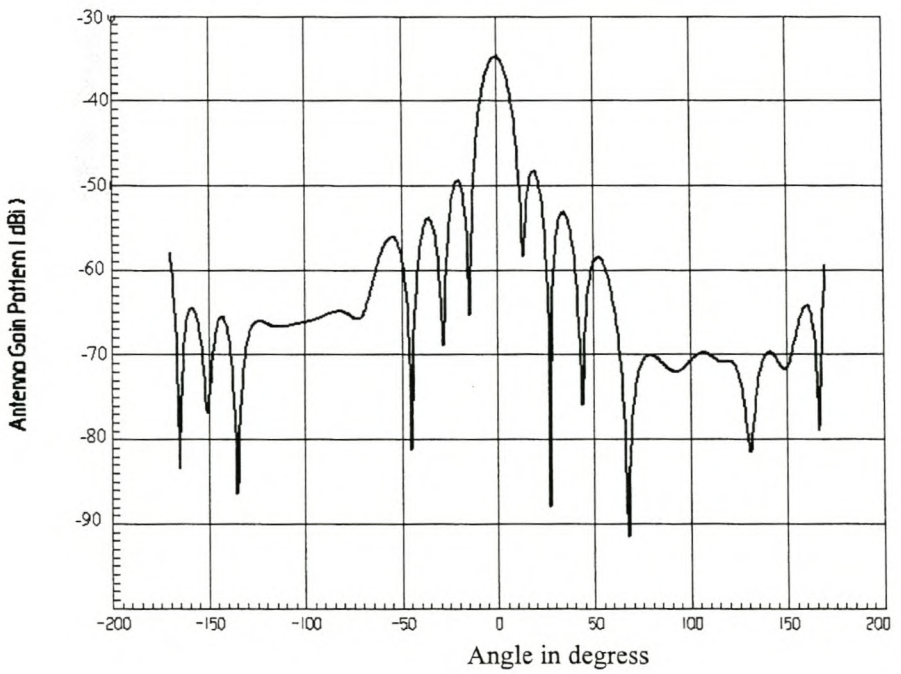

Figure 3.17 Simulated gain pattern of the slotted waveguide feed at 2.45 GHz.

The correlation between measured and simulated patterns is good especially in the -50 to 50 degree region

3.8 Conclusion

A systematic analytical method for designing slots on the broadside of a rectangular waveguide with and without mutual coupling has been presented. The design with mutual coupling has been shown to be computationally involved, but produces offsets which differ by 5 % at most. The method is developed from well established theory and design procedures, however, it is has been extended for the problem at hand. The procedure has been tested against Elliott's method and an independent FEM design.

The design of an applicator is influenced by its intended application. For a continuous processing applicator, in which the modes change continuously with dielectric properties of the load, the slotted waveguide feed can be sufficiently designed using the FEM displacement method. Details of analytical and CAD methods for designing a slotted waveguide feed have been provided in this chapter to make it possible for a designer to make an informed choice.

The performance of the slotted waveguide feed is compared with that predicted by simulation and that of a dummy feed. The radiation pattern has been simulated and measured. The feed and its replica are used in the microwave applicator described in Chapter 4.

Chapter 4

MICROWAVE HEATING SYSTEM: APPLICATOR AND CHOKE CHARACTERISATION

4.1 Introduction

The applicator (also referred to as cavity) is one of the most important components of a microwave heating system. It is in the applicator that the interaction of electromagnetic energy and the workload takes place. The geometry of the cavity and the way it is excited, determines, to a large extent the field distribution and, therefore, the heating uniformity. Considerable design effort has been put into applicators [2][39]. This has resulted in, among others, pentagonal, rectangular and cylindrical shapes. In general, the applicators can be classified as shown in Figure 4.1.

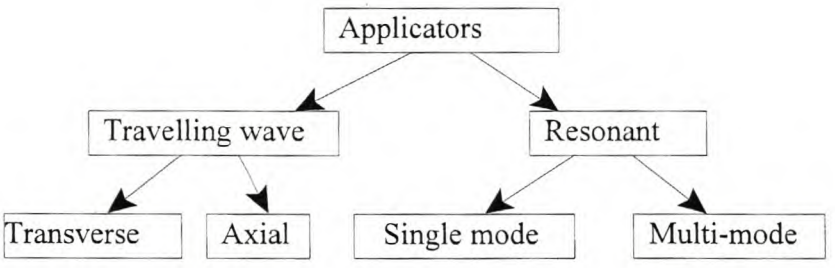

Figure 4.1 Classification of applicators

Single mode applicators can sustain one mode only at a time, however, by either altering the geometry or adjusting the frequency of the microwave source, mode switching can be achieved [63]. Their dimensions are of the same order as the wavelength of the exciting source. The heating is inherently nonuniform.

Multi-mode cavities can sustain many modes at the same time. Multi-mode heating is more uniform than single mode. Several techniques for achieving uniform heating have been investigated, ranging from the basic dimensions of the cavity to modification of the electromagnetic field within the applicator [2][39][63]. Microwave phase control and hybrid heating have also been investigated [64].

In industrial applications, continuous entry and exit of the workload on a conveyor belt is sometimes desired. This requires an open-ended applicator with chokes to prevent or reduce the leakage of microwave energy. To demonstrate the industrial process, a slotted waveguide fed multi-mode resonant cavity applicator with chokes was developed for this study. The applicator and choke are described next.

4.2 Specifications of the Waveguide-fed Applicator

The microwave heating system is made up of the following functional blocks:

- power supply
- two magnetrons with a nominal frequency of 2.45 GHz and a power rating of 1kW. The magnetrons can be turned on independently and are air-cooled through ducts from two fans
- multi-mode applicator of dimensions 1 500 x 247 x 190 mm. The cavity is fed by two slotted waveguide feeds, described in Chapter 3. The slots are inverted mirror images of each other and the feeds are on opposite sides of the cavity
- air system. This consists of a centrifugal blower with an electric motor rated at 125 W and two heating elements rated at 350 W each.

The system shown in Figure 4.2 , can be operated using:

- one feed with or without hot air
- two feeds with or without hot air
- hot air only

The processing of loads can be batch or continuous.

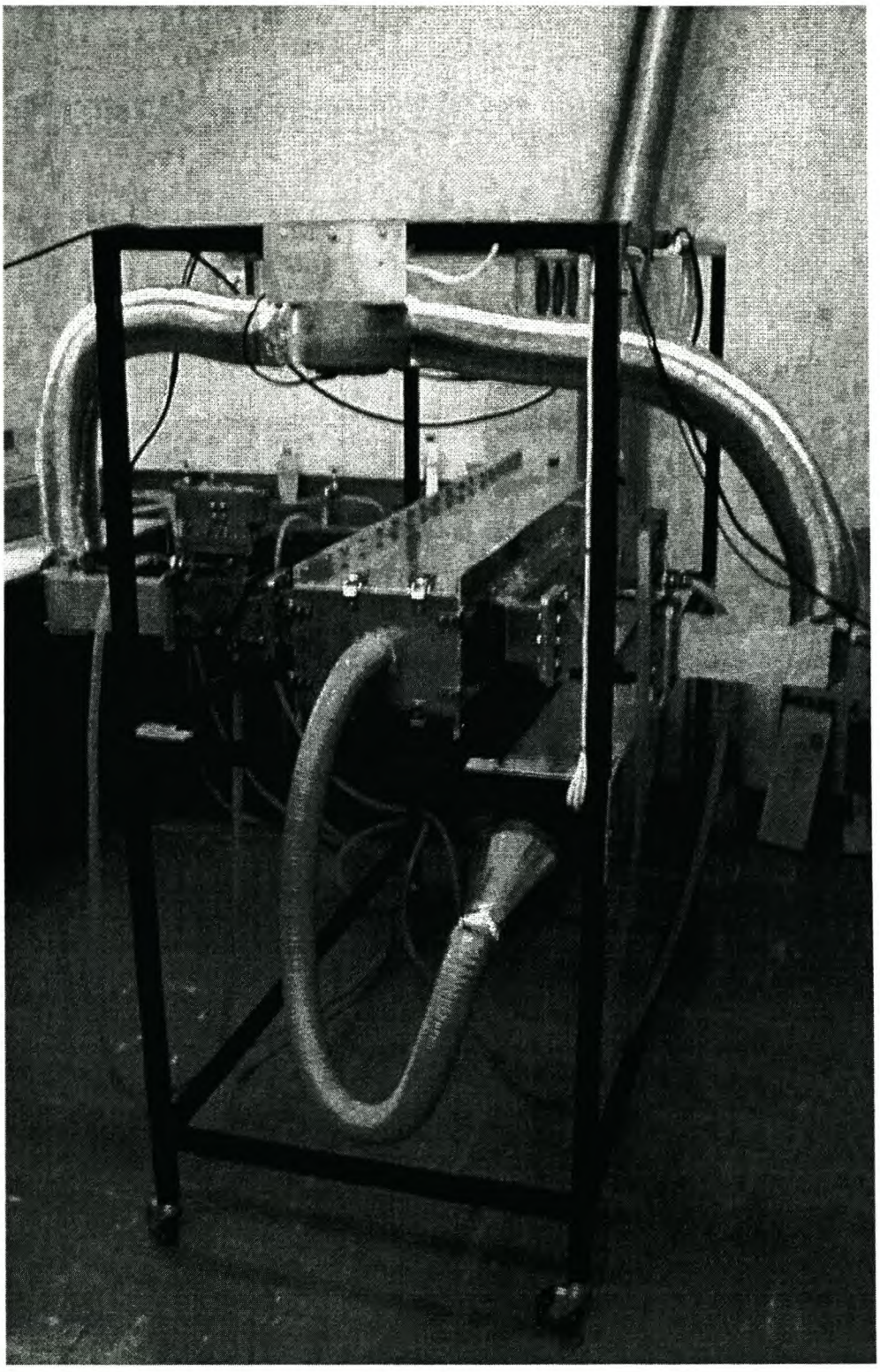

Figure 4.2 Picture of the microwave heating system

4.3 Field Distribution in the Applicator

The field distribution in the cavity is one of the factors which influences heating uniformity. It is valuable to get an insight into this distribution in the empty applicator. The distribution will, however, change with loading and changes in the dielectric properties of the load [39 pp 163]. Various analytical, numerical and experimental methods have been used to map the field pattern in applicators [65]. The most notable ones are:

- calorimetric techniques [66]. These involve measuring the change in temperature of a known mass of material whose specific heat capacity or heat capacity is known over a known period of time.
- fax paper method [67].
- electromagnetic field probing method [68].
- cobalt chloride brick method.
- simulations [65][66][69].
- infra-red imaging.

Experimental methods such as calorimetric, field probing and cobalt chloride are time consuming. Infra-red imaging requires an infra-red camera. Due to its simplicity and quick display of heating patterns, the fax paper method is used in this study. The technique is described in Section 4.3.1.

4.3.1 Mapping of Field Pattern in the Applicator Using Fax Paper

The heat distribution in the "unloaded" applicator was mapped using the fax paper method described by Johnson et al. [67]. The sides of a styrofoam sheet (of dimensions 510 x 190 x26 mm) were covered with fax and teledeltos papers. The papers were tied flat to the styrofoam sheet using a cotton string to form a thermal imaging set. Styrofoam ($\varepsilon'=1.03$) was used to support the papers so that loading of the cavity is due to the papers only. This loading is assumed negligible and the cavity with the thermal set can be described as empty. The set was then placed symmetrically between the slotted waveguide feeds. Figure 4.3 is typical of the heating patterns obtained in 15 seconds with both magnetrons running.

The blackened areas of the fax paper indicate temperatures between 100 and 150 °C [67]. It follows then that the white areas are not necessarily cold spots but are areas where the temperature is below 100 °C. By flipping Figure 4.3(a) from left to right and placing it back to back with Figure 4.3(b), the complete 15 second heating pattern (above 100 °C) between the feeds of the empty applicator can be seen. The complete picture is fairly uniform.

Further details and comments on mapping of heating patterns in a microwave cavity can be found in [93]. The patterns developed in a loaded applicator will be examined further in Chapter 5.

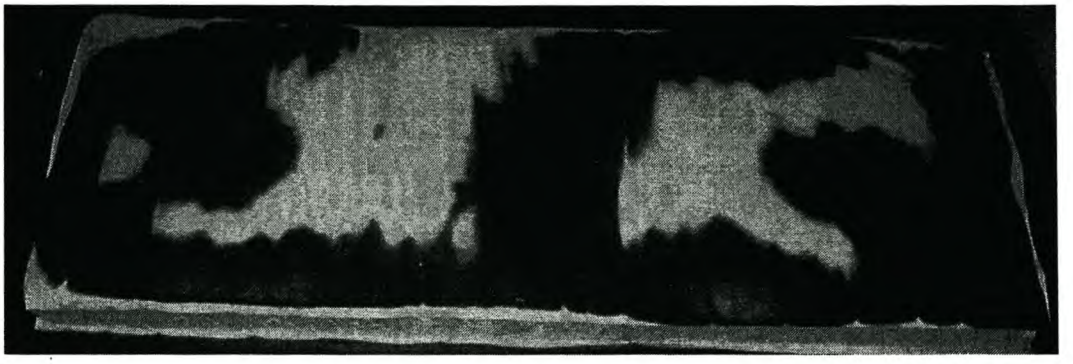

(a) Side facing feeder 1

(b) Side facing feeder 2

Figure 4.3 Fax paper pattern of empty cavity after heating for 15 seconds with both slotted feeds active

4.4 The Choke

It is mentioned in Section 4.2 that the microwave heating system can be operated in the continuous mode. This option requires the continuous entry and exit of the load carried on a conveyor belt. Therefore, the applicator must be open-ended. The dimensions of the open end, 247 x 190 mm, are larger than the 122.45 mm wavelength of the 2.45 GHz magnetrons used in this system. Thus microwave energy will leak out, posing a health hazard to human tissue. To limit the leakage to the recommended exposure level of 10 mW/cm^2 (1-5 mW/cm^2 in some standards) at 2.45 GHz measured at a distance of 50 mm from the equipment [2 pp 278][39 pp 324][70], a choke (also referred to as a filter) is used. Various designs of filters have been investigated and are in use [2 pp 283-294][39 pp 180-187]. The variant used with the applicator of Figure 4.2 was designed by Chris Vale [97] as part of his PhD dissertation. As his interests were purely theoretical, it was decided to implement the design in hardware and use it in the

continuous mode of operation of the microwave heating system.

The schematic of the choke is shown in Figure 4.4 and was designed to the following specifications:

- attenuation of at least 30 dB for all possible propagating modes in particular the TE_{10}.This is the dominant mode supported by the slotted waveguide feed.
- bandwidth of 5% around 2.45 GHz.
- shortest possible length.

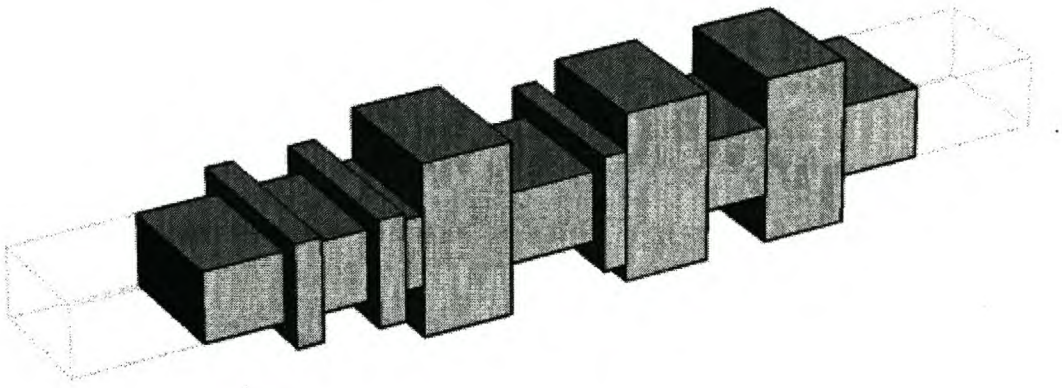

Figure 4.4 Schematic diagram of the choke

4.4.1 Design of a Choke Connected to an Applicator

The design starts by identifying the modes which are most likely to be generated in the applicator when it is excited by a 2.45 GHz source which has a frequency range of 2.4 to 2.5 GHz. Mode-stopping "block structures", each of which is aimed at presenting a propagation zero to one or more modes are designed. In Figure 4.4, the smaller blocks attenuate TE_{01}, TE_{11} and TM_{11} modes and the larger ones attenuate TE_{10} and TE_{20} modes. The performance of each mode is analysed using a mode matching procedure, described in detail in [71].The blocks are next cascaded with the aid of a generic scattering matrix algorithm so that the overall attenuation is within specification. The cascaded block structure is then optimized using a least squares technique.

4.4.2 Experimental Characterisation of the Applicator and Choke

A full-two- port calibrated HP8510C ANA is used to determine the performance of the applicator and choke combination. The combination is treated as a multiport system. The ports are defined as indicated in Figure 4.5 for the applicator with a short and Figure 4.6 for the applicator with a choke.

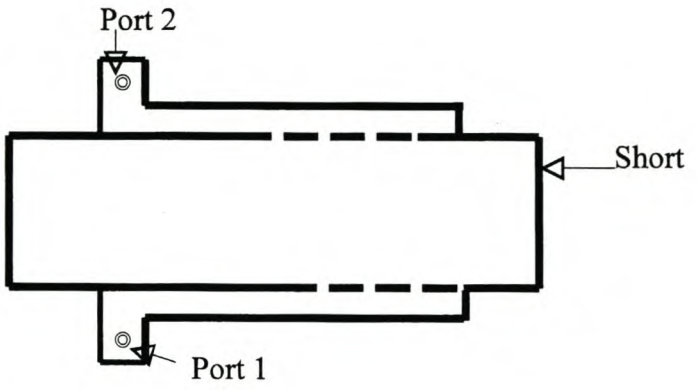

Figure 4.5 Setup for measuring coupling between ports of the applicator with a short

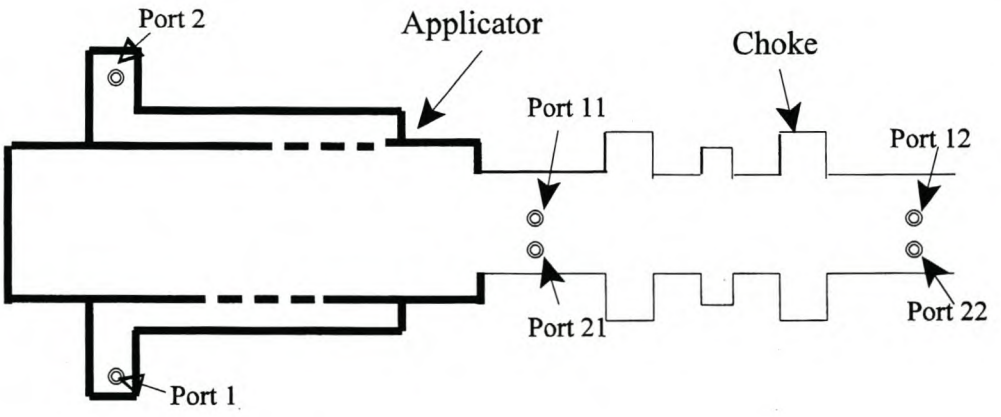

Figure 4.6 Setup for measuring coupling between ports of applicator with choke

The ports are holes big enough for insertion of SMA female connector derived probes. The mount panel of the SMA female connector can be fixed on the port using two small screws. Coaxial cables of suitable length are used to connect the mounted probes to the ANA.

Except in the experiment in which coupling between ports 1 and 2 is measured, the main function of these ports, is to excite the multiport system. The other ports are positioned for probing a number of modes which can be set in the applicator-choke system. Ports 11 and 12 probe the TE_{10}, 21 and 22 probe the TE_{20} and 31 and 32 probe the TE_{01} mode. (Ports 31 and 32 are on the sides adjacent to ports 21 and 22 respectively).

By connecting port 1 to one port of the ANA and port 2 to the other port of the ANA, the coupling between the ports in the calibration frequency range can be measured. The frequency range of 2.2 to 2.6 GHz was considered adequate for assessing the performance of the system

when powered by magnetrons of frequency 2.45 GHz (± 5%). The region of interest in the forthcoming discussions of the performance measurements will, therefore, be confined to the 2.4 to 2.5 GHz frequency range. The other frequencies in the measurement range serve to contrast the performance of the system in and out of the magnetron range. As will become apparent in the plots that follow, the vertical scale changes from figure to figure for clarity.

The measured coupling between ports 1 and 2 of applicator with a short and with a choke are plotted in Figure 4.7

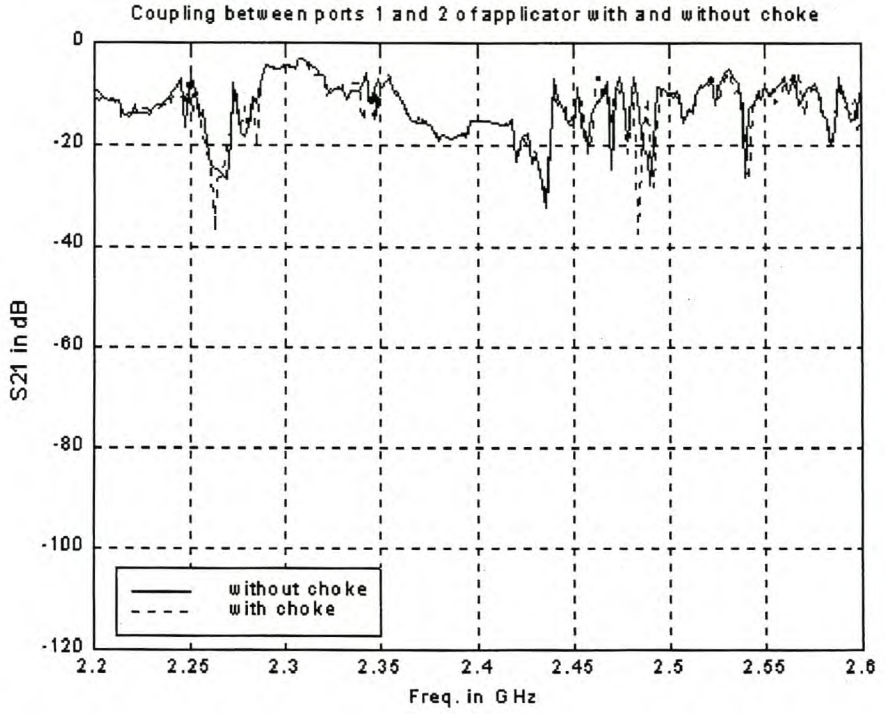

Figure 4.7 Coupling between ports 1 and 2 of applicator with a short and with a choke

The coupling between ports 1 and 2, figure 4.7, is nearly identical. This shows that the choke does the same job as the short, as expected. The coupling is -15 dB in the operational frequency band of the magnetrons. This coupling is high, hence the use of circulators to protect the magnetrons.

Under real operating conditions, the applicator is loaded with wood whose moisture content is continuously changing from high value to low value. To assess the coupling between ports 1 and 2 of the applicator-choke system under the two extremes, green wood (high moisture content wood) and oven-dried wood were placed at the same marked position in the applicator. The dimensions of each piece of pine wood were the same. Figure 4.8 shows the coupling.

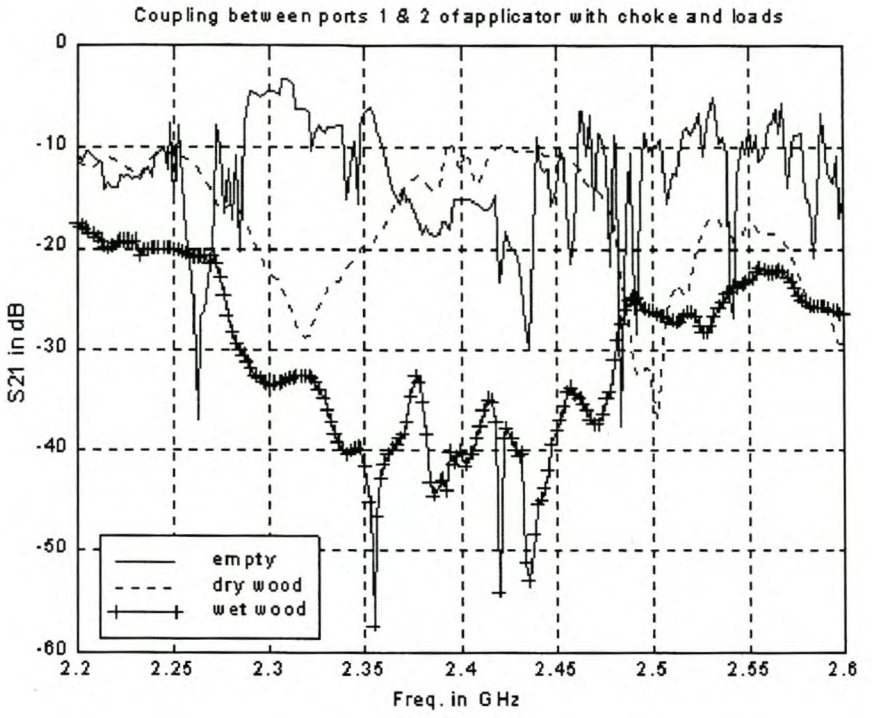

Figure 4.8 Coupling between ports 1&2 of applicator with choke and loads

The plots of Figure 4.8 show that the coupling between ports 1 and 2 is less when the wood is wet than when dry. This is because, in general, wet wood absorbs microwave energy more than dry wood (more on this in Chapter 5). It also appears that dry wood causes more coupling than air in the range 2.38 to 2.47 GHz. This can be attributed to the shift in mode patterns, resulting in a different field distribution being coupled through the slots. The shift in mode pattern should always be borne in mind when interpreting these results.

Ports 1 and 2 excite the applicator through slotted feeds which are inverted with respect to each other. Therefore, they have the potential to excite the choke system differently. The coupling between each applicator port and the ports on the choke was, therefore, measured separately. Figures 4.9 and 4.10 are representative plots of the coupling between the specified ports of the system. The graphs are used to assess the performance of the choke.

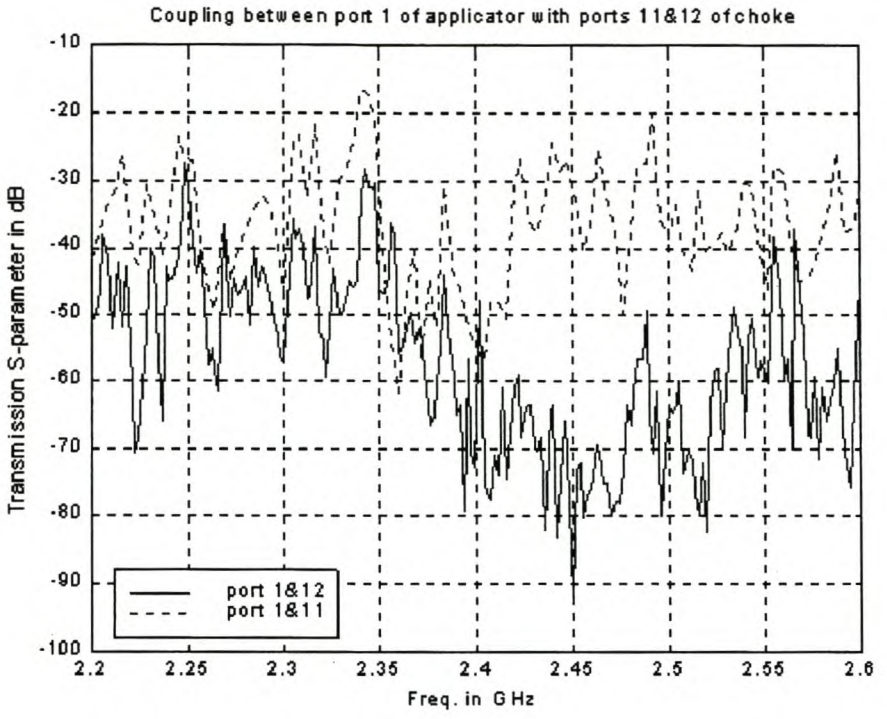

Figure 4.9 Coupling between port 1 of applicator with ports 11 & 12 of choke

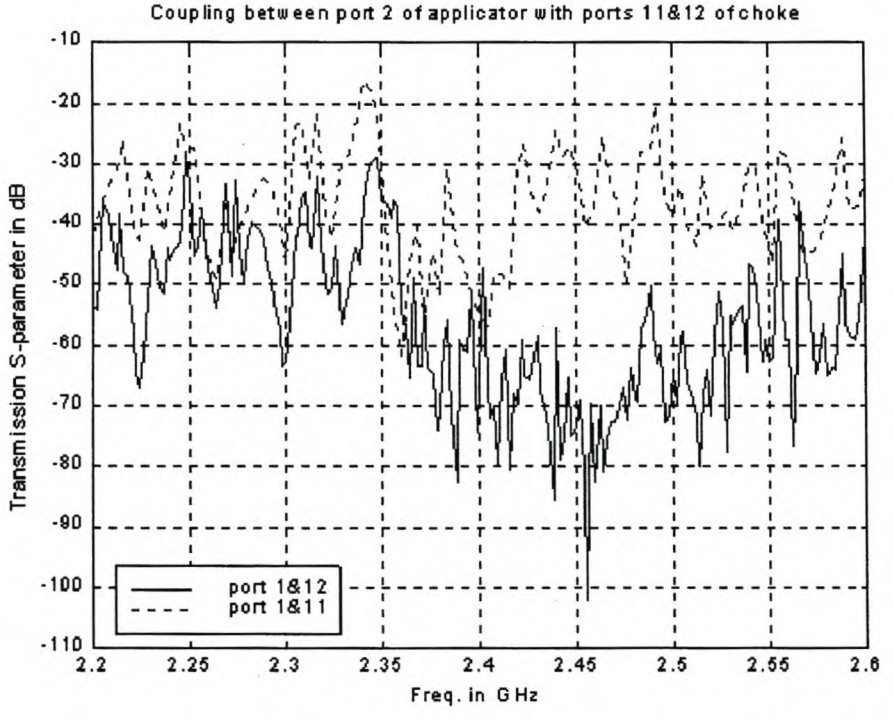

Figure 4.10 Coupling between port 2 of applicator with ports 11 & 12 of choke

In both Figures 4.9 and 4.10, in the frequency range 2.4 to 2.5 GHz, the worst case attenuation by the choke is 10 dB and the best is 30 dB. The attenuation is the difference between the near port (ports 11 and 21) response and the corresponding far port (ports 12 and 22) response. It is interesting to note that the choke achieves the attenuation specified in the design: 30 dB at 2.45 GHz for a TE_{10} mode. However, outside the band of interest, the performance of the choke is not unexpectedly poor. This shows that the design specifications were very tight.

Figures 4.9 and 4.10 also show that the attenuation when applicator is excited through port 1 is very similar to that when excited from port 2. The slight differences can be attributed to difference in the layout of the feeding slots.

The applicator-choke system can also support TE_{20} and TE_{01} modes. The TE_{20} mode can be probed at ports 21 and 22, and TE_{01} mode can be probed at ports 31 and 32. Because ports 1 and 2 coupling to observation ports 11 and 12 have already been shown to be similar in nature, only results with excitation at port 1 are presented for the TE_{20} and TE_{01} modes. The coupling is shown in Figure 4.11 and 4.12.

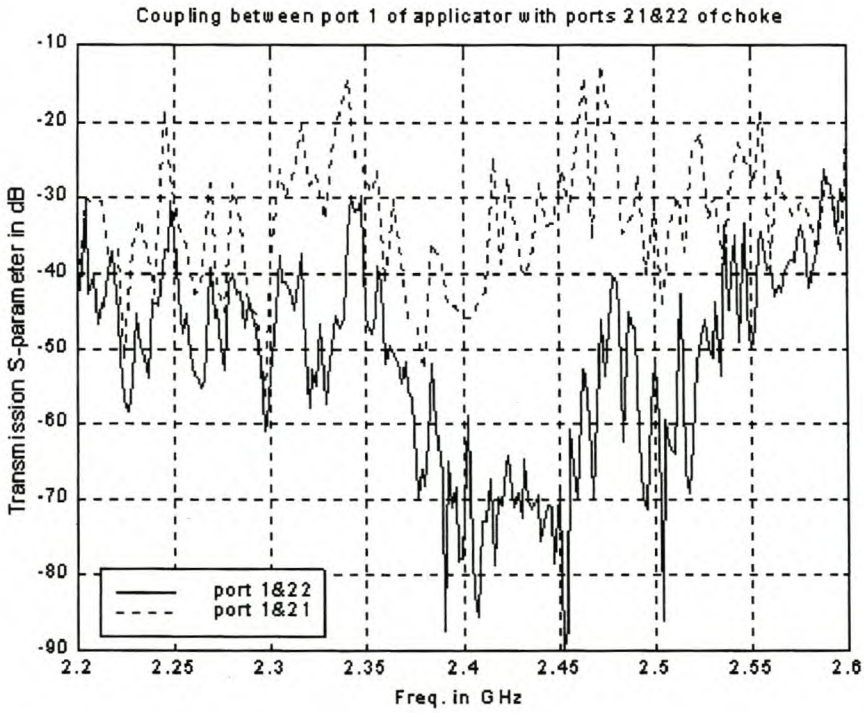

Figure 4.11 Coupling between port 1 of applicator with ports 21 & 22 of choke

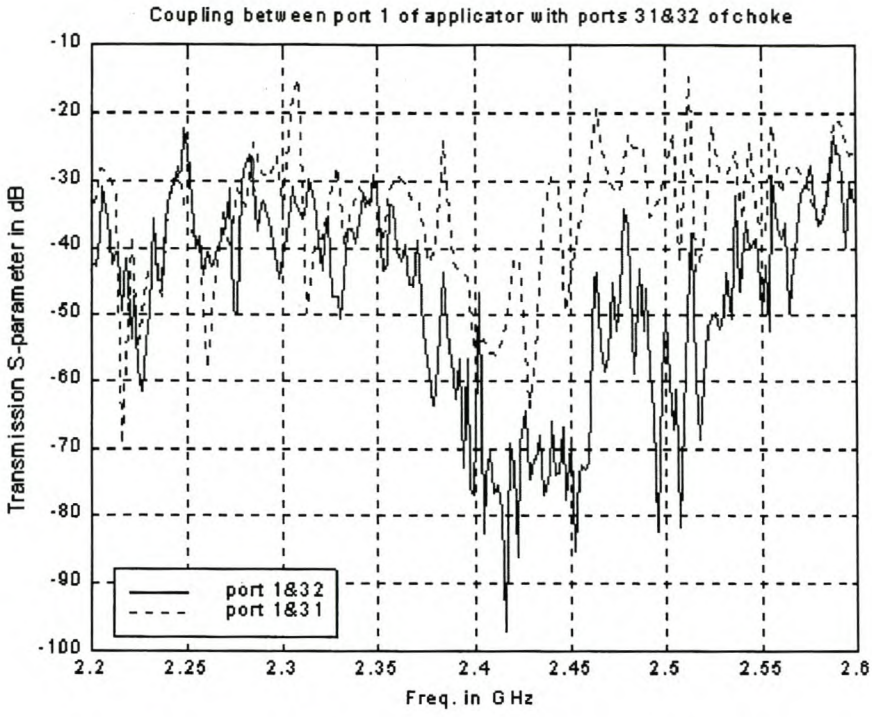

Figure 4.12 Coupling between port 1 of applicator with ports 31 & 32 of choke

In Figure 4.11, the worst case attenuation in the 2.4 to 2.5 GHz band is 10 dB and the best is 30 dB. This is similar to that of the TE_{10} mode in terms of magnitude, though not necessarily at the same frequency. Figure 4.12 demonstrates that the choke is less successful at attenuating the TE_{01} mode.

The response of the choke to TE_{10} and TE_{20} modes is shown clearly in Figures 4.13 and 4.14 respectively. It is obtained by subtracting the near port (ports 11 and 21) response from the corresponding far port (ports 12 and 22) response.

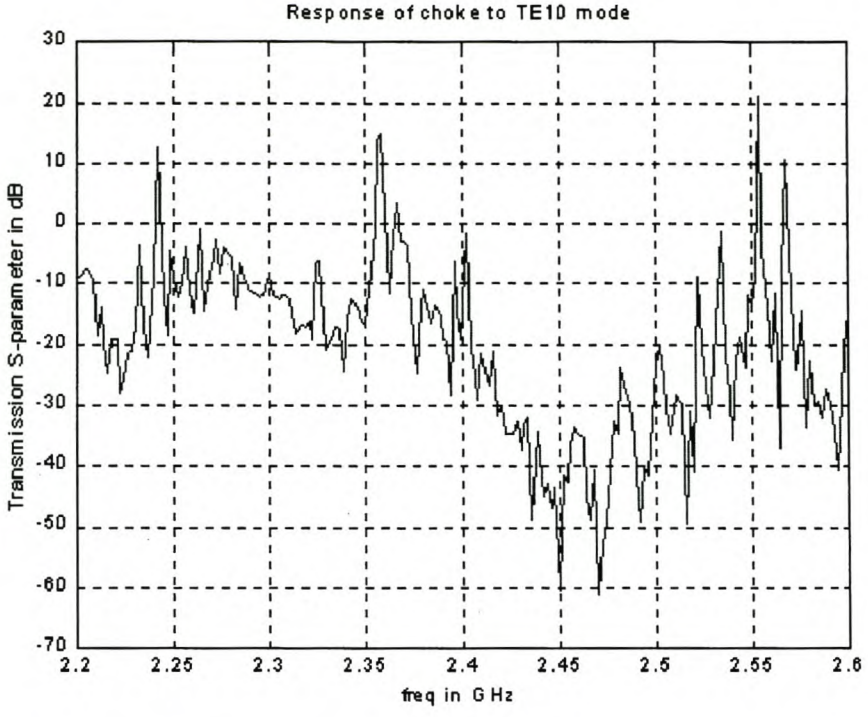

Figure 4.13 Choke response to TE_{10} mode for empty system

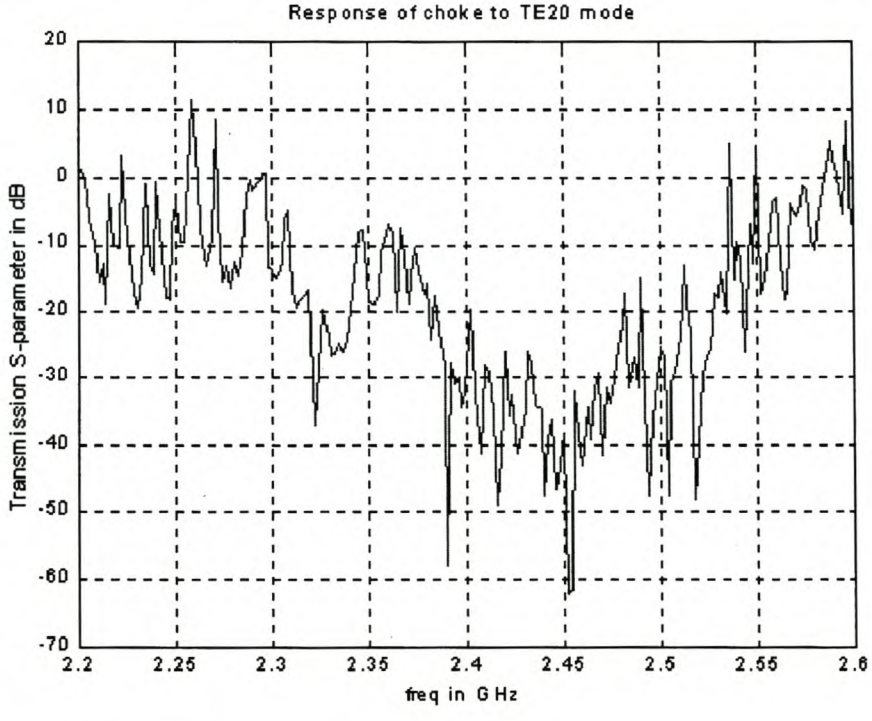

Figure 4.14 Choke response to TE_{20} mode for empty system

When the applicator is loaded, modes which are different from those in an empty applicator are generated [39]. To investigate the response of the choke under these realistic and worst case conditions, the cavity is loaded with a 300 × 150× 40 mm wood block (neither green nor oven-dried). The block is placed lying on the 40 mm side, at two marked positions at the centre of the applicator. Position 1 is when the load is not in front of any of the slots. Position 2 places the load in front of most slots.

Because Figures 4.13 and 4.14 have demonstrated that the choke response to TE_{10} and TE_{20} modes are similar, the TE_{10} response only is presented for the loaded applicator. The response is given in Figure 4.15 and 4.16.

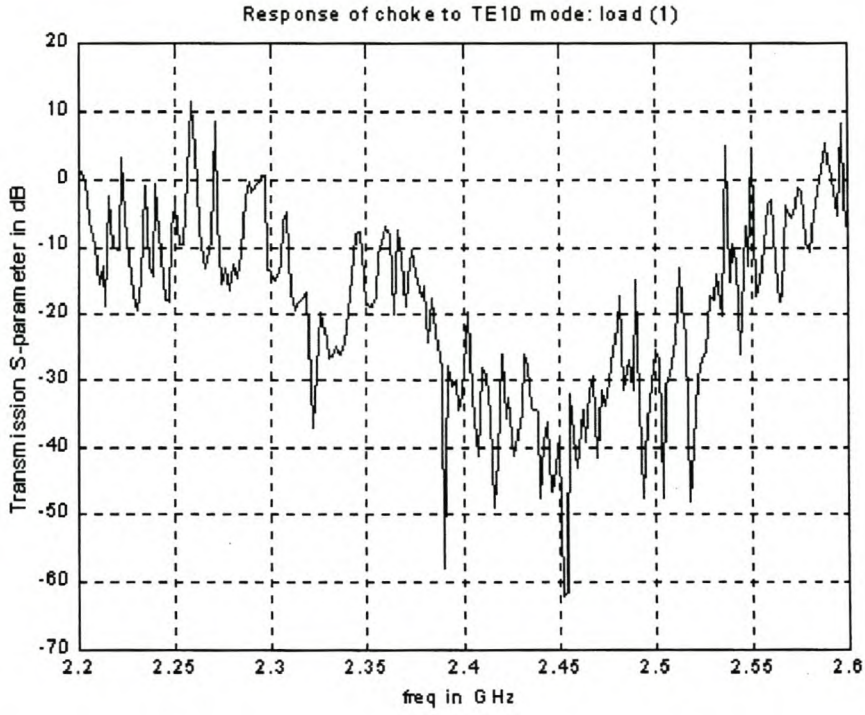

Figure 4.15 Response of choke to TE_{10} mode with applicator loaded at position (1)

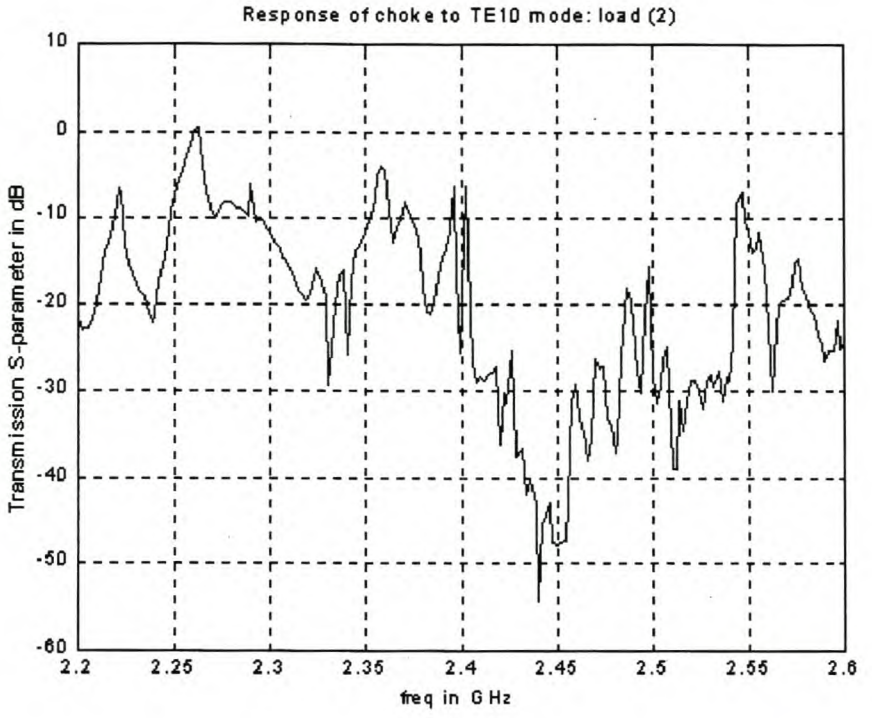

Figure 4.16 Response of choke to TE_{10} mode with applicator loaded at position (2)

In Figure 4.15, the minimum attenuation is the frequency band of interest is 12 dB and the maximum is greater than 30 dB. In figure 4.16, the minimum attenuation is 7 dB and the maximum is greater than 30 dB. These results are not apparently consistent with those obtained for the situations investigated up to this point. This is explained by emphasising that the load perturbs the field in the applicator, generating modes which cannot be easily calculated. The choke is designed to exclude the main anticipated modes.

In the continuous mode of operation of the microwave heating system under discussion, the conveyor belt (made of teflon coated fibre glass mesh with edges reinforced with a 'teflon ribbon') carries the load in and out of the chokes. It is, therefore, necessary to test the performance of the loaded choke. This was done by placing two wood loads (same dimensions as those of anticipated loads) of 'green' and 'oven-dry' moisture contents at two different positions in the choke and then measuring the coupled power between port 1 and the exit ports of the choke (Figure 4.6). Position 1 is when the load has just completely entered the choke from the applicator and position 2 is when it is just about to exit the choke. The power of the TE_{10} mode coupled at port 12 for the two green load positions are compared in Figure 4.17 together with the power when choke-applicator system is empty. Figure 4.18 is the comparison for the oven-dry load.

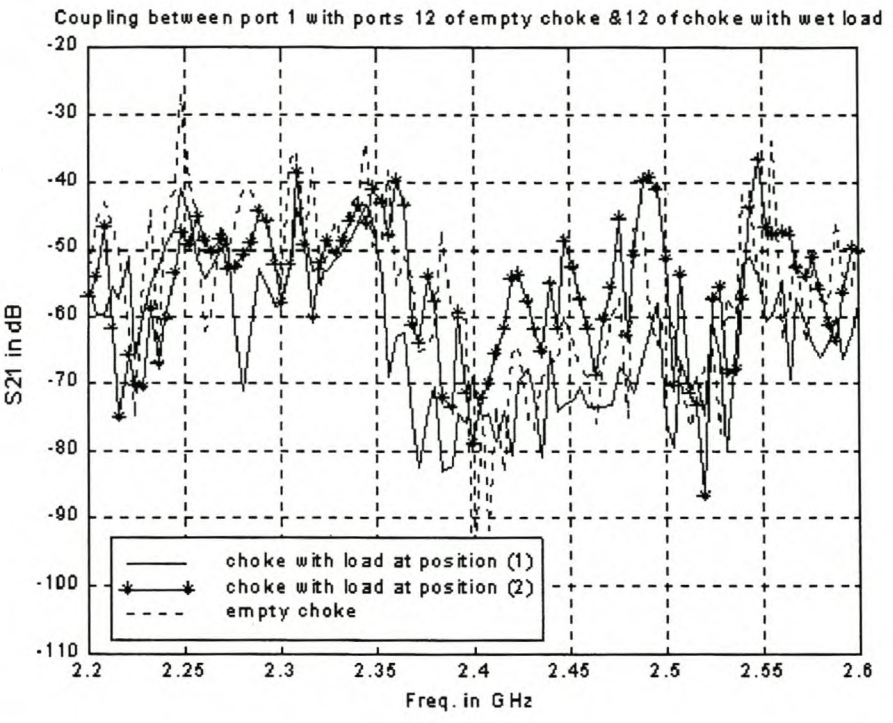

Figure 4.17 Coupling between port 1 of applicator with port 12 of choke: green load

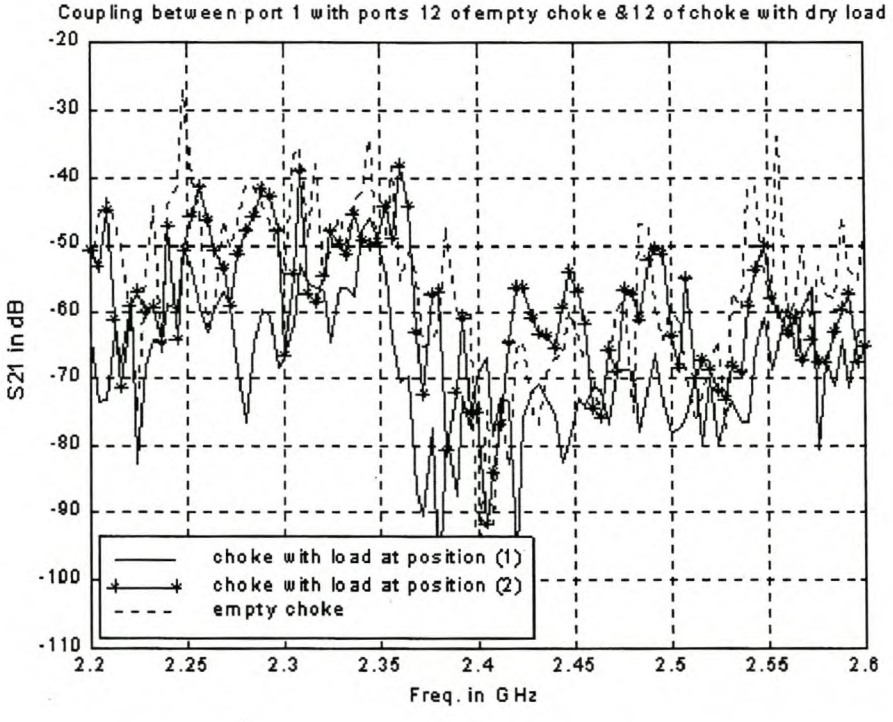

Figure 4.18 Coupling between port 1 of applicator with port 12 of choke : oven-dry load

Figures 4.17 and 4.18 show that the choke is just as effective with and without a load, whether the load has just completely entered or is just leaving it and whether the load is of high or low moisture content. It is, however, evident in the above diagrams that the position and moisture content state of the load, does determine the amount of coupled power. Similar graphs were obtained for the TE_{20} mode.

The high power performance of the choke was investigated by feeding the empty applicator with two 1kW magnetrons at full power in a setup similar to that of Figure 4.6. The power at ports 11 and 12 was measured using a prior calibrated power meter connected to the SMA probe through a 69 dB step attenuator. The reading at port 11 with 30 dB attenuation was -13.69 dBm and at port 12 with no attenuation was -11.22 dBm. Thus the working power attenuation of the choke when the applicator is not loaded is within the 30 dB design specification.

In the interest of safety, the radiation at the open-end of the choke was measured using a microwave survey meter set at its lowest sensitivity of 2 mW/cm^2. It gave a zero reading. This is further evidence that very low power modes if any, exist at the open-end of the choke.

4.5 Conclusion

This chapter described the slotted waveguide fed microwave applicator and the choke. The heat distribution in the empty applicator was mapped using the fax paper method and was found to be uniform. The applicator can be operated in a number of modes. The continuous mode requires the use of an open-ended choke. The design of the choke has been presented and the choke-applicator system has been tested rigorously under high and low power excitation, loaded (load in applicator or choke) and unloaded conditions. The test procedure is novel and simple in the sense that it avoids de-embedding. All tests verify the effectiveness of the choke in preventing the leakage of microwave energy.

The microwave heating system with the choke is used in a mock industrial wood drying process. The process is described in Chapter 5.

Chapter 5

Wood Drying and Moisture Content Measurement

5.1 Introduction

In 735 B.C, Hesoid is quoted by Brown in [72] as having said " as homes of the ancients were so smoky, it must be comprehended how, by means of smoke, they could dry and harden pieces of timber". Thus the drying of timber is an ancient art and through the years, efforts have been made to make the process faster. This study continues the effort, this time by using a section of the electromagnetic spectrum that the ancients did not probably know about let alone use; the RF and microwave regions. This chapter discusses the transport processes in wood, the wood drying process, dielectric heating and the monitoring of moisture content as wood is dried in a microwave applicator.

5.2 Transport Processes in Wood

Wood has a complicated anisotropic structure. The complexities of the micro-structure of wood and, therefore, the complexities of describing water movement (i.e mass transfer), can be appreciated by viewing the electron micrograph of a softwood given in Figure 5.1.

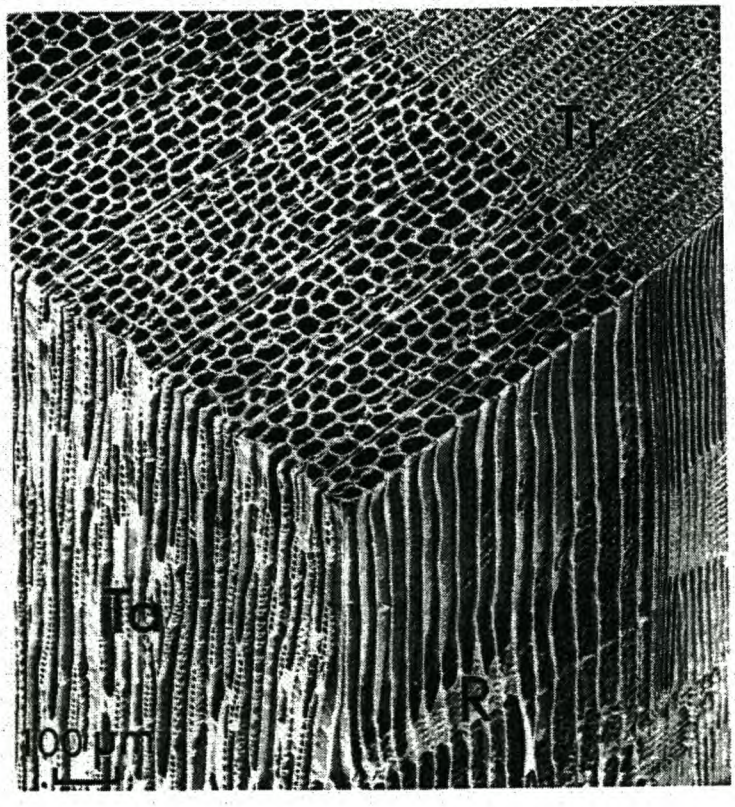

Figure 5.1 Scanning electron micrograph of softwood (after [73] pp27)

The micrograph shows the complex multiple flow pathways for water as it moves out of the micro-structure during drying. Olson [74] studied moisture distribution and flow pathways during the drying of white oak using Magnetic Nuclear Resonance (MNR) imaging. The study revealed that the movement of water during the drying process, is faster along the growth rings than across them. Other experimental techniques which have been proposed for studying moisture movement and distribution are [75] " image analysis, gamma ray measurements, computerized tomography, etc".

The description of water movement is further complicated by the simultaneous occurrence of heat and mass transfer and by the existence of water in wood in three forms. It exists as vapour, free and bound water. Each phase has unique transport mechanisms and properties [76] and is in equilibrium with the other phases. The different phases exist in the many different cells and voids of wood, bound water in the cell walls, free water and vapour in the voids. The cell walls have pits through which water can enter or leave the cell. The pits have different structures, some are open (i.e non-aspirated) and others are closed (i.e aspirated) [77]. The equilibria which exist in wood can be represented by the block diagram below.

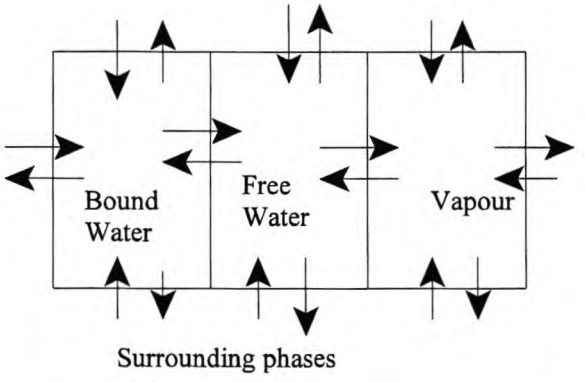

Figure 5.2 Equilibria between water phases in wood

The equilibria which exist in the longitudinal, tangential and radial sections of the wood have different characteristics and are coupled.

5.2.1 The Process of Wood Drying

The "wood water system" is in equilibrium with the water vapour content of the surrounding air. The equilibrium moisture content (EMC) of wood changes with relative humidity and temperature, among other variables. For example, the wood EMC is zero when the relative humidity of the surrounding air is 0% and the wood cell walls are saturated (i.e at 30 % moisture content) when the relative humidity is approximately 100% [78 pg 1].

Thus the drying of wood involves the shifting of the equilibrium point between the water in the wood and that in its surroundings. This is achieved by applying a constraint which reduces the moisture content of the environment and, therefore, shifts the equilibrium points of the wood-environment system towards a lower moisture value in accordance with LeChatelier's principle.

LeChatelier's principle [96] has been stated in various ways which all amount to saying, "if a constraint is applied to a system which is in equilibrium, the system will shift in a direction which tends to nullify the effect of the constraint". In the wood-air system, the constraint can be applied in the wood or in the surrounding air.

Traditional methods of applying the constraint in air use the following techniques:

- leaving the wood in air and allowing the natural movement of air over wood to alter the equilibria in a direction which moves water from the wood. This is the most natural way of drying wood and probably the best in terms of results, but like most things natural, it is not controllable in terms of time. With humankind's desire for speed and control, faster methods have been, and are still being, devised.
- blowing hot air into stacks of wood in kilns. During a kiln drying process, a moisture gradient develops in wood, leaving the surface drier than the core. The moisture gradient causes the water to move out of the wood. The final condition in which the outside of wood is drier than the inside and stress reversal has taken place (i.e surface is under compression and core is in tension) is known as case-hardening. Case-hardening is often reduced by humidification (i.e. raising the relative humidity in the kiln by introducing steam). At the end of a drying schedule, a small undesired moisture gradient remains. The remaining gradient is reduced if not eliminated by equalising, which means the raising of the humidity so as to reverse the drying process for a short time.

There are also reports of studies in which the constraint has been applied to air by

- reducing pressure. This is called vacuum drying.
- drying the air using aqueous solutions of hygroscopic salts or concentrated sulphuric acid [78 pg 18].This is called chemical drying.

Other techniques involve the application of the constraint into the wood itself. This has been implemented in the form of RF and microwave heating. This has the effect of driving water from the inside of the wood by means of a pressure and temperature gradient from the core to the surface. A moisture gradient which is opposite to that developed during kiln drying is produced. Case-hardening does not occur. Thus water can be removed from wood by heating inside (volumetric heating) and by heating the surrounding air.

A wide variety of analytical and numerical models for mass and energy transfer during the drying of wood have been developed [79-82]. The models vary in complexity from one dimensional ones in which energy and mass are not coupled, to two and three dimensional models in which energy and mass coupling is considered. The models have remained largely theoretical. The only applicators which have been used to validate the models at 2.45 GHz are conventional microwave ovens [88] and enlarged waveguide sections [82]. This dissertation reports on the simulated and experimental profiling of the drying of pine wood.

5.3 Brief Theory of Dielectric Heating

The dielectric response of a material to an electromagnetic field is attributed to a number of polarisation mechanisms. The most common ones include [83][84]

- electronic
- atomic
- ionic
- dipole (also known as orientation or Debye polarisation)
- Maxwell-Wagner

At microwave frequencies, dipole polarisation is thought to be dominant. It follows then that materials which contain dipoles or easily polarised constituents are good absorbers of radio and microwave energy. One such substance is water, a constituent of most materials.

Water molecules consist of two atoms of hydrogen and one atom of oxygen. Oxygen is more electronegative than hydrogen (i.e hydrogen is more electropositive than oxygen), resulting in oxygen pulling the bonding electrons towards itself. It, therefore, acquires a negative charge and the hydrogen atoms a positive charge. The unequal sharing of bonding electrons results in the formation of a dipole as shown in Figure 5.3.

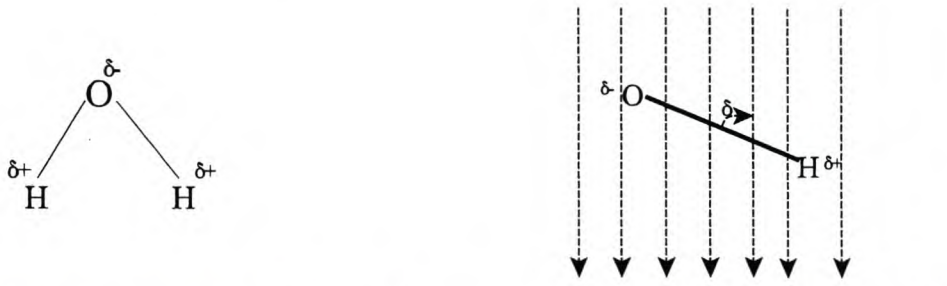

(a) structure of water molecule dipole (b) dipole in an electric field

Figure 5.3 Water molecule dipole and its orientation in an electric field

When a microwave field is applied to a material which contains water or easily polarised molecules (such as cellulose molecules in wood), the dipole will orient itself with the electric field component of the microwaves, see Figure 5.3(b). Since the electric field is oscillating, the dipole follows the field but will lag behind by an angle, the loss angle. It is helpful to view the loss angle as either the angle between the axis of the dipole and the electric field vector or as a measure of the lag in the rise and fall of the polarisation or dipole moment as the electric field rises and falls. The magnitude of the angle depends on the frequency of the electric field. The movement of the dipole back to its rest position is a relaxation process. It is usual to model the relaxation behaviour of the dipole by an equivalent electrical circuit [83][84].

Parallel RC and RCL circuits have been used as convenient analogues. Figure 5.4 shows the simplest of the circuits together with its reduced impedance diagram (also referred to as an Argand diagram).

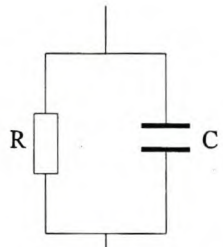

(a) Parallel RC circuit

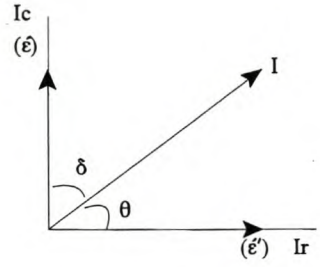

(b) Reduced impedance diagram (Argand diagram)

Figure 5.4 Electrical equivalent circuit and Argand diagram of a dipole

The angle between the resultant current I and the current I_c, Figure 5.4(b), is the equivalent circuit definition of loss angle. The trigonometric relations based on the angle δ and its complement θ on the reduced impedance diagram are often used as a measure of how lossy a material is. The most commonly used is tan δ, the loss tangent (also known as the dissipation factor).

The loss tangent is related to the dielectric properties of the material being heated by [2]

$$\tan\delta = \frac{\varepsilon''}{\varepsilon'} \tag{5.1}$$

The tracking of the electric field by the dipoles is the process that converts microwaves into the kinetic energy of the dipoles and therefore heat. Using the Poynting vector as the starting point, it is shown in [30 pp 29] that the average rate of microwave energy conversion in a dielectric material, is given by

$$P_{ave} = \frac{1}{2}\int_V \omega\varepsilon'' E.E^* dV$$

$$= \omega\varepsilon''|E|^2 V \tag{5.2}$$

From equation (5.2), the average power, P, converted in a unit volume is

$$P = 2\pi f\varepsilon''|E|^2 \tag{5.3}$$

Equations (5.2) and (5.3) show that the rate of microwave energy conversion depends on frequency, the loss factor and the square of the electric field vector. In a microwave heating system such as the one described in chapter 4, f and $|E|$ are fixed by the choice of the microwave energy source. Therefore P in equation (5.3) is directly proportional to ε''. It follows then, that if the power absorbed by a material is determined accurately, the changes in the loss factor as

the material is heated can be monitored. This can be used for online moisture content measurement of wood as it dries during dielectric heating.

Another important parameter in dielectric heating is the depth of penetration given by [39 pp 32]

$$D = \frac{c}{2\pi f\sqrt{2\varepsilon'}}\frac{1}{\sqrt{(1+\tan^2\delta)^{0.5}-1}} \tag{5.4}$$

From equations (5.2) and (5.4), it is evident that the loss factor and frequency determine both the rate of power deposition and the penetration depth. The decrease in the loss factor means that the power converted per unit volume, equation (5.2), will decrease and the penetration depth, equation (5.4), will increase. Knowledge of the values of the dielectric properties of a material can be used to estimate the thickness of the load which can be heated effectively from the onset.

5.4 Dielectric Properties of Wood

Wood is anisotropic at three levels [85 pp 20] namely

- macro-structural (earlywood, latewood, rays, resin canals and vessels).
- micro-structural (cells, cell walls and vessel walls).
- molecular (cellulose, hemi-cellulose, lignin, salts, water and other substances).

All the levels of non-uniformity influence the dielectric properties, as do

- moisture content.
- chemical composition.
- cell and wood structure .
- density.
- temperature
- wood species

A detailed study of these parameters can be found in wood science literature such as [78][85].

Closed form expressions for calculating the dielectric properties of wood are not available. Researchers tend to extract the components of wood and measure the dielectric properties of the extracts and then apply one of the many proposed mixing formulae [85 pp20]. Such studies have shown that the constituent substances of wood have varied dielectric properties. The dielectric properties vary in the longitudinal, radial and tangential directions on each section of wood and also from point to point along the height of the tree.

It follows then that the change in dielectric properties as the wood is heated with microwaves is not the same at various locations. However, investigations of the changes at a particular locality of a plank of wood give invaluable insight into the general trend. The investigations are reported in Section 5.4.1.

5.4.1 Measurement of the Dielectric Properties of Wood

To take into account the anisotropy of wood, samples are cut from three localities of a plank, one metre apart. At each locality, three pairs of samples are cut from a green plank of pine wood. The samples are cut in such a way that under stripline measurement, (chosen for reasons given in Chapter 2) the electric field will be in the radial, tangential and longitudinal directions. The anatomical directions are depicted in Figure 5.5.

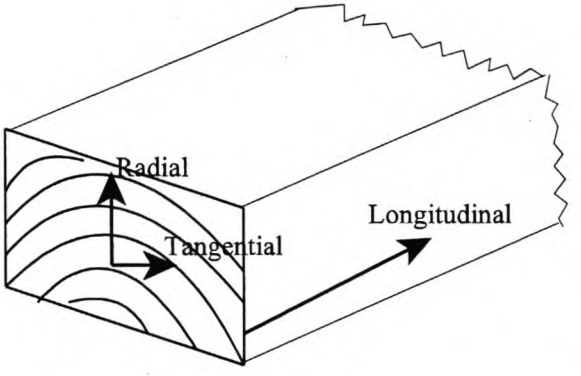

Figure 5.5 Radial, tangential and longitudinal directions in a plank of wood

It is noted in the above diagram that samples which are purely radial and tangential are impossible to cut, hence the samples defined as such are an approximation. Each green sample pair is identified by an *ij* tag, where *i* is the locality and *j* is the direction (samples are further identified by a *measurement session letter* in Appendix 5A). The samples at position 1 for example, are as shown in Figure 5.6.

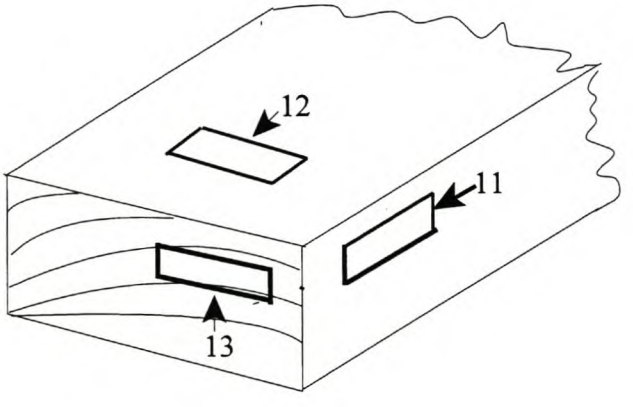

Figure 5.6 Samples at position 1:
11 is the tangential, 12 is the radial and 13 is the longitudinal sample

After cutting, the samples are placed in a thick plastic bag and allowed to equilibrate for six hours. The mass of each sample pair is measured on a digital balance after which the samples are returned to the plastic bag. This is done so that the moisture exchange between samples and

surrounding air is minimal. S-parameters of each pair of a set of samples are measured as quickly as possible on a calibrated stripline-ANA system. Again, exposure of the samples to the environment is minimised. The mass is then measured after the S-parameters have been taken. The average of the mass before and after S-parameter measurement is used as the mass of the sample for which the S-parameters are measured.

The samples (50g average green mass per pair) are then air dried at room temperature and after a significant change in mass, for example 2 grammes, they are placed in the plastic bag and the process already described is continued. When air drying is no longer effective, the samples are dried in an oven at a temperature of 30 °C. After every significant change in mass, the S-parameters are measured as previously stated. The temperature of the oven is raised in increments of 10 °C up to103 °C . The constant mass obtained at 103 °C is taken as the oven dry mass of the sample.

Moisture content is then calculated on a dry basis using [39 pp 351]

$$MCDB = \frac{\{current\ mass\ of\ sample - (oven - dry\ mass\ of\ sample)\}}{oven - dry\ mass\ of\ sample} \times 100\% \qquad (5.5)$$

The permittivity and the loss factor are calculated as described in Chapter 2. The graphs in Appendix 5.A show the variation of the dielectric properties with frequency at different moisture contents.

The following discussion is based on sample 12, Appendix 5.A.1 (extracted from Appendix 5.A.2 in order to facilitate the discussion). Any sample could have been chosen, however, during heating in the applicator, it is the radial side of the plank which is placed directly in front of the radiating slots.

The following observations can be made from the sample 12 plots:

- ε' decreases as moisture content on a dry basis decreases and also as frequency increases. (The variation of permittivity with moisture content for sample 12 is shown clearly in appendix 5A.1.1) The decrease with increase in frequency is evidence of dielectric relaxation [87]. As moisture content decreases, the rate of change of ε' with respect to frequency decreases. This implies that relaxation is becoming less pronounced. It can, therefore, be concluded that the relaxation in the wood samples under study is dominated by water related dipoles.
- loss factor plots show some resonance. The resonance shifts to higher frequencies and then flattens out as moisture content decreases. The shift can be used to indicate change in moisture content.

In addition to the comments made on sample 12, the following can be said about the set of graphs in Appendix 5.A.2:

- anisotropy of wood is evident;
  - corresponding samples (e.g radial samples,12, 22 & 32) which have been exposed to the same environmental conditions have different moisture contents and

dielectric properties.

- samples at the same locality but of different orientation (e.g 11, 12 &13) which have been exposed to the same environmental conditions have different moisture contents and dielectric properties.

- ε' for high moisture content samples has a minimum in the 2.0-3.0 GHz frequency band. This suggests the end and the onset of different microwave-wood interaction mechanisms. The mechanism below the frequency at which the minimum occurs, is dominated by water dipoles.
- corresponding samples (eg 12, 22 & 32) have similar plots.
- longitudinal samples have the highest real part of permittivity at a particular locality.
- radial and tangential samples at the same locality (eg 11 and 12) have similar values for the real part of permittivity. The values are actually the same at low moisture contents. N.B. Observations pertaining to permittivities of longitudinal, radial and tangential samples are consistent with the values tabulated by Zhao et.al.[82]
- the flattening of the graphs at low MCDB indicates the levelling in the moisture content.
- the rate of change of MCDB is on average 24.33 % per day with sample 12 having the lowest rate at its locality.

The dielectric properties just described are used to simulate the interaction of 2.45 GHz microwaves with wood of specific a moisture content. The variation of dielectric properties with moisture content is the basis of a proposed moisture content measuring system in Section 5.5.1. The simulations are reported in Section 5.4.1.1.

5.4.1.1 Experimental Investigation of Moisture Distribution in Drying Wood

A number of studies have been published in which the heat distribution (and therefore moisture content) in wood is mapped using fibre-optic thermometers [79][88]. The thermometers are inserted in holes drilled in the wood. This approach interferes with the drying process and is destructive. A non-invasive method is thermal imaging. This has usually been done using an infra-red (IR) camera [92]. In the absence of an IR camera, fax paper is being proposed as an alternative for wood studies. The mapping of heat distribution in wood at different moisture contents using fax paper is given in Appendix 5.B.

In reports [79] and [88], the experimentally determined heat distribution is compared with that from models for which the dielectric properties are sourced from literature. In this dissertation, the dielectric properties used in simulations are obtained from measurements reported in section 5.4.1. The values of ε' and ε'' at different moisture contents can be read from each plot or more accurately, taken from arrays used in the plots. Values obtained using the latter at a frequency of 2.45 GHz are used to simulate field distributions in drying wood using HFSS 7.0. Because the electric field is related to the power generated (equation 5.3) and the power is related to heat, it means that practically obtained heat patterns can be compared with simulated electric field distributions.

The computational and practical procedures (and results) used to investigate the heating patterns in wood are given in Appendix 5.B.

From the fax-paper mapping and simulation experience of Appendix 5.B, it can be concluded that:

- moisture distribution in drying wood cannot be mapped easily.
- computed field patterns from which heat distribution can be derived, cannot be correlated to experimentally determined heat distribution easily. However, computed trends have been demonstrated experimentally.
- distribution of moisture in wood depends on the moisture content. At high MCDB , the water is non-uniformly distributed. This leads to localised heating by microwaves.
- uniform distribution of moisture in wood of the lowest possible MCDB, can be shown accurately by fax-paper and simulated patterns.

To minimise localised microwave heating, the wood load must be moved in an inevitably moded , slotted waveguide fed applicator. The heating of wood as it moves on a conveyor belt through a microwave applicator is investigated experimentally in Section 5.5.1. However, before a quality product can be produced, optimum processing procedures must be established. This has been done by developing drying schedules in Section 5.5.

5.5 Development of Microwave-Air Drying Schedules for Wood

The steps used in the drying of wood using any technology are referred to as a drying schedule. Before the technology is used commercially, a schedule must be developed. This section presents the development of a microwave-air drying schedule.

The schedule is developed by investigating the drying times of wood using different combinations of microwaves and centrifugal pump blown air at different temperatures in a setup shown in Figure 5.7. However, one has to determine the thickness of the wood which can be processed effectively from the onset first. To get the thickness, values of ε' (= 4) and ε'' (= 1) of sample A12 at 2.45 GHz are substituted into equation (5.4). This gives a penetration depth of 39.20 mm. Planks which are 40 mm thick are used in developing the schedules and in the mock industrial drying process.

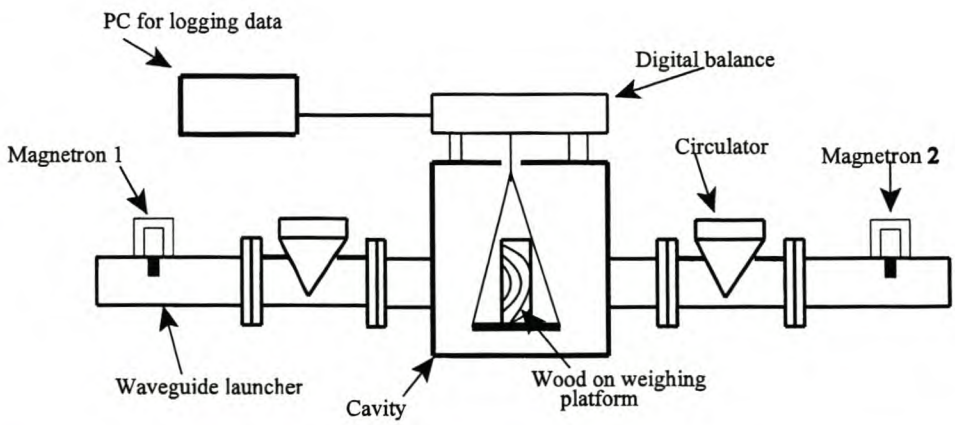

Figure 5.7 Setup for developing drying schedules of wood.

The system consists of the slotted waveguide fed applicator, a weighing scale, sample holding platform and a computer running a data acquisition software. The measurement procedure is as follows:

- weighing platform is hooked to the bottom of the scale and the scale is zeroed.
- 500 x 110 x 40 mm green plank is placed on the platform so that it is horizontally balanced and is as close as possible to the receiving slots without affecting the accuracy of mass measurement. The width and length of the plank is such that it covers the slotted section of the receiving waveguide feed. The plank is irradiated in the radial direction.
- extraction fan and cold air blower are turned on.
- water supply to circulators is turned on and one magnetron is fired.
- data acquisition program is run. The program logs in the mass of the plank at one second intervals.

The following combinations of microwaves and air were used to develop the schedules:

- two magnetrons and air at room temperature.
- one magnetron and air at room temperature.
- one magnetron and hot air.
- hot air (i.e centrifugal pump blown hot air).

The results are compared in Figure 5.8.

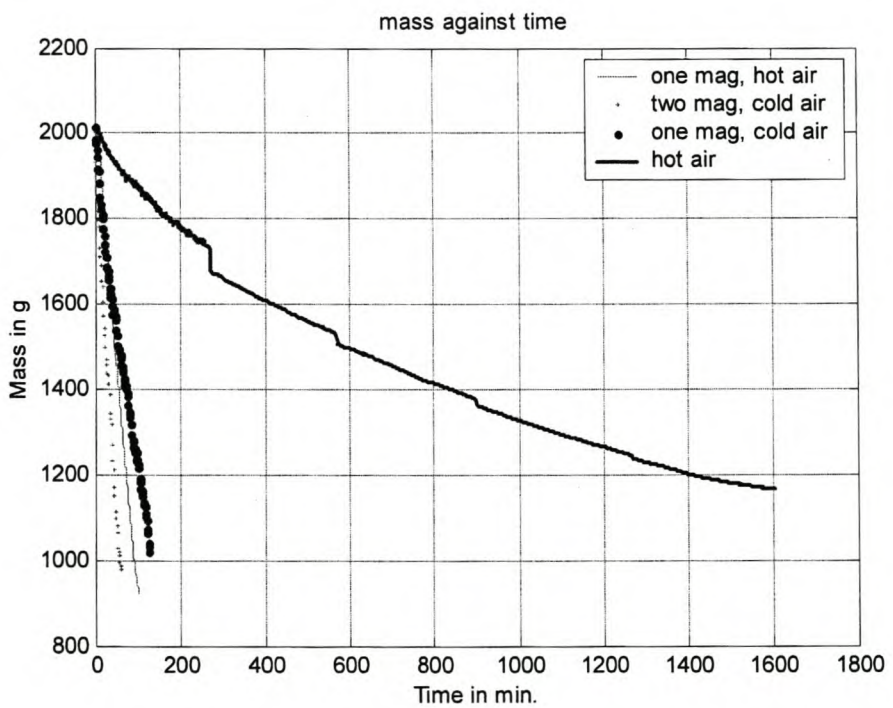

Figure 5.8 Drying runs using different energy sources

The starting masses and, therefore, moisture content of the planks used to develop the schedules were not necessarily the same. It is difficult to cut planks of exactly the same mass. Therefore masses around 2 000 grammes were used as starting masses in the plots. This has a small bearing on the results. Other factors which may influence the drying rates include:

- anisotropy of wood (i.e whether side facing slots is tangential or radial).
- ambient conditions.
- wood density

The limitations indicated above are so insignificant that the comparison of drying schedules in Figure 5.8. remains valid.

The differences in the drying rates are due to the nature of the drying processes. The dominant moisture removal mechanisms are capillary flow and diffusion which, in theory, could be opposed by a temperature gradient. Application of microwave energy generates heat in the wood at a rate given by equation 5.3. The moisture is removed by a positive temperature gradient, capillary flow and diffusion from the inside of the wood and by air (cold or hot) from the surface. This process is faster than when using hot air alone. Hot air (alone) heating removes moisture from the surface of wood resulting in the creation of a moisture gradient and, therefore, diffusion.

Figure 5.8 shows that the decreasing order of drying rates is obtained from the following combinations:

- two magnetrons and air at room temperature.
- one magnetron and hot air.
- one magnetron and cold air (air at room temperature).
- hot air.

The hot air drying curve was obtained over a period of five days. The start of each drying session appears as a discontinuity in the curve. Magnitudes of discontinuity steps were reduced by placing the plank in a plastic bag in between drying sessions. The hot air curve shows the three main stages in the drying of wood; the fast rate, falling rate and the constant rate. These stages are not obvious in the other drying curves.

The following observations were made during the course of the experiments:

- green wood can be dried by microwaves up to half its green mass without charring. This applies to both hot and cold air combinations. Heating to below half the green mass results in both charring at certain spots and collapse (wood ruptures and a crater is formed). This implies that microwaves localise moisture in wood of less than half the green mass instead of levelling it. Up to half the green mass, the product is devoid of checks.
- drying with hot air alone results in checks.
- drying with microwaves only results in condensation in the applicator.
- knots in wood result in extrusion of resins around them and eventually in collapse.
- boards with defects and very different wood types develop hot spots at high moisture content (dry basis). Thus only boards with one wood type can yield a high quality product when processed using a drying schedule developed from similar wood types.

From these observations, it is recommended to dry green boards with very similar, if not the same wood types, to half the green mass using microwave-air or microwave-hot air combinations and then use hot air with periodic application of low power microwaves. This procedure was used to produce a 10 % MCDB product which was found to be uniformly dried, without checks and warp.

5.5.1 Mock-up Industrial Wood Drying System

Simulations and fax paper patterns in Appendix 5.B showed that microwave heating of green wood is localised. Section 5.5 established that a combined microwave and hot air drying schedule is the fastest. It also established that schedules can be changed as the heating progresses. The two experiences are now combined in a demonstration of "the industrial drying of wood using microwaves and air".

Four samples of wet wood were marked and weighed. They were then placed on a conveyor belt just before the entrance choke, one at a time, Figure 5.9.

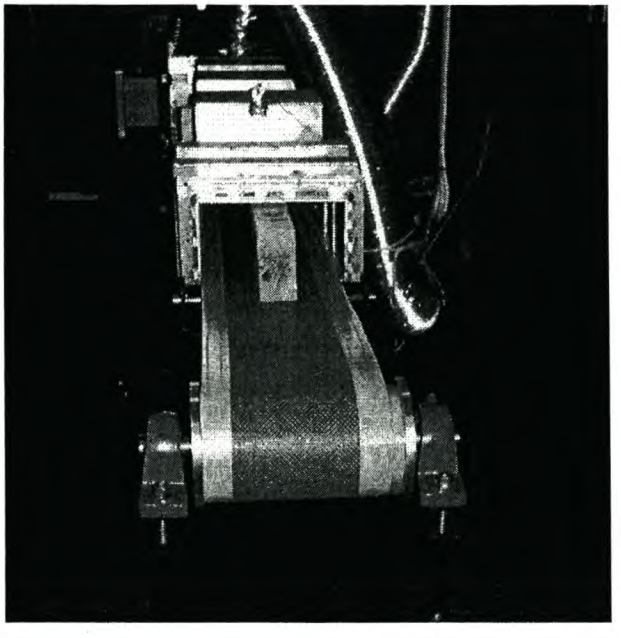

Figure 5.9 Wood entering the entrance choke

The conveyor belt carries the planks into the applicator at a speed of 5.4 mm/s. (Other speed settings are possible. The speed determines the amount of moisture lost in each pass for a particular drying schedule). As the wood passes through the applicator, it is heated by microwaves and centrifugal pump blown hot air. On leaving the exit choke, the wood is visual inspected (for charring, collapse and development of hot spots), weighed quickly, placed on the entrance choke again and the process is repeated.

After half the green mass has been lost, the schedule is changed. Hot air with a periodic supply

of microwaves is used. After 70 % of green mass has been lost, hot air alone is used. For each sample, the process is stopped when a number of consecutive passes do not lead to a change in mass.

The process described above demonstrated successfully the continuous microwave drying of wood and that average moisture content of wood can be measured after every pass. The major improvement which can be incorporated to the above system is to automate the measurement of moisture content as wood passes out of the exit choke. A set up similar to the one shown in Figure 5.10 can be used. Using Figure 5.10 as the basis, the principle of operation of the proposed system is discussed.

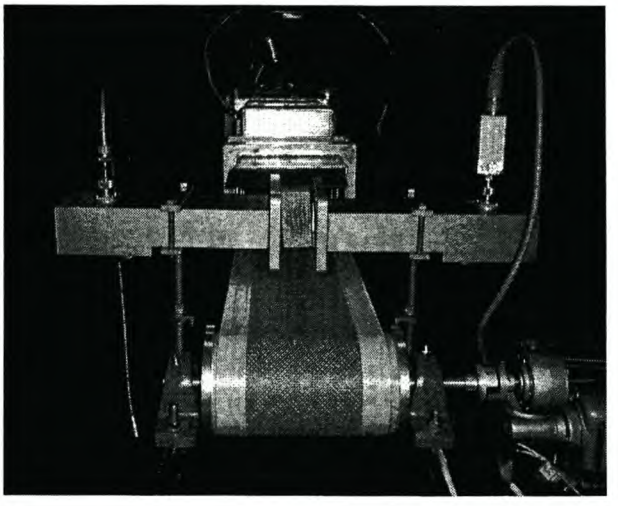

Figure 5.10 Wood coming out of exit choke and proposed position of moisture meter

The 'moisture measuring system' system in Figure 5.10 consists of a signal generator, waveguide sections, a power meter and a computer. The separation of the aligned waveguide sections is such that the plank just slides through the gap without touching the waveguide flanges. As the wood passes through the gap, the signal from the signal generator interacts with the wood. Some of the signal is scattered and the other finds its way into the receiving waveguide section where it is measured by the power meter. The problem with this simple arrangement is that there is no way of knowing the amount of detected power which has actually been transmitted through the wood.

The power detected during the passes of a particular sample can be plotted to give a graph like the one shown in Figure 5.11.

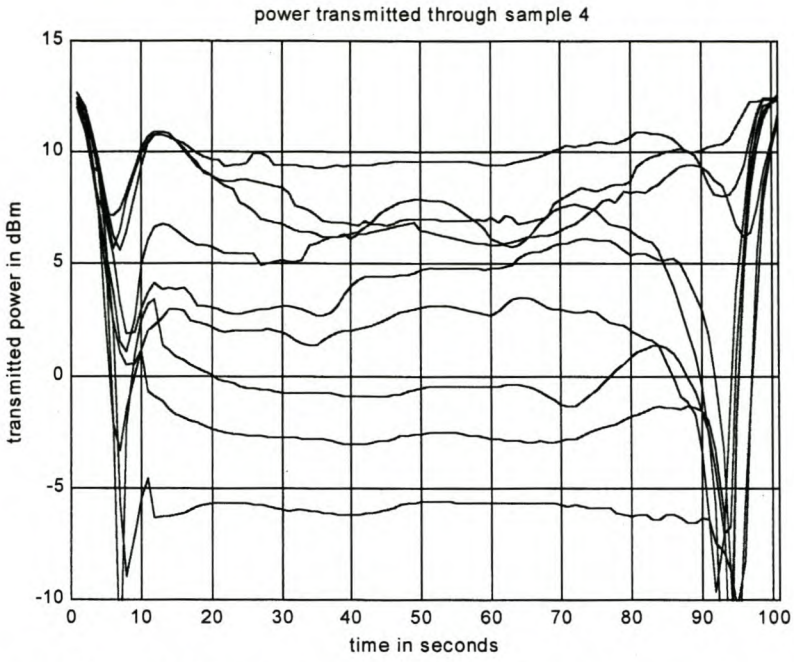

Figure 5.11 Multipass power transmitted through a sample.
(Passes increase from bottom to top)

Using the weaknesses and strengths of the system in Figure 5.10 as a guide, a moisture content measuring system that exploits the variation of permittivity with moisture content in wood is being proposed. The basic structure of the system is illustrated in Figure 5.12.

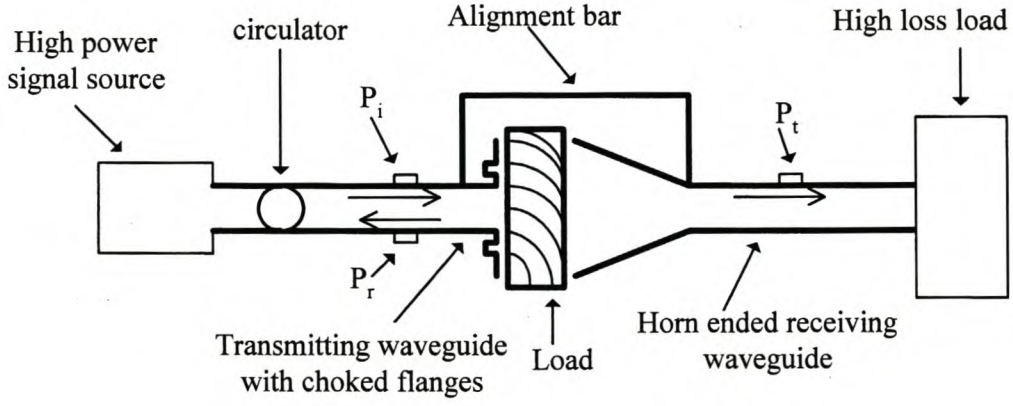

Figure 5.12 Components and measurement setup of the proposed moisture meter

The important features of the system are:

- the transmitting and receiving waveguides are kept in alignment by a rigid bar

- the transmitting waveguide has flanges which have chokes to reduce power loss.
- the receiving waveguide has a horn. This ensures that most of the power transmitted through the MUT is received and measured.
- the signal source is high power to ensure that a strong signal is available for interaction with the MUT. Load pulling is reduced by using circulators.
- the high loss load absorbs all the power delivered to it by the receiving waveguide.

The incident power P_i, the reflected power P_r and the transmitted power P_t would be measured accurately at intervals as the MUT is carried through the gap between the transmitting and receiving waveguides by a conveyor belt.

By letting $S_{11}^2 = \frac{P_r}{P_i}$ and $S_{21}^2 = \frac{P_t}{P_i}$ the real and the imaginary parts of permittivity can be calculated using a NRW based routine. From the variation of the real part or the imaginary part with moisture content established by measurements on fixtures such as the stripline, an expression relating the dielectric properties can be formulated. The expression can then be used to relate the dielectric properties obtained from the proposed system to the moisture content.

The error due to the system can be found by measuring high and low loss materials of known permittivity (measured on waveguide or stripline fixture). The error is the difference between values obtained through the system and those obtained through well tested fixtures. The error can then be used to correct for the dielectric properties measured by the system.

Such a system should appeal to a kiln operator especially if the moisture content determination is done in real time.

5.6 Conclusion.

In this chapter, dielectric heating has been reviewed, dielectric properties of wood at different moisture content have been measured using a stripline fixture and continuous microwave-air processing of wood has been demonstrated.

The dielectric properties were used to simulate the distribution of absorbed microwave energy during microwave drying of wood. This was validated by fax-paper mapping.

During the continuous processing, the wood was visually inspected and its moisture content determined after every run. The drying wood did not develop hot spots, even if it had knots. Any length of wood which can enter and exit the chokes easily can be processed using the mock-up industrial facility. Available options for controlling the drying rate include choosing the speed of the conveyor belt and the combination of microwaves with conventional heating.

Any online moisture measuring system was investigated and was found to be unsatisfactory. However, it was used as a guide in the proposal presented in this chapter for an online moisture meter.

Chapter 6

General Conclusions and Recommendations for Future Research

This dissertation combined a wide range of topics to address a wide spectrum of issues in dielectric heating of wood.

In Chapter 2, four fixtures have been used to measure the dielectric properties of teflon and perspex. The coaxial probe is an innovative modification of a panel mount SMA female connector. The calibration kit for the probe is new. The design of a new stripline fixture and its calibration kit has been presented. Algorithms for extracting dielectric properties from measured data have been developed from existing ones. For application to the stripline fixture, the algorithm presented by Boughriet et al.[36] needed substantial modification. The uncertainty analysis of stripline measured dielectric properties is much more rigorous than usually found in the literature. A rigorous methodology for calibrating a waveguide fixture has been presented.

The design of microwave applicators is often regarded as a daunting task, considered an art rather than a science. This is because the design procedure is not often clear. Chapter 3 gives a systematic procedure for designing a slotted waveguide feed. The feed is treated as an antenna and is characterised as such.

Two feeds are used in the microwave applicator reported in Chapter 4. The applicator has several operational modes which include the use of open-ended chokes and a conveyor belt. The applicator and choke are characterised under low and high power excitation using a practical procedure which avoids de-embedding. The procedure has not been reported before.

The performance of the microwave heating system in each operational mode is investigated in Chapter 5. The findings are summarised as drying curves which indicate the cost in terms of time for each mode. The drying profile of wood is followed by simulation and experiment. This is the first time that wood dielectric properties have been measured using a stripline fixture and then used to simulate the drying process using a FEM. The chapter concludes with a demonstration of an industrial continuous wood drying process in which the moisture content of the wood is periodically measured using a gravimetric method. Dielectric heating of wood, on a conveyor belt, as it passes through a slotted waveguide fed applicator with a choke, has not been reported in the literature. An online moisture measuring system is proposed and its operation is discussed.

Further studies in this area can focus on

- implementation of the proposed moisture measuring system or its variant. This can provide the long sought after online moisture content measuring system for the wood industry.
- modelling the relationship between the real and the imaginary parts of permittivity. A practical implementation of the Kramers-Kronig relations which relate the two need further investigation. This is important because, as shown in Chapter 2, most fixture

measurements result in one component of permittivity being more accurately determined than the other. The modelling will enable the less accurately determined component to be obtained from the more accurately determined one.

Appendix 2.A

Capacitance of Plate Capacitor due to Fringing Field [44]

The disc plate capacitor of the Marconi dielectric test jig has a fringing capacitance error. The error to be included when processing data measured at a particular separation of plates is obtained from Figure 2A.1

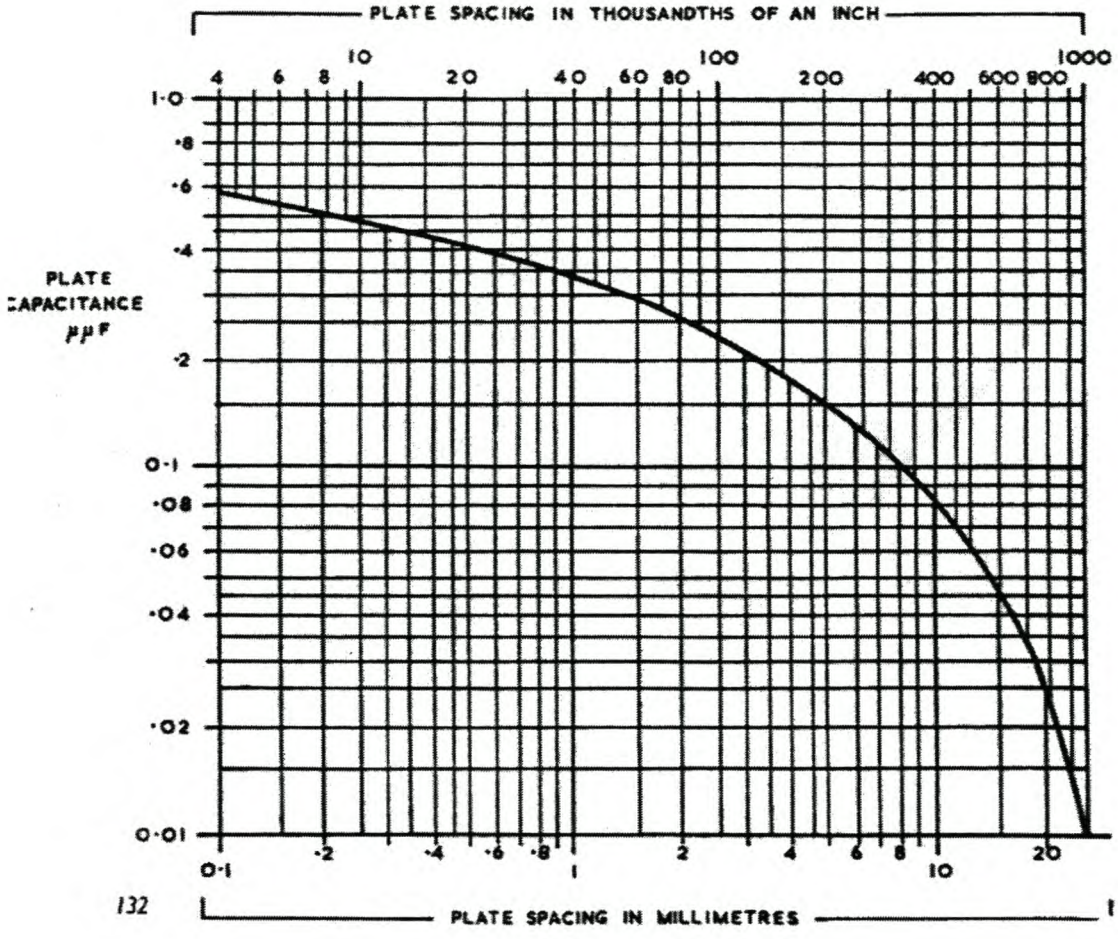

Figure 2A.1 Variation of fringing capacitance with separation of plates for the Marconi dielectric test jig.

Appendix 2B

MATLAB Routine for Calculating the Real and Imaginary Part of Permittivity from Probe Measurements

This program implements equations (2.13), (2.15), (2.16) and (2.17).

```
f = linspace(0.045, 3, 101)';        % frequency in GHz

% Determination of fringing capacitance, equation (2.13)

im=imag(s11);                        % imaginary part
re = real(s11);                      % real part
 x = atan(im./re);
 p = tan(x/2);                       % phase angle
z = 50;                              %characteristic impedance
Co = p./(2*pi*f*z)                   %effective capacitance of probe


% Determination of the total capacitance, equation (2.17)

a = (1.3e-3)/2;              % diameter of inner conductor in m
b = (4.1e-3)/2;              % diameter of outer conductor in m
c = 2.9979e8;                %speed of light in a vacuum in m
Z = 50;                      % impendance in ohms

m=(2*sqrt(a*b)/(b+a));
[K,E]=ellipke(m);
Ct=(4*(a+b)*(E-1)/(Z*pi*c*log(a/b)));   % capacitance of probe without sample.

% Calculation of permittivity, equations (2.15) and (2.16)
Cf = Ct-Co;
y = Cf.\Co;

r = abs(s11);
p = angle(s11);

%%%%%%%%%%%%%%%%%%%%%%%%%%%%%%%%%%%%%%%%%%%%%%%%%%%%%%%%

den1 = pi*f*Z.*Co;

num = r.*sin(-p);
den2 = (1+2*r.*cos(p)+r.^2);
```

```
den = den1.*den2;
x = num./den;
e1 = x-y;                % real part

e11=(1-r.^2)./den;       % imaginary part

%%%%%%%%%%%%%%%%%%%%%%%%%%%%

subplot(2,1,1)
plot(f,e1)
title(' ')
xlabel('freg in GHz')
ylabel('real part of permittivity')
axis([1 3 0 3])
grid
hold on

subplot(2,1,2)
plot(f, e11)
xlabel('freg in GHz')
ylabel('loss factor')
axis([1 3 -0.5 1])
grid
```

Appendix 2C

Alternative Expression for the n Parameter in the Phase Ambiguity Correction Term of the Nicolson-Ross-Weir (NRW) algorithm

Equation (2.24) has a phase ambiguity which must be corrected for at certain frequencies when processing measured data using the NRW algorithm. The correction term is $2\pi nj$. Methods for determining n have been discussed in the literature. An expression for n used in this study is derived in this appendix.

Smith [38] gave n as

$$n = \frac{j}{2\pi}\left[\frac{\omega}{\mathrm{T}}\frac{\partial \mathrm{T}}{\partial \omega} - \ln(T)\right] \tag{2C.1}$$

and T as

$$\mathrm{T} = e^{-j\gamma_0 d}$$

where $\gamma_o = \alpha + j\beta$

For the no attenuation case $\alpha = 0$ therefore $\gamma_o = j\beta$.

Thus $$\mathrm{T} = e^{-j(j\beta)d}$$

$$= e^{\beta d} \tag{2C.2}$$

but $$\beta = \frac{2\pi}{\lambda}$$

$$= \frac{2\pi f}{c}$$

$$= \frac{2\pi f}{30} \tag{2C.3}$$

where the frequency f is in Hertz and the velocity of light in a vacuum c has been taken to be equal to 3×10^8 ms^{-1}.

Substituting the value of β in (2B.3) into (2B.2) gives

$$\mathrm{T} = e^{\frac{\pi f d}{15}} \tag{2C.4}$$

Therefore $$\frac{\partial T}{\partial f} = \frac{\pi d T}{15} \tag{2C.5}$$

Next the term , $\frac{\omega}{T}\frac{\partial T}{\partial \omega}$, in equation (2B.1) is expressed as

$$\frac{\omega}{T}\frac{\partial T}{\partial \omega} = \frac{2\pi f}{T}\frac{\partial T}{2\pi \partial f}$$

$$= \frac{f}{T}\frac{\partial T}{\partial f} \qquad (2C.6)$$

Substituting the value of $\frac{\partial T}{\partial f}$ in (2B.5) into (2B.6) and simplifying gives

$$\frac{\omega}{T}\frac{\partial T}{\partial \omega} = \frac{\pi f d}{15} \qquad (2C.7)$$

Substituting for $\frac{\omega}{T}\frac{\partial T}{\partial \omega}$ from (2B.7) into (2B.1) gives

$$n = \frac{j}{2\pi}\left(\frac{\pi f d}{15} - \ln(T)\right)$$

Appendix 2D

MATLAB Program for Calculating Permittivity from Stripline Measurements

This program implements equations (2.21) through (2.26)

```
% measured data, the matrix which contains the measured data is a

for n = 1:22
s11 = a(n,2)+a(n,3)*j;
s21 = a(n,4)+a(n,5)*j;
 f(n) = a(n,1);

 % Equations (2.21) and (2.22)

k = ((s11^2-s21^2)+1)/(2*s11);
r1 = k+(k^2-1)^0.5;
r2 = k-(k^2-1)^0.5;

 if abs(r1)<=1      % condition as given in the algorithm
    r = r1;
else
    r=r2;
  end

 %%% Equations (2.23) and (2.24)

t = ((s11+s21)-r)/(1-(s11+s21)*r);
v = log(1/t);
d = 3;              % length of sample in cm
y = -(v/(2*pi*d))^2;
b = y^0.5;
if real(b)>=0
    b = real(b)-imag(b);
else
     b = -real(b)+imag(b);
  end

%%% Equations (2.25) and (2.26)
p = (1+r)/(1-r);
xo = 30/f(n);       % wavelength in free space in cm at the
x g= xo;
ue = xg*b*p;
e(n,:) = xg*b/p;
```

```
  end

  for n = 21:50
  s11 = a(n,2)+a(n,3)*j;
  s21 = a(n,4)+a(n,5)*j;
   f(n) = a(n,1);

%%%
```

Appendix 2E.

Stripline Uncertainty Analysis

Associated with any practical measurement is uncertainty. The main categories of errors are:

- systematic
- random or non-systematic
- drift

Random errors cannot be characterised but are reduced by averaging. Drift errors depend on the variations of the ambient conditions with time. They can be reduced by recalibration, usually at the beginning of each measurement session. Systematic errors can be reduced by calibration. However, some errors cannot be removed. These can be analysed by differentiating partially the expressions which relate the quantity whose uncertainty is to be found to the quantity which causes the uncertainty. The uncertainty in the quantity which causes the uncertainty must be measurable. Uncertainties due to factors other than measurable ones are not considered in this analysis.

From error analysis theory, it is well known that errors are additive [45]. Therefore the uncertainty in $\varepsilon^* = \varepsilon' - j\varepsilon''$ can be written as $\Delta\varepsilon^* = \Delta\varepsilon' + j\Delta\varepsilon''$.

where $\Delta\varepsilon^*$ is the uncertainty in ε^*
$\Delta\varepsilon'$ is the uncertainty in ε'
$\Delta\varepsilon''$ is the uncertainty in ε''

Let $$\Delta\varepsilon' = \Delta\varepsilon'_{11} + \Delta\varepsilon'_{21}$$

$$\Delta\varepsilon'' = \Delta\varepsilon''_{11} + \Delta\varepsilon''_{21}$$

where $\Delta\varepsilon'_{11}$ is the uncertainty in ε' due to the magnitude and phase measurement at port 1
$\Delta\varepsilon'_{21}$ is the uncertainty in ε' due to the magnitude and phase measurements at port 2
$\Delta\varepsilon''_{11}$ and $\Delta\varepsilon''_{21}$ are defined similarly.

Following a procedure used to analyse the uncertainty of a two port transmission line measurement system first by Barker-Jarvis et al. [46] and later by Boughriet et al.[36], the following expressions for $\Delta\varepsilon'_{11}, \Delta\varepsilon'_{21}, \Delta\varepsilon''_{11}$ and $\Delta\varepsilon''_{21}$ can be written:

$$\Delta\varepsilon'_{11} = \sqrt{\left(\frac{\partial\varepsilon'}{\partial|S_{11}|}\Delta|S_{11}|\right)^2 + \left(\frac{\partial\varepsilon'}{\partial\theta_{11}}\Delta\theta_{11}\right)^2 + \left(\frac{\partial\varepsilon'}{\partial d}\Delta d\right)^2} \qquad \text{(2E1)}$$

$$\Delta\varepsilon'_{21} = \sqrt{\left(\frac{\partial\varepsilon'}{\partial|S_{21}|}\Delta|S_{21}|\right)^2 + \left(\frac{\partial\varepsilon'}{\partial\theta_{21}}\Delta\theta_{21}\right)^2 + \left(\frac{\partial\varepsilon'}{\partial d}\Delta d\right)^2} \tag{2E2}$$

$$\Delta\varepsilon''_{11} = \sqrt{\left(\frac{\partial\varepsilon''}{\partial|S_{11}|}\Delta|S_{11}|\right)^2 + \left(\frac{\partial\varepsilon''}{\partial\theta_{11}}\Delta\theta_{11}\right)^2 + \left(\frac{\partial\varepsilon''}{\partial d}\Delta d\right)^2} \tag{2E3}$$

$$\Delta\varepsilon''_{21} = \sqrt{\left(\frac{\partial\varepsilon''}{\partial|S_{21}|}\Delta|S_{21}|\right)^2 + \left(\frac{\partial\varepsilon''}{\partial\theta_{21}}\Delta\theta_{21}\right)^2 + \left(\frac{\partial\varepsilon''}{\partial d}\Delta d\right)^2} \tag{2E4}$$

where

$$\frac{\partial\varepsilon'}{\partial|S_{11}|} = \left(\frac{\partial\varepsilon'}{\partial\Gamma}\frac{\partial\Gamma}{\partial S_{11}} + \frac{\partial\varepsilon'}{\partial T}\frac{\partial T}{\partial S_{11}}\right)\exp^{j\theta_{11}} \tag{2E5}$$

$$\frac{\partial\varepsilon'}{\partial|S_{21}|} = \left(\frac{\partial\varepsilon'}{\partial\Gamma}\frac{\partial\Gamma}{\partial S_{21}} + \frac{\partial\varepsilon'}{\partial T}\frac{\partial T}{\partial S_{21}}\right)\exp^{j\theta_{21}} \tag{2E6}$$

$$\frac{\partial\varepsilon'}{\partial\theta_{11}} = j|S_{11}|\frac{\partial\varepsilon'}{\partial|S_{11}|} \tag{2E7}$$

$$\frac{\partial\varepsilon'}{\partial\theta_{21}} = j|S_{21}|\frac{\partial\varepsilon'}{\partial|S_{21}|} \tag{2E8}$$

$$\frac{\partial\varepsilon'}{\partial d} = \frac{\partial\varepsilon'}{\partial T}\frac{\partial T}{\partial d} \tag{2E9}$$

$$\frac{\partial\varepsilon''}{\partial|S_{11}|} = \left(\frac{\partial\varepsilon''}{\partial\Gamma}\frac{\partial\Gamma}{\partial S_{11}} + \frac{\partial\varepsilon''}{\partial T}\frac{\partial T}{\partial S_{11}}\right)\exp^{j\theta_{11}} \tag{2E10}$$

$$\frac{\partial\varepsilon''}{\partial|S_{21}|} = \left(\frac{\partial\varepsilon''}{\partial\Gamma}\frac{\partial\Gamma}{\partial S_{21}} + \frac{\partial\varepsilon''}{\partial T}\frac{\partial T}{\partial S_{21}}\right)\exp^{j\theta_{21}} \tag{2E11}$$

$$\frac{\partial\varepsilon''}{\partial\theta_{11}} = j|S_{11}|\frac{\partial\varepsilon''}{\partial|S_{11}|} \tag{2E12}$$

$$\frac{\partial\varepsilon''}{\partial\theta_{21}} = j|S_{21}|\frac{\partial\varepsilon''}{\partial|S_{21}|} \tag{2E13}$$

$$\frac{\partial \varepsilon''}{\partial d} = \frac{\partial \varepsilon''}{\partial \mathrm{T}} \frac{\partial \mathrm{T}}{\partial d} \qquad (2E14)$$

in which

$$\frac{\partial \Gamma}{\partial S_{11}} = \left(1 \pm \frac{K}{\sqrt{K^2 - 1}}\right)\left(\frac{2S_{11}^2 - 2S_{21}^2 + 1}{2S_{11}^2}\right) \qquad (2E15)$$

$$\frac{\partial \Gamma}{\partial S_{21}} = \left(1 \pm \frac{K}{\sqrt{K^2 - 1}}\right)\left(\frac{-2S_{21}}{S_{11}}\right) \qquad (2E16)$$

$$\frac{\partial \mathrm{T}}{\partial S_{11}} = \frac{1 - \Gamma^2 + \frac{\partial \Gamma}{\partial S_{11}}\left[\left(S_{11} + S_{21}\right)^2 - 1\right]}{\left[1 - \left(S_{11} + S_{21}\right)\Gamma\right]^2} \qquad (2E17)$$

$$\frac{\partial \mathrm{T}}{\partial S_{21}} = \frac{1 - \Gamma^2 + \frac{\partial \Gamma}{\partial S_{21}}\left[\left(S_{11} + S_{21}\right)^2 - 1\right]}{\left[1 - \left(S_{11} + S_{21}\right)\Gamma\right]^2} \qquad (2E18)$$

In the above equations, the uncertainties in the S-parameters and phase angles are obtained from the specifications of the ANA. However, the differentials with respect to Γ and T are not explicitly given as functions of measured quantities. The following analysis shows the relationship.

A more general equation for ε^* is [36]

$$\varepsilon^* = \left(\frac{1 - \Gamma}{1 + \Gamma}\right)^{(n-1)}\left(\frac{\lambda_{og}}{\Lambda}\right)^{(n+1)} \qquad (2E19)$$

Differentiating equation (2E19) with respect to Γ gives

$$\frac{\partial \varepsilon^*}{\partial \Gamma} = (1 - n)\left[\frac{j\lambda_{og}}{2\pi d}\ln(\mathrm{T})\right]^{(n+1)}\left[\frac{1 - \Gamma}{1 + \Gamma}\right]^{-n} \qquad (2E20)$$

Substituting $\varepsilon^* = \varepsilon' - j\varepsilon''$ into equation (2E20) yields

$$\frac{\partial \varepsilon'}{\partial \Gamma} - j\frac{\partial \varepsilon'}{\partial \Gamma} = (1-n)\left[\frac{j\lambda_{og}}{2\pi d}\ln(T)\right]^{(n+1)}\left[\frac{1-\Gamma}{1+\Gamma}\right]^{-n} \tag{2E21}$$

When $n = 0$, equation (2E21) becomes

$$\frac{\partial \varepsilon'}{\partial \Gamma} - j\frac{\partial \varepsilon'}{\partial \Gamma} = \frac{j\lambda_{og}}{2\pi d}\ln(T) \tag{2E22}$$

This implies that

$$\frac{\partial \varepsilon'}{\partial \Gamma} = 0 \tag{2E23}$$

$$\frac{\partial \varepsilon''}{\partial \Gamma} = -\frac{\lambda_{og}}{2\pi d}\ln(T) \tag{2E24}$$

Differentiating equation (2E19) with respect to T gives

$$\frac{\partial \varepsilon^*}{\partial T} = (1+n)\left[\frac{j\lambda_{og}}{2\pi d}\ln(T)\right]^{n}\left[\frac{1-\Gamma}{1+\Gamma}\right]^{(1-n)}\left[\frac{j\lambda_{og}}{2\pi d T}\right] \tag{2E25}$$

Substituting $\varepsilon^* = \varepsilon' - j\varepsilon''$ into equation (2E25) yields

$$\frac{\partial \varepsilon'}{\partial T} - j\frac{\partial \varepsilon''}{\partial T} = (1+n)\left[\frac{j\lambda_{og}}{2\pi d}\ln(T)\right]^{n}\left[\frac{1-\Gamma}{1+\Gamma}\right]^{(1-n)}\left[\frac{j\lambda_{og}}{2\pi d T}\right] \tag{2E26}$$

When $n = 0$ equation (2E26) becomes

$$\frac{\partial \varepsilon'}{\partial T} - j\frac{\partial \varepsilon''}{\partial T} = \left[\frac{1-\Gamma}{1+\Gamma}\right]\left[\frac{j\lambda_{og}}{2\pi d T}\right] \tag{2E27}$$

Equating real and imaginary parts gives

$$\frac{\partial \varepsilon'}{\partial T} = 0 \tag{2E28}$$

$$\frac{\partial \varepsilon''}{\partial T} = -\left[\frac{1-\Gamma}{1+\Gamma}\right]\left[\frac{j\lambda_{og}}{2\pi d T}\right] \tag{2E29}$$

A MATLAB routine for evaluating the errors is presented in appendix 2E.1 and typical results are given in figure 2.14.

Appendix 2E.1

MATLAB program for uncertainty analysis of data measured using the stripline fixture

To facilitate the writing of the uncertainty analysis program for the stripline fixture in MATLAB, the following assignments were made in the equations of Appendix 2E

$$a_1 = \frac{\partial \varepsilon'}{\partial \Gamma} \qquad a_2 = \frac{\partial \varepsilon''}{\partial \Gamma} \qquad b_1 = \frac{\partial \varepsilon'}{\partial T}$$

$$b_2 = \frac{\partial \varepsilon''}{\partial T} \qquad e_1 = \frac{\partial \Gamma}{\partial S_{11}} \qquad e_2 = \frac{\partial \Gamma}{\partial S_{21}}$$

$$g_1 = \frac{\partial T}{\partial S_{11}} \qquad g_2 = \frac{\partial T}{\partial S_{21}} \qquad h_1 = \frac{\partial \varepsilon'}{\partial |S_{11}|}$$

$$h_2 = \frac{\partial \varepsilon'}{\partial |S_{21}|} \qquad L_1 = \frac{\partial \varepsilon'}{\partial \theta_{11}} \qquad L_2 = \frac{\partial \varepsilon'}{\partial \theta_{21}}$$

$$m_1 = \frac{\partial \varepsilon'}{\partial d} \qquad m_2 = \frac{\partial \varepsilon''}{\partial d} \qquad v_1 = \frac{\partial \varepsilon''}{\partial |S_{11}|}$$

$$v_2 = \frac{\partial \varepsilon''}{\partial |S_{21}|} \qquad w_1 = \frac{\partial \varepsilon''}{\partial \theta_{11}} \qquad w_2 = \frac{\partial \varepsilon''}{\partial \theta_{21}}$$

$$y_1 = \Delta|S_{11}| \qquad y_2 = \Delta|S_{21}| \qquad y_3 = \Delta|\theta_{11}|$$

$$y_4 = \Delta|\theta_{21}| \qquad y_5 = \Delta d \qquad z_1 = \Delta\varepsilon'_{11}$$

$$z_2 = \Delta\varepsilon'_{21} \qquad z_3 = \Delta\varepsilon''_{11} \qquad z_4 = \Delta\varepsilon''_{21}$$

$$z_5 = \Delta\varepsilon' \qquad z_6 = \Delta\varepsilon'' \qquad r = \Gamma$$

$$x = \lambda_{og}$$

```
for n = 1:50
    s11 = a(n,2)+a(n,3)*j;
    s21 = a(n,4)+a(n,5)*j;
    f(n) = a(n,1);
    o11 = a(n,6);
    o21 = a(n,7);
     x = 30/f(n);
     d = 3;
%%%
```

```
        w1 = j*abs(s11)*v1;
        w2 = j*abs(s21)*v2;
          m2 = b1*p;

%%%
```

Appendix 2 F

NRW Algorithm for Calculating Permittivity from Waveguide Measurements

This routine implements the well known NRW algorithm [34] for processing waveguide measured data.

```
%%%
```

Appendix 3A

Sine and Cosine Integral Functions

These functions are a MATLAB adaptation of the FORTRAN functions written by A.C. Polycarpou and distributed on disk with "Antenna Theory : Analysis and Design", 2nd ed. , New York, Wiley, 1997 . C.A Balanis. The FORTRAN code for ci( ) and si( ) functions needed substantial modification.

ci.m

```
% This function calculates the cosine integral
function ci = ci(u)
        ci = f(u)*sin(u)-g(u)*cos(u);
```

si.m

```
% This function calculates the sine integral
function si = si(u)
        si = 2.0*atan(1)-f(u)*cos(u)-g(u)*sin(u);
```

f.m

```
% This function is used by ci( ) and si( )
function f = f(x)
         a = [38.027264 265.187033 335.677320 38.102495];
         b = [40.021433 322.624911 570.236280 157.105423];

        numer = (x^8+a(1)*x^6+a(2)*x^4+a(3)*x^2+a(4));
        denom = (x^8+b(1)*x^6+b(2)*x^4+b(3)*x^2+b(4));

        f = (1./x).*(numer/denom);
```

g.m

```
% This function is used by ci( ) and si( )
function g = g(x)
         a = [42.242855 302.757865 352.018498 21.821899];
         b = [48.196927 482.485984 1114.978885 449.690326];

        numer = (x^8+a(1)*x^6+a(2)*x^4+a(3)*x^2+a(4));
        denom = (x^8+b(1)*x^6+b(2)*x^4+b(3)*x^2+b(4));

        g = (1./x^2).*(numer./denom);
```

Appendix 3B

Design of a Slotted Waveguide Feed which Includes Mutual Coupling

This program is for designing a slotted waveguide for a microwave applicator. The mutual coupling between four slots is included.

```
n = 1:4;          % number of slots
%Relative excitation levels
a1 = 1;
a2 = 2;
a3 = 2;
a4 = 1;

%value of constant k

K= 1/(a1^2+a2^2+a3^2+a4^2);
%calculation of the normalised conductance of the nth slot
g1 = K*a1^2;
g2 = K*a2^2;
g3 = K*a3^2;
g4 = K*a4^2;

%dimensions of the waveguide in inches
a = 0.9;
b = 0.4;
f = 9.375*10^9;          % frequency of signal
c = 3*10^10/2.54; %speed of light in avacuum
lamdao = c/f;
lamdag = lamdao/((1-(lamdao/(2*a))^2)^0.5);  % this assumes a TE10 mode

%calculation of the offsets
x1 = abs((a/pi)*asin((g1*lamdao*b/(2.09*lamdag*a*(cos(pi*lamdao/(2*lamdag)))^2)))^0.5);
x2 = abs((a/pi)*asin((g2*lamdao*b/(2.09*lamdag*a*(cos(pi*lamdao/(2*lamdag)))^2)))^0.5);
x3 = abs((a/pi)*asin((g3*lamdao*b/(2.09*lamdag*a*(cos(pi*lamdao/(2*lamdag)))^2)))^0.5);
x4 = abs((a/pi)*asin((g4*lamdao*b/(2.09*lamdag*a*(cos(pi*lamdao/(2*lamdag)))^2)))^0.5);

%calculation of the length of the slots
k = 2*pi/lamdao;
beta = 2*pi/lamdag;
zo = ((pi*b)/(2*a))*((120*pi)/((1-(lamdao/(2*a))^2)^0.5));

% Calculation of the length Ln
xn  = x1;  % Put the appropriates value before a run
```

```
gn  = g1;
an  = a1;
P = (lamdao/a)*sin(pi*xn/a)*sqrt((2*zo)/(120*pi*k^2*a*b))*an/6;
Ln1 = (1/beta)*acos(gn/P);
% for a starting length we use the center line resonance condition

L=Ln1;

%Mutual coupling of two parallel in achelon DIPOLES
%ref Antenna Theory Analysis and Design by Balanis
%integration arguments
d = x1+x2;
h = 2*Ln1;
s = h;
w0 = beta*(h);
w1 = beta*((d^2+(h)^2)^0.5+h);
w2 = beta*((d^2+(h)^2)^0.5-h);
w3 = beta*((d^2+(h-L)^2)^0.5+(h-L));
w4 = beta*((d^2+(h-L)^2)^0.5-(h-L));
w5 = beta*((d^2+(h+L)^2)^0.5+(h+L));
w6 = beta*((d^2+(h+L)^2)^0.5-(h+L));

%Calcualtion of the mutual resistance between 1&2
Q = 1/((sin(beta*h))^2);
r1 = -15*Q*cos(w0)*(-2*ci(w1)-2*ci(w2)+ci(w3)+ci(w4)+ci(w5)+ci(w6));
r2 = 15*Q*sin(w0)*(2*si(w1)-2*si(w2)-si(w3)+si(w4)-si(w5)+si(w6));
r12 = r1+r2

%calculation of mutual reactance between 1&2
x2a = -15*Q*cos(w0)*(2*si(w1)+2*si(w2)-si(w3)-si(w4)-si(w5)-si(w6));
x2b = 15*Q*sin(w0)*(2*ci(w1)-2*ci(w2)-ci(w3)+ci(w4)-ci(w5)+ci(w6));
x12 = x2a+x2b;
z12 = r12+j*x12;

%MUTUAL COUPLING OF TWO DIPOLES IN COLLINEAR CONFIG 1&3
v0 = beta*(h+s);
v1 = beta*(2*h+s);
v2 = beta*s;
v3 = beta*(h+s);
r13 = -15*Q*cos(v0)*(-2*ci(2*v0)+ci(v2)+ci(v1)-log(v3))+0.5*Q*sin(v0)*(2*si(2*v0)-si(v2)-
si(v1));
x13  =  -15*Q*cos(v0)*(2*si(2*v0)-si(v2)-si(v1))+0.5*Q*sin(v0)*(2*ci(2*v0)-ci(v2)-si(v1)-
log(v3));
z13 = r13+j*x13;

%Calculation of the coupling between 1&4
```

```
y0 = beta*(2*h+2*s);
y1 = beta*((d^2+(2*h+2*s)^2)^0.5);
y2 = beta*((d^2+(1.5*h+2*s)^2)^0.5);
y3 = beta*((d^2+(h+2*s)^0.5));
y4 = beta*((d^2+(3*h+2*s)^2)^0.5);
y5 = beta*((d^2+(2.5*h+2*s)^2)^0.5);
y6 = beta*((d^2+(2*h+2*s)^0.5));

%calculation of mutual reisitance between 1&4
r4a = -15*Q*cos(y0)*(-2*ci(y1)-2*ci(y2)+ci(y3)+ci(y4)+ci(y5)+ci(y6));
r4b = 15*Q*sin(y0)*(2*si(y1)-2*si(y2)-si(y3)+si(y4)-si(y5)+si(y6));
r14 = r4a+r4b;

%calculation of mutual reactance between 1&4
x4a = -15*Q*cos(y0)*(2*si(y1)+2*si(y2)-si(y3)-si(y4)-si(y5)-si(y6));
x4b = 15*Q*sin(y0)*(2*ci(y1)-2*ci(y2)-ci(y3)+ci(y4)-ci(y5)+ci(y6));
x14=x4a+x4b;
z14=r14+j*x14;

%Total mutual coupling term for dipole 1
z1m=z12+z13+z14+z23;

%conductance g1
gm1=1/(real(z1m));
%calculation of xm2, the m stands for mutual
xm1=abs((a/pi)*asin((gm1*lamdao*b/(2.09*lamdag*a*(cos(pi*lamdao/(2*lamdag)))^2)))^0.5);

%calculation of Lm
Lm1=(1.517+1.822*xm1)/k;
```

APPENDIX 3C

Simulated Loss at Different Offsets for Four, Six and Ten Slots

Table 3A1 Offset - loss table for four slots

offset of slots 1 and 3 in mm	offset of slots 2 and 4 in mm	S_{11} in dB
0	0	0
10	-10	-6.942
14	-14	-10.994
14.5	-14.5	-11.014
14.7	-14.7	-11.49
14.8	-14.8	-16.191
14.9	-14.9	-15.595
15	-15	-15.125
15.1	-15.1	-14.014
15.2	-15.2	-11.478
15.3	-15.3	-11.387
15.5	-15.5	-11.395
16	-16	-11.305
20	-20	-8.066
25	-25	-4.953

Table 3A2 Offset - loss table for six slots

Offset of slots 1, 3 and 5 in mm	offset of slots 2, 4 and 6 in mm	S_{11} in dB
5	-5	-2.483
10	-10	-9.152
11.5	-11.5	-10.257
11.8	-11.8	-10.431
11.9	-11.9	–12.676
12	-12	-13.58
12.1	-12.1	-12.503
12.2	-12.2	-11.57
12.5	-12.5	-11.063
13	-13	-10.576
15	-15	-9.245
16	-16	-8.414
17.5	-17.5	-6.935
20	-20	-5.111
25	-25	-3.17

Table 3A3 Offset - loss table for ten slots

offset of slots 1, 3, 5, 7 and 9 in mm	offset of slots 2, 4, 6, 8 and 10 in mm	S_{11} in dB
5	-5	-3.303
7	-7	-6.502
9	-9	-9.575
10	-10	-12.770
11	-11	-9.33
12	-12	-8.542
13	-13	-7.531
14	-14	-6.479
15	-15	-5.753

Appendix 5A

Graphs of Permittivity of Wood Samples Measured on a Stripline Fixture

To investigate the interaction of microwaves with wood, its dielectric properties must be measured. The measurements are carried out on samples whose location and orientation take into account the anisotropy of wood. The orientation of the samples under discussion is given in Figure 5.6. The dielectric properties of the samples were measured using a stripline fixture over six days.

Measurements carried out in the same session start with the same letter. The subscript of the letter identifies the sample. The first number of the subscript refers to the position on the plank and the second defines the orientation. For days A to C, the samples were air dried and for days D to F were oven dried. For easy comparison, the scales of the plots should be the same. However, using the same scales for the high and low moisture content samples yields invisible low value plots. In the interest of clarity, the scales are changed whenever necessary.

In order to facilitate the discussion of the measured results, this appendix is divided into two parts. Appendix 5.A.1 are results for sample 12. It is used so that the reader can follow the variation of properties easily. Appendix 5.A.2 contains results of all the measured samples.

The abbreviation MCDB (moisture content dry basis) is used in the titles of the graphs.

Appendix 5A.1 Variation of permittivity of sample 12 with frequency at different moisture contents

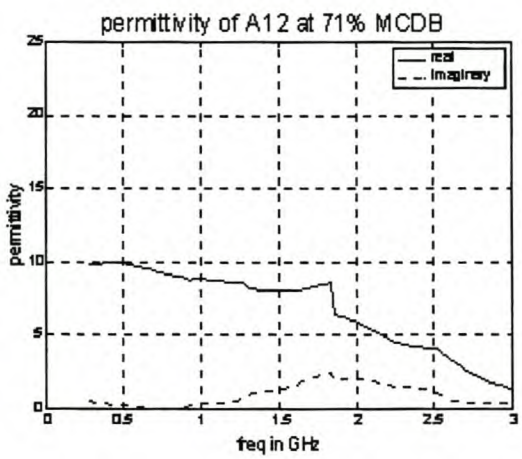

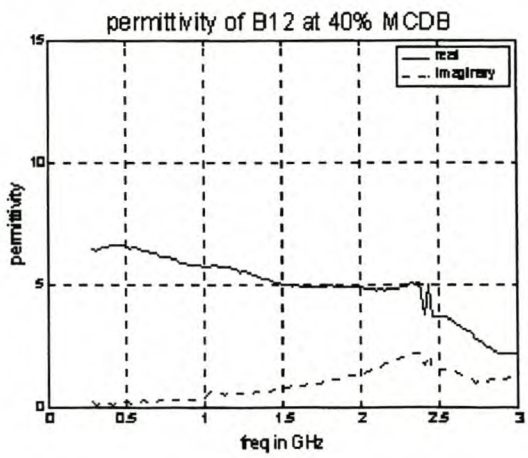

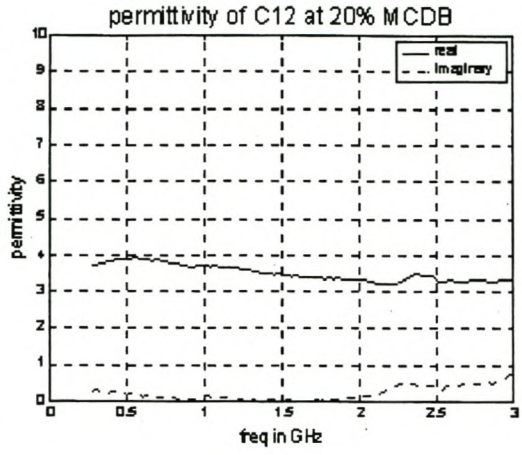

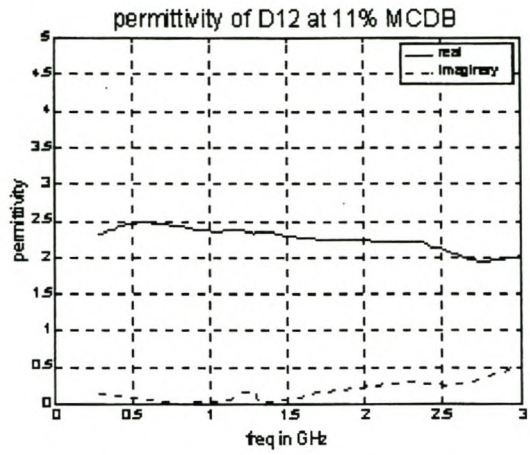

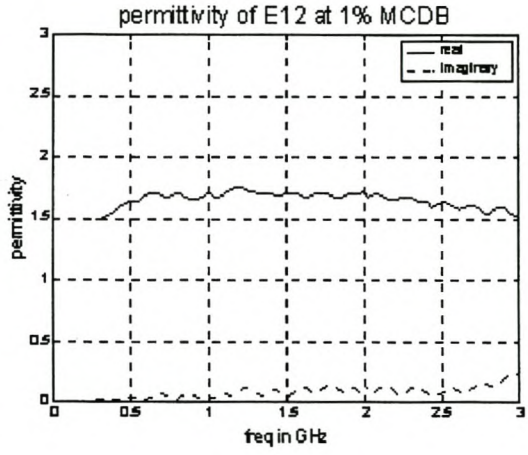

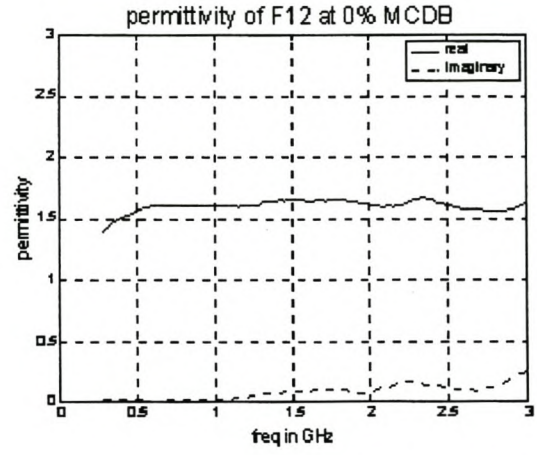

Appendix 5A.1.1

Graph of Permittivity Against Moisture Content for Sample 12

To show clearly the variation of permittivity with moisture content, values of permittivity at 2.5 Ghz, for samples 12, were obtained from Appendix 5.A.1. The permittivity is plotted against moisture content in this appendix.

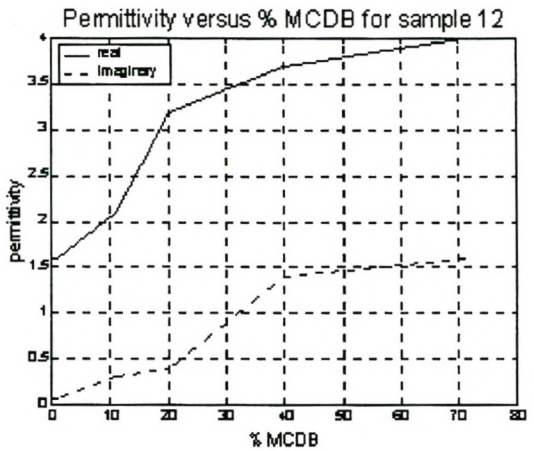

Appendix 5A.2 Variation of Permittivity of Samples with Frequency at Different Moisture Contents

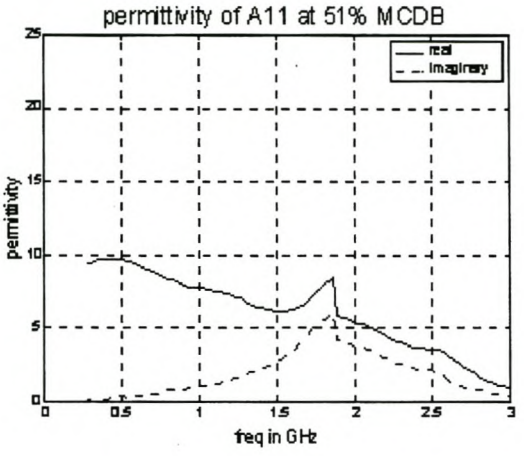

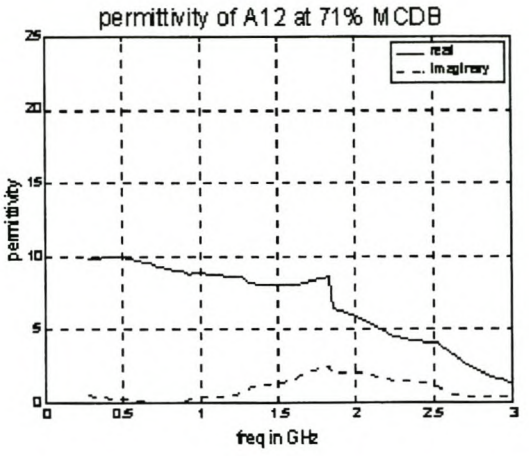

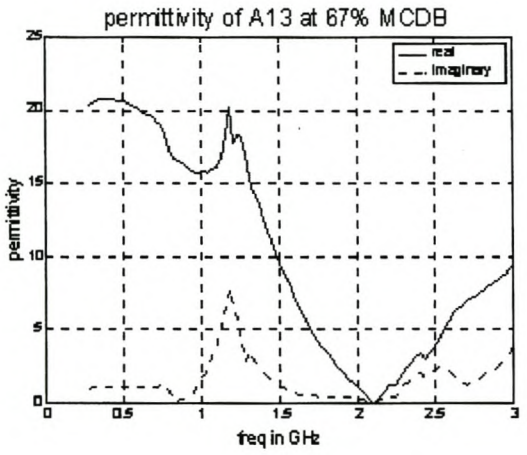

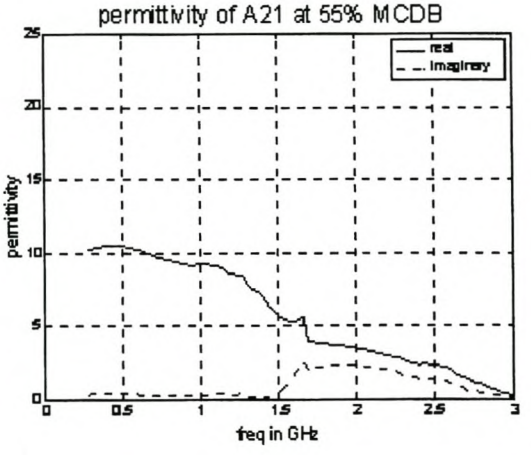

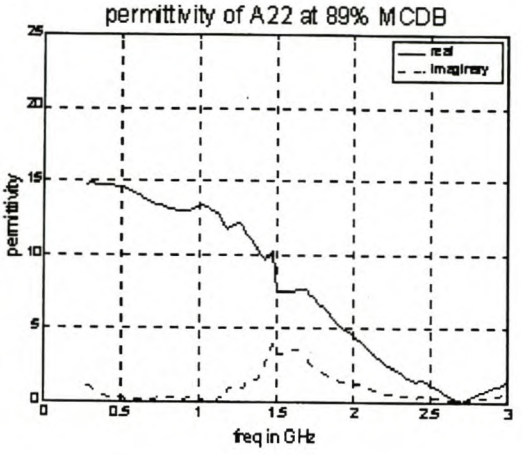

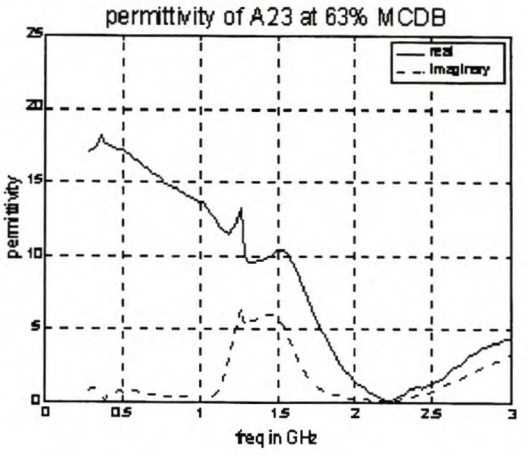

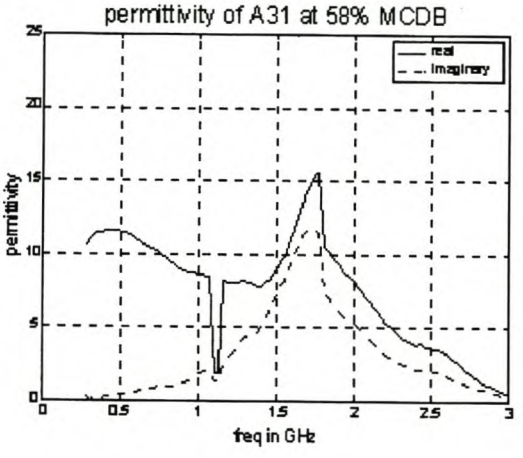

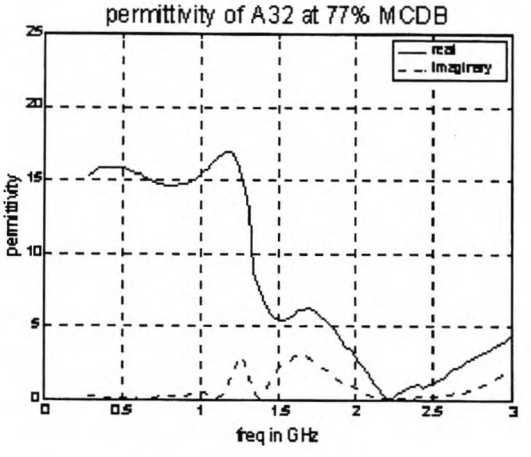

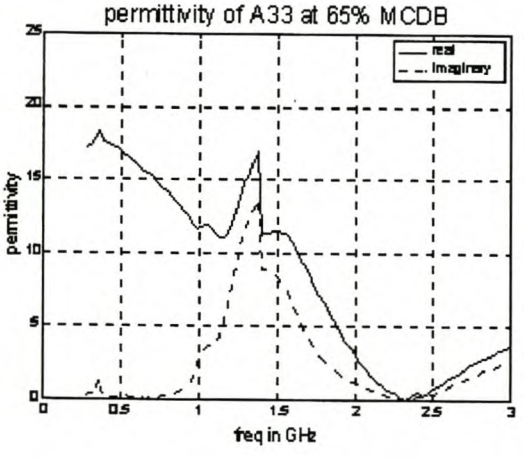

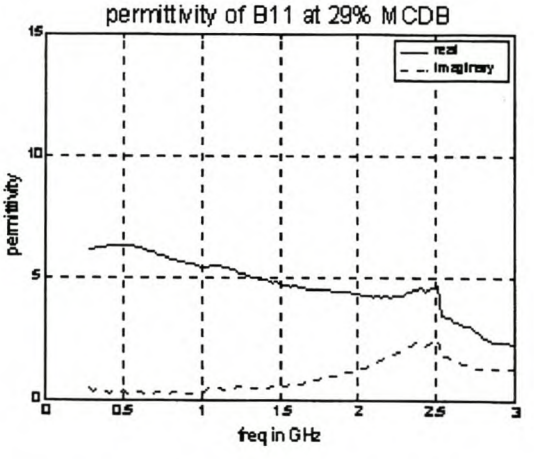

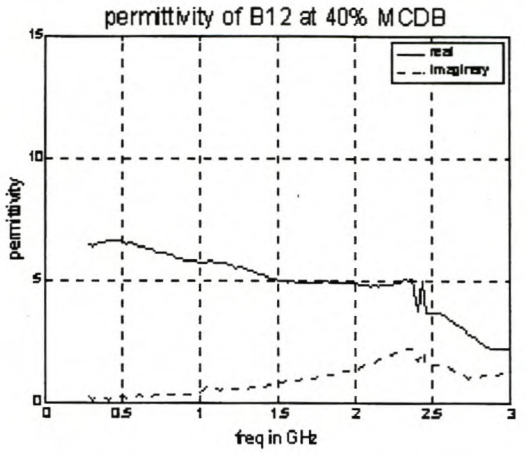

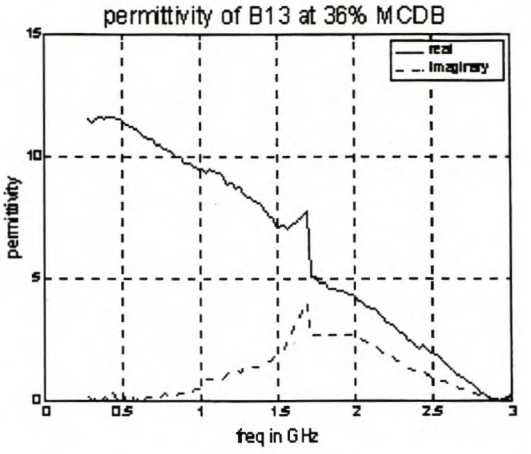

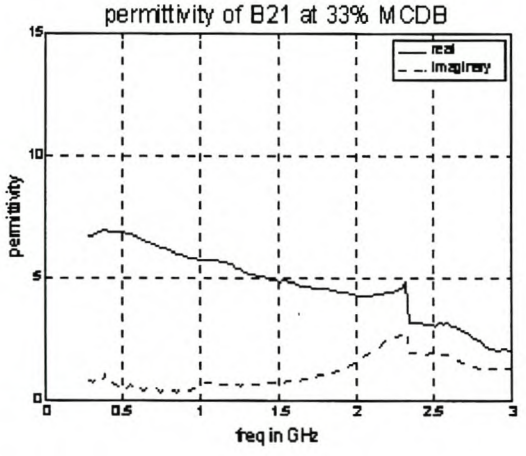

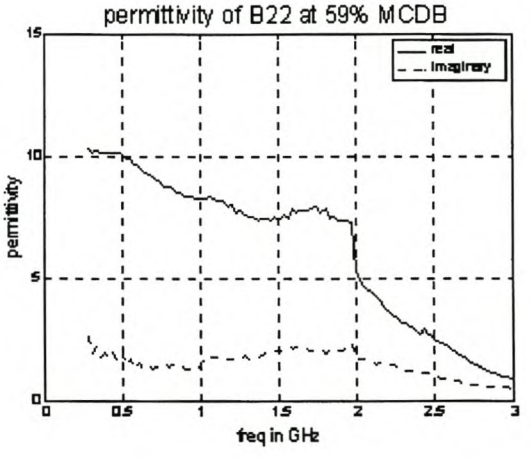

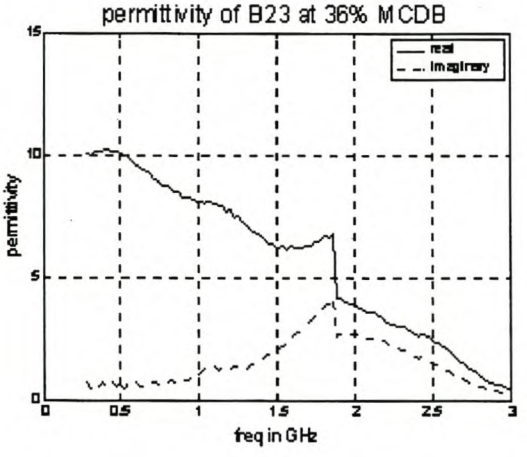

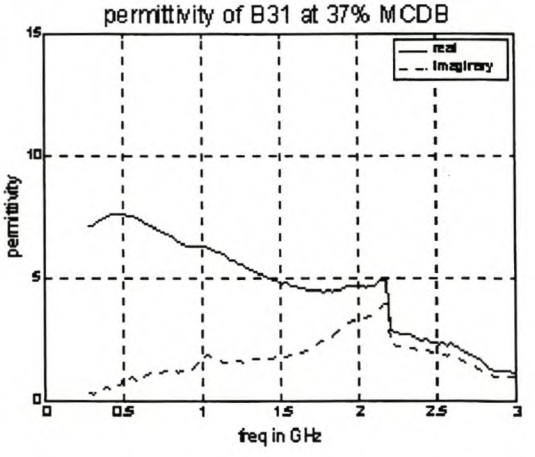

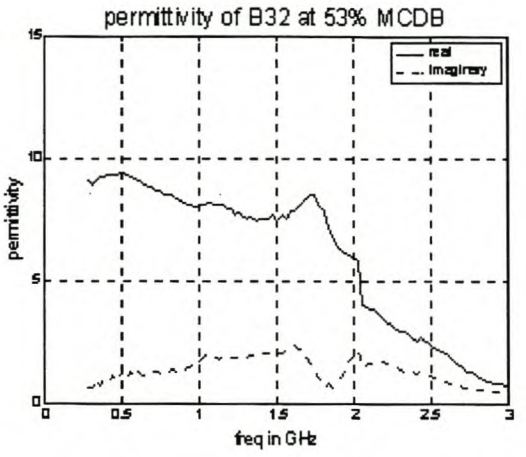

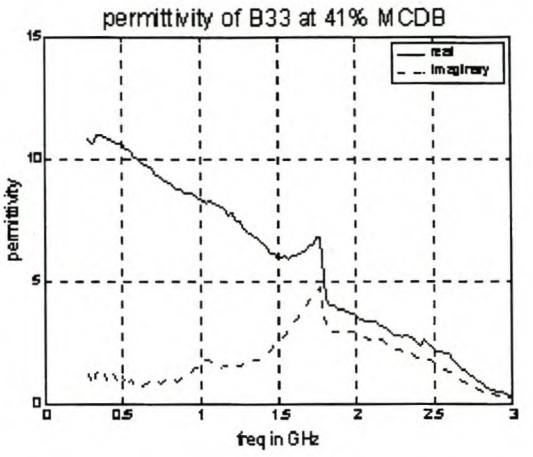

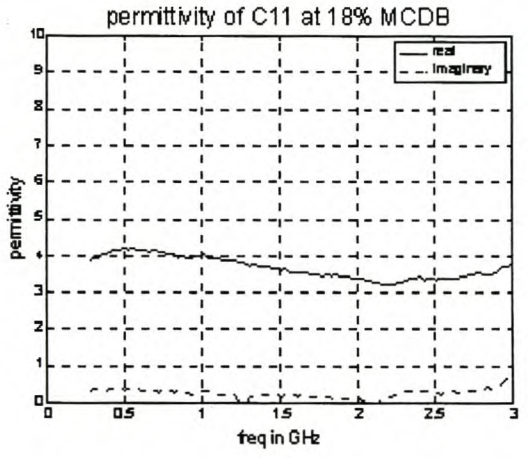

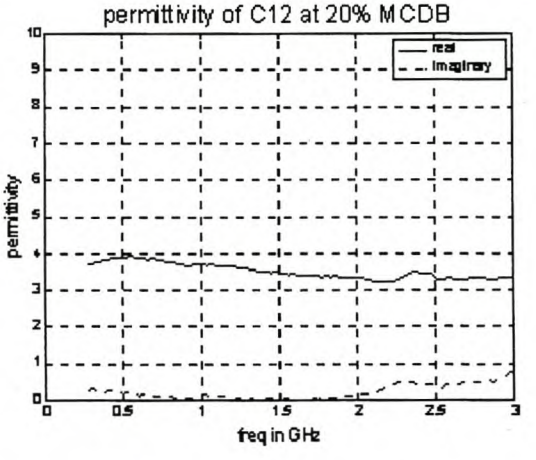

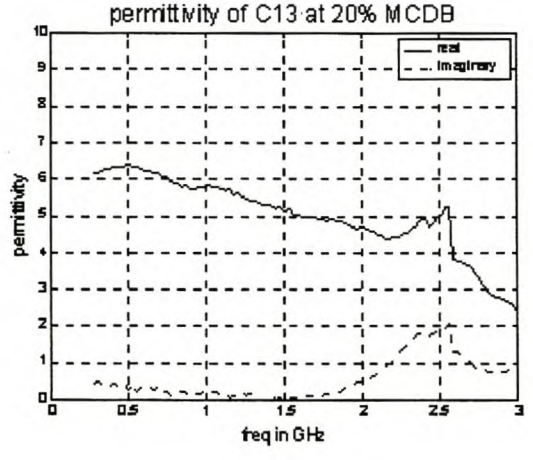

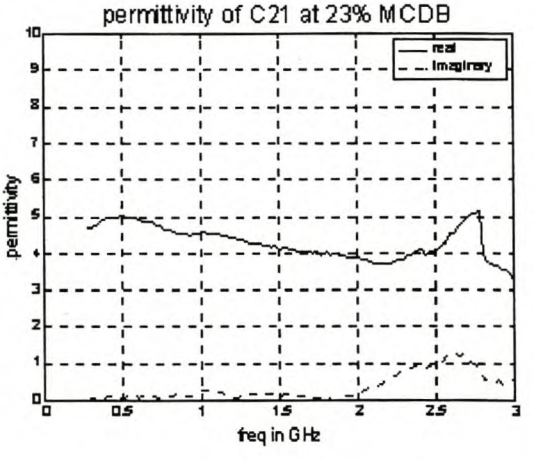

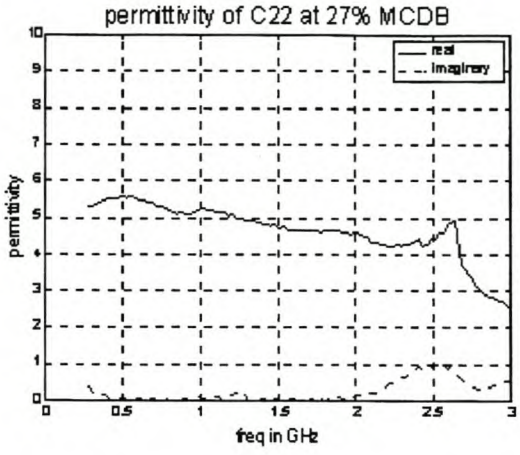

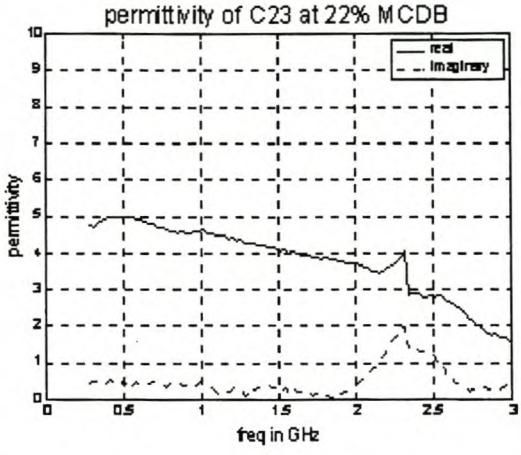

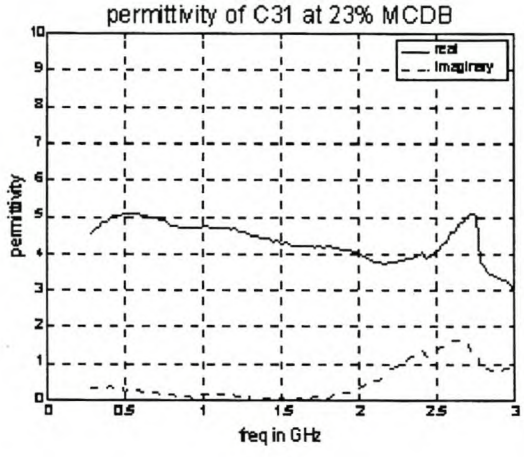

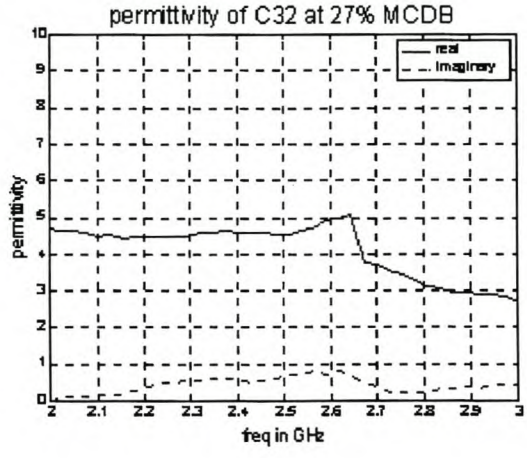

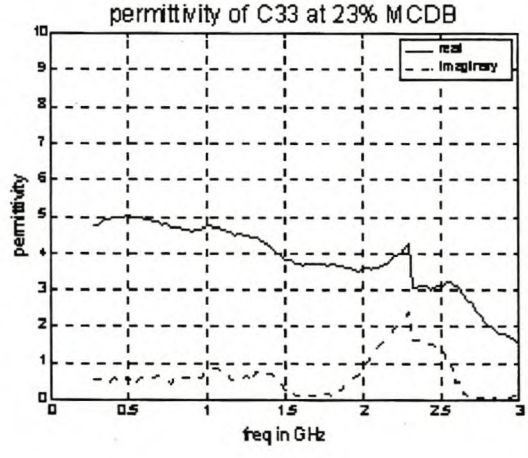

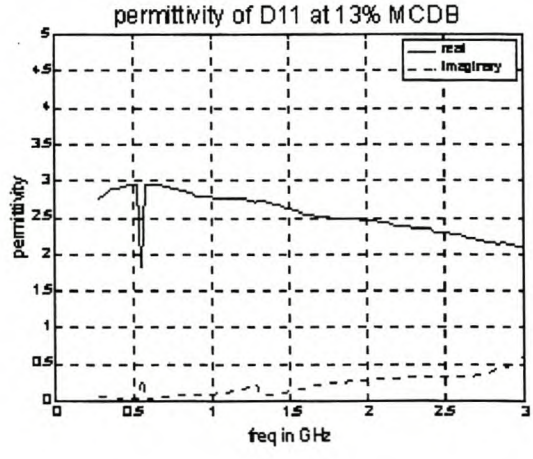

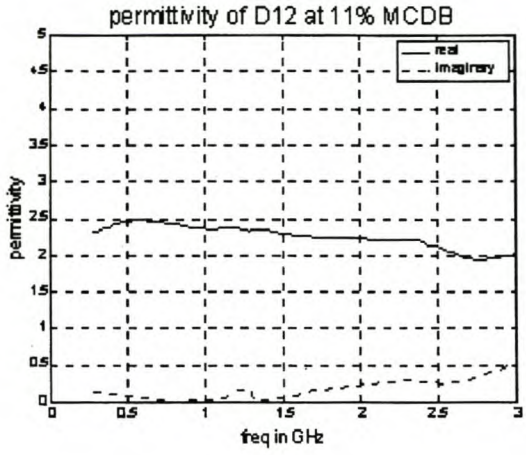

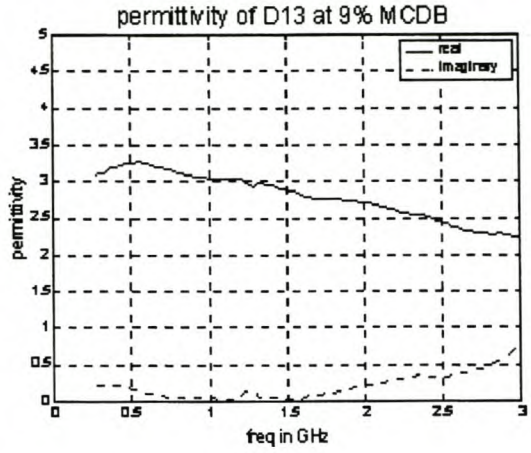

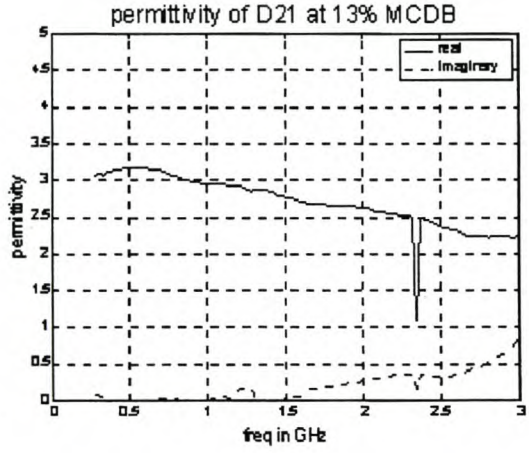

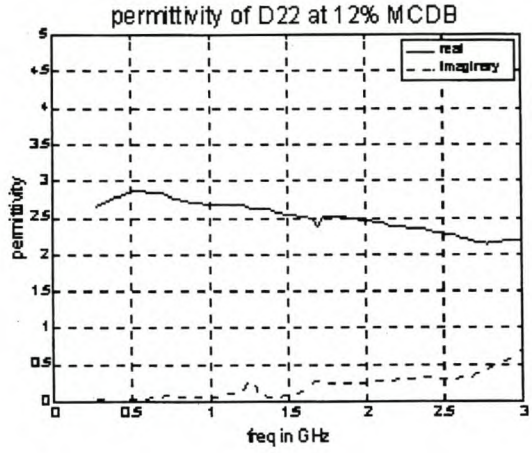

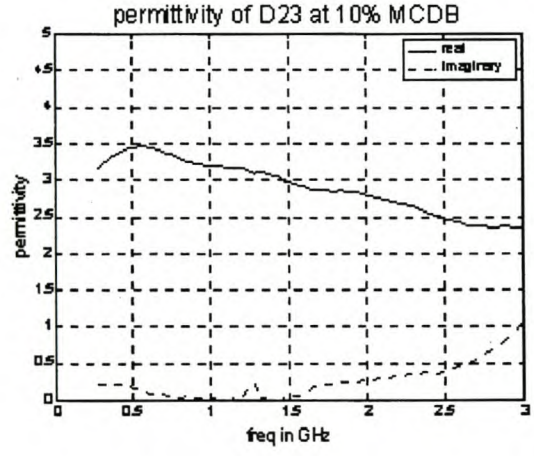

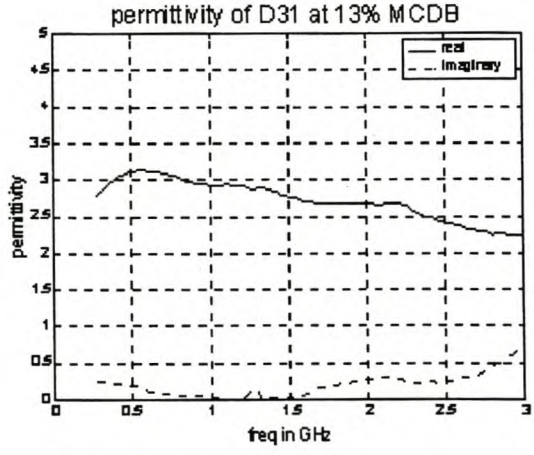

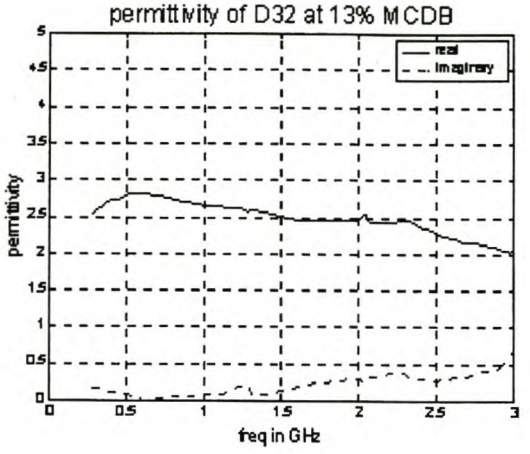

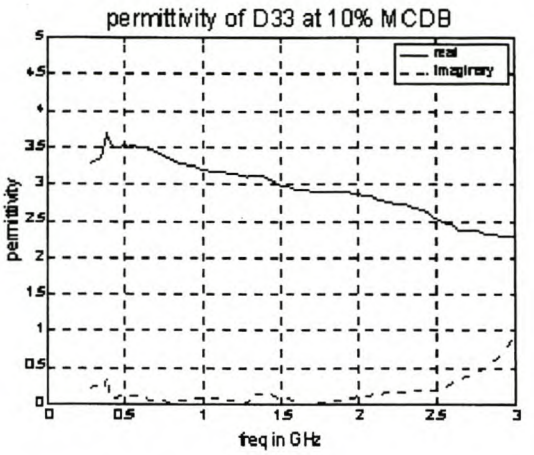

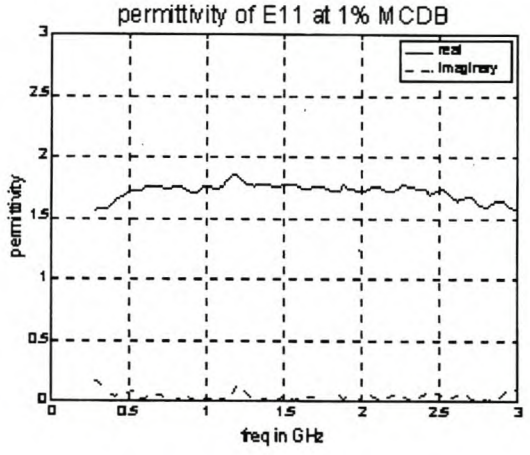

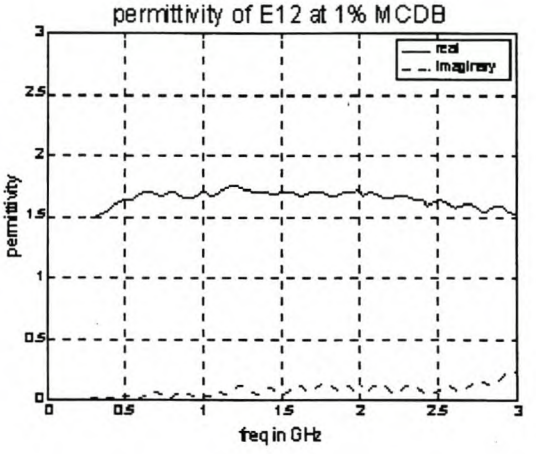

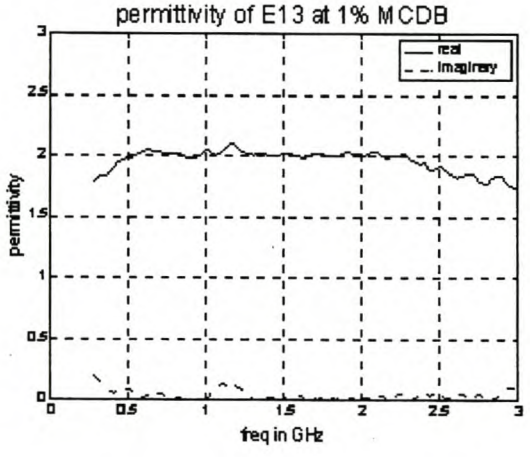

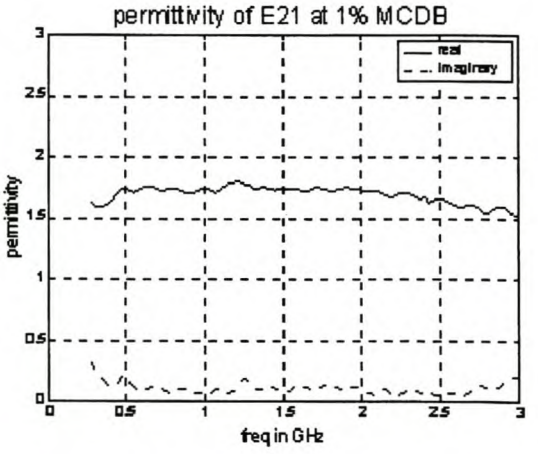

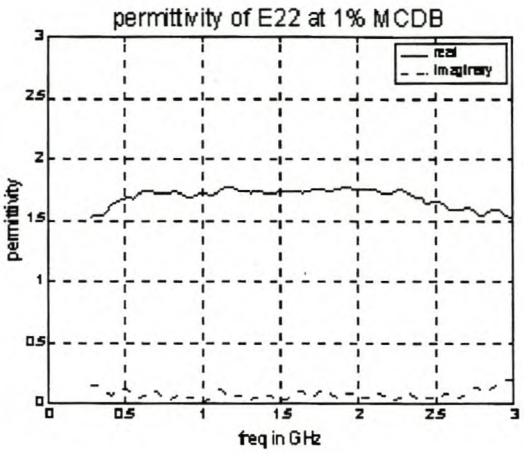

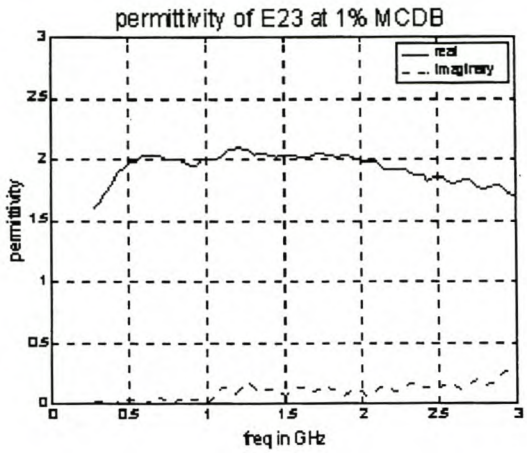

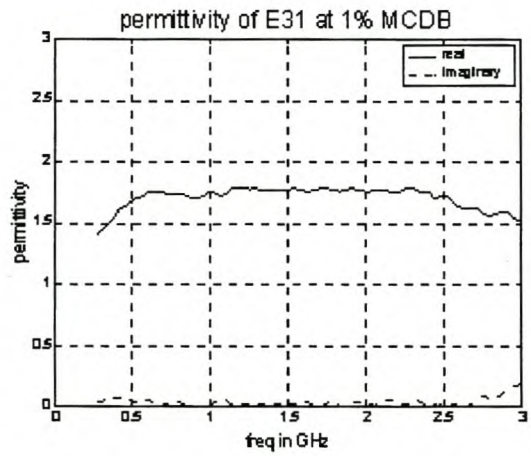

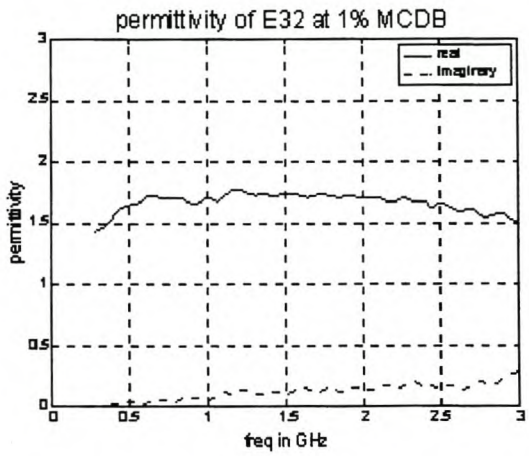

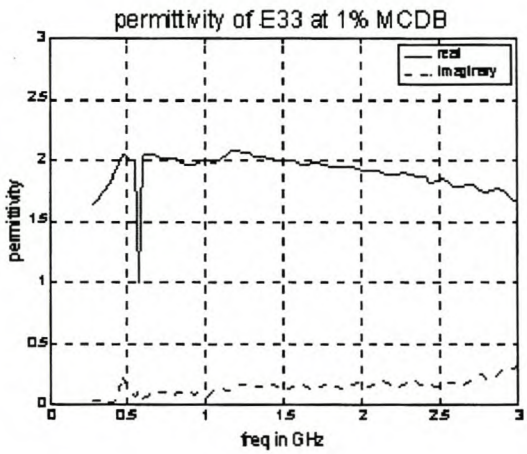

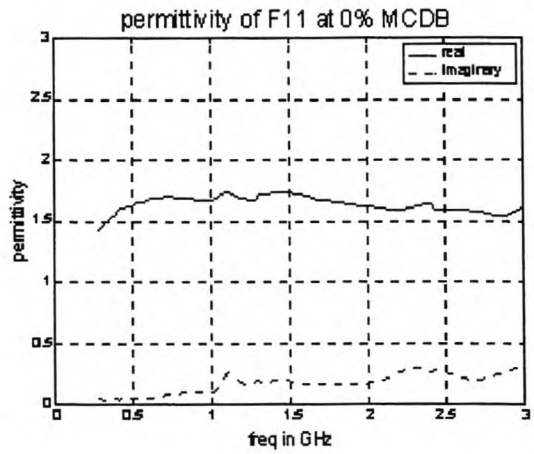

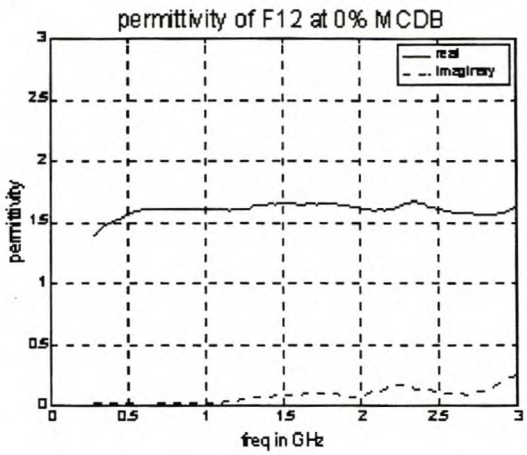

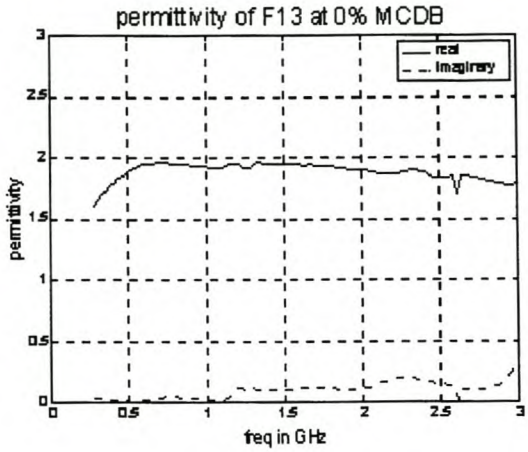

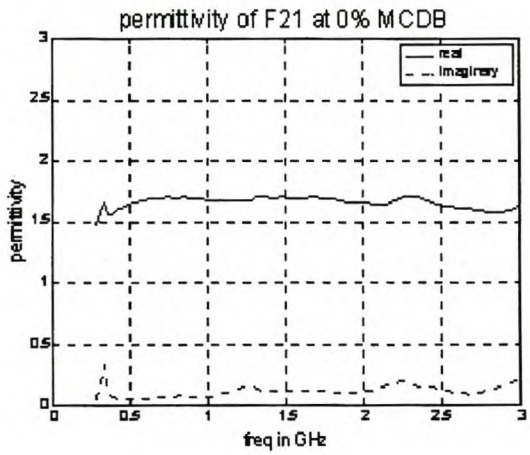

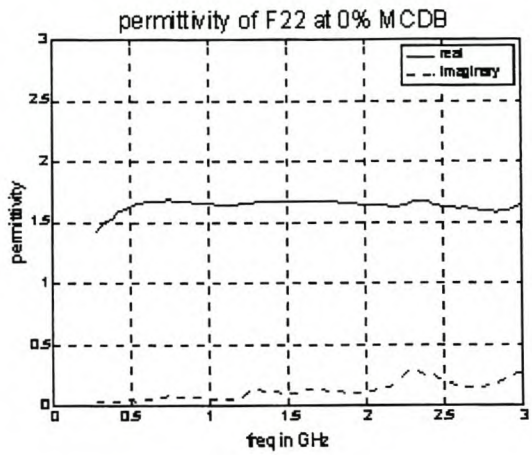

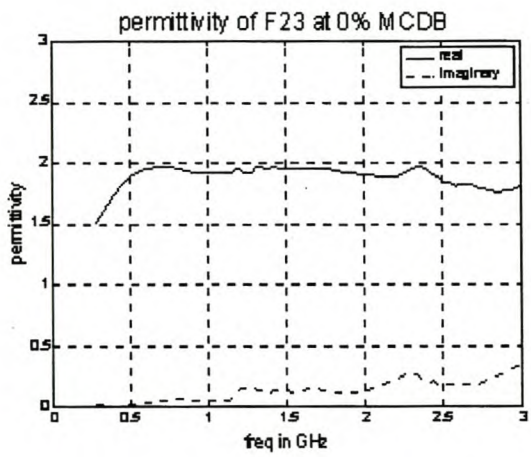

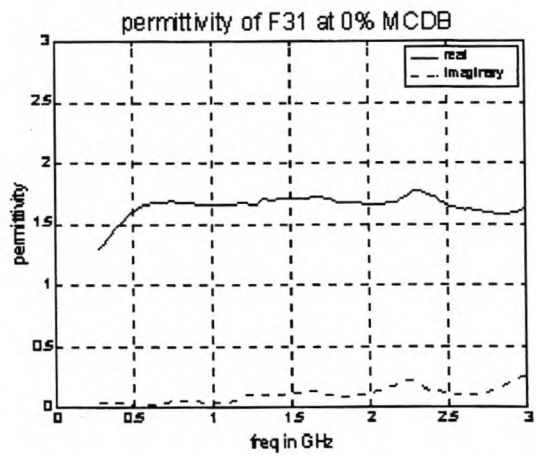

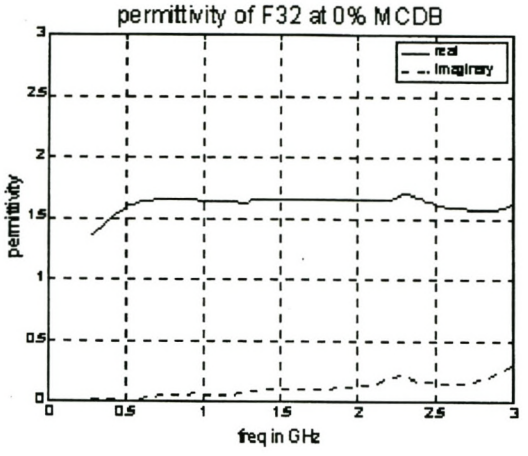

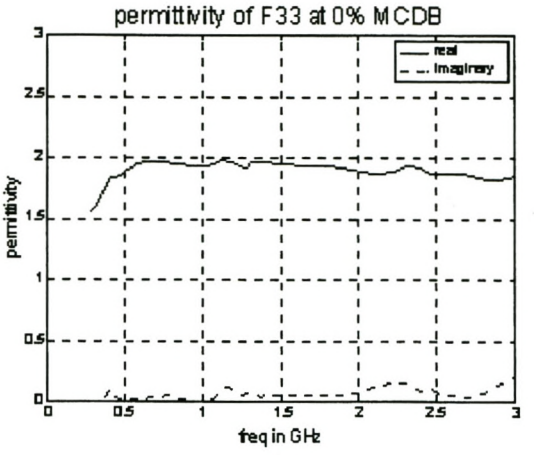

Appendix 5B

Simulated and Fax-paper Patterns for Drying Wood

5B.1 Introduction to Fax-paper patterns

Heat distribution (and therefore moisture content) in microwave heated wood has been mapped using fibre-optic thermometers inserted in holes drilled into the wood at selected points [79][88]. This process is destructive and it interferes with the heat distribution itself. Thermal imaging using an infra-red (IR) camera has been used as a non-invasive method [92]. In the absence of an IR camera, fax paper was proposed as an alternative.

5B.2 Fax-paper mapping method

The given times and steps described in the following method for obtaining fax-paper patterns are the result of experience obtained from several trial runs. The applicator described in Section 4.2 is used. The procedure used in this study is as follows:

- plank of green wood (510 × 110 × 40 mm, same dimensions as planks used in drying runs) is weighed and is positioned with the broadside (radial direction) parallel to the slots. Being parallel, the plank is equidistant from the slots along its entire length. The position of the plank is carefully marked within the applicator. The inside (side facing the slots that would be excited by a magnetron), the outside and the top of the plank are marked. The plank is then heated in the microwave applicator using one magnetron only and air at room temperature for 30 minutes. The air removes moisture from the applicator.
- with reference to section 4.3.1, the plank is allowed to cool to a temperature which does not affect the fax-paper. (Cooling time of 10 to 15 minutes was used. This time is not long enough for the water in the wood to equilibrate).
- fax-paper of the same length and width as the plank is placed on the outside of the plank with the active side against the wood and is tied into position using a cotton string.
- plank, with fax-paper tied, carefully placed on the marked position in the applicator with proper orientation maintained, is heated for exactly two minutes and is quickly removed.
- fax-paper is removed from the plank and is subsequently photographed. (Time is not an issue as the pattern does not change once fax-paper has been removed from the plank). The mass of the plank, however, is measured immediately.
- plank is heated again for 15 minutes and the procedure is repeated starting from the second step.

The mass of the plank measured just before and after fax-paper mapping is averaged. The average is taken as the mass of the plank at the time of mapping. The averaged mass is used to calculate the average moisture content on a dry basis.

Figures B1 to B5 is a series of the fax-paper patterns at different moisture contents on a dry basis

Figure B1 46 % MCDB

Figure B2 40 % MCDB

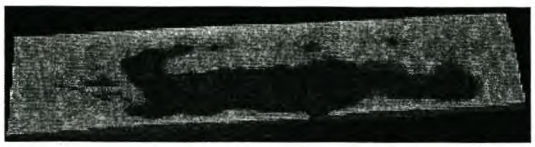

Figure B3 27 % MCDB

Figure B4 20 % MCDB

Figure B5 15 % MCDB

Figure B6 11 % MCDB

As mentioned in section 4.3.1, the black areas indicate regions of the plank with temperatures above 100 °C and white areas indicate temperatures below. The increasing black pattern (B1 -B6) indicates the decreasing moisture content and its increasingly uniform distribution.

5.B.3 Introduction to Simulated patterns

The Ansoft HFSS 7.0 FEM package is a commercial code which is widely used and has been perfected through a number of revisions. The FEM code has been tested against an analytical design of a slotted waveguide feed in Chapter 3. It was also used to generate the radiation pattern of the slotted waveguide feed. The pattern was compared with that cut in an antenna test facility. The similarity of the patterns is evident in Figures 3.16 and 3.17. Thus HFSS 7.0 was used with confidence to generate the electric field patterns in Figures B7 through B12. The wood model used in the simulations is of the same dimensions as the planks used in mapping fax paper patterns. The tensor dielectric properties of the wood have been carefully determined, as described in Section 5.4.1.

5B.4 Simulated Electric Field Patterns

The anisotropic material setup tensors for HFSS are 3×3 for both permittivity and electric loss tangent with diagonal entries. The tensor is shown below

$$\begin{pmatrix} diag[1] & 0 & 0 \\ 0 & diag[2] & 0 \\ 0 & 0 & diag[3] \end{pmatrix}$$

Dielectric properties of longitudinal, radial and tangential samples of approximately the same moisture content from the same locality were used to fill the tensors. The average moisture content of the samples was used as the moisture content of the plank for which dielectric properties are entered in the tensor. Diag[1] entries were taken from the longitudinal sample, diag[2] from the radial sample and diag[3] from the tangential sample. The simulated patterns are shown in Figures B7 through B12 for locality 2 sample set (i.e sample21, sample 22 and sample 23) and are to be compared with Figures B1 to B6.

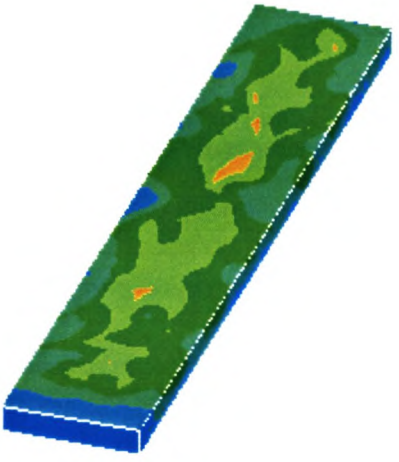

Figure B7 44% MCDB

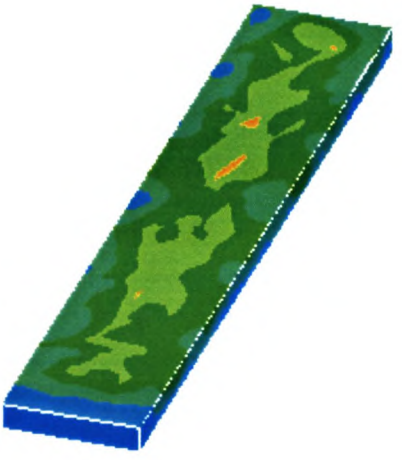

Figure B8 40% MCDB

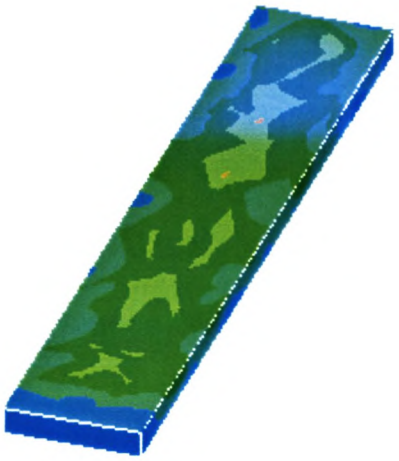

Figure B9 37% MCDB

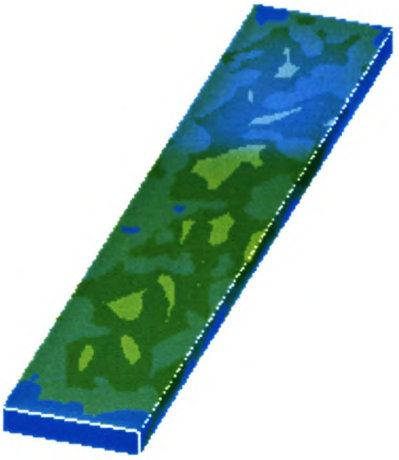

Figure B10 19% MCDB

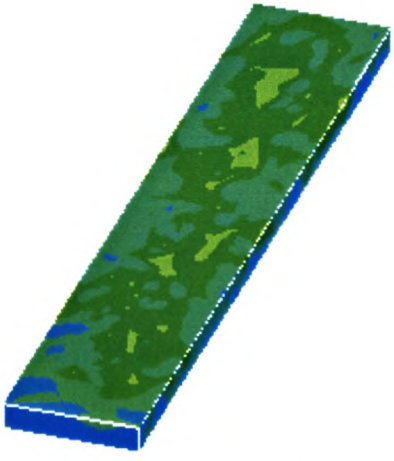

Figure B11 13% MCDB

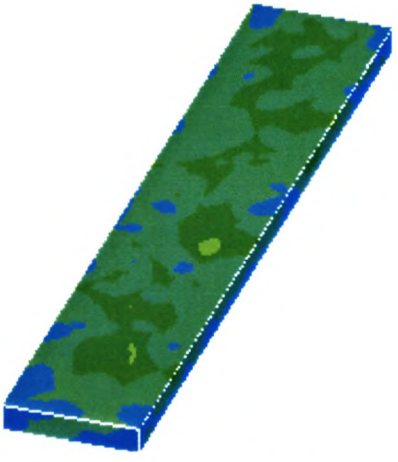

Figure B12 11% MCDB

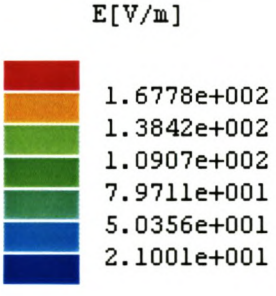

colour key

5B.5 Comparison of Fax-paper and Simulated Patterns

It is noted at the onset of this discussion that computational and fax-paper experiments are not tightly correlated. A number of reasons can be given for the lack of tight correlation. These include:

- it is not possible to derive identical MCDB through this procedure because moisture content cannot be determined precisely while the wood is being heated. That is, the plank for which the heating pattern is mapped with the fax-paper is not at the same moisture content as the samples from which the dielectric properties used in the simulation are taken. However, the MCDB used in the comparison are as close as practicable.
- each simulation run is static but a fax paper measurement is dynamic. In other words, moisture migration and temperature changes are not accounted for in simulations.
- the plank used with fax-paper is different from the one used to measure dielectric properties.
- the simulation assumes a linear device but wood heating is a non-linear process.
- the simulations are carried out at a fixed frequency of 2.45 GHz using a continuous wave but there is possibly 2 to 3 different weighted modal distributions excited in the applicator by the 2.45 ± 5% GHz magnetron.
- A number of processes separate the simulations and heating patterns. The simulations indicate the distribution of the electric component of the microwave field absorbed by the wood. The fax-paper patterns indicate the distribution of heated water coming out of the wood. The hot water comes out after the absorbed microwave energy has been converted into heat; the heat has been used to raise the temperature and change the state of water in the wood. The heat is also used to raise the temperature of the cellular and resin components of wood. In other words, some of the simulated field distribution information is lost in the intervening processes before detection by fax-paper.

However, the following can be deduced from figures B1 through B12:

- the blackened area of fax-paper increases as MCDB decreases (Fig B1-B6). Intensity of electric field increases and its uniformity increases as MCDB decreases (Fig B7-B12). Both trends show that at high MCDB, the moisture distribution in wood is not uniform but becomes progressively uniform as MCDB decreases.
- the starting points of the experiments (Fig B1 and B7) are correlatable.
- patterns at the end of the experiment (Fig B6 and B12) show striking similarities. This shows that when wood is at the lowest possible MCDB, the uniform distribution of moisture can be shown accurately through fax-paper and simulated patterns.

References

[1] J. Thu'ery, *Microwaves: Industrial, Scientific and Medical Applications*. Norwood, Artech House, 1992.

[2] C. Metaxas, R. Meredith, *Industrial Microwave Heating* Peter Peregrinus,(IEE) 1983.

[3] V. Raicu, "A simple theoretical and practical approach to measuring dielectric properties with an open-ended coaxial probe," *Meas. Sci. Technol.* vol 6 pp. 410-414, 1995.

[4] A.M.Nicolson, G.F Ross, " Measurement of the intrinsic properties of materials by time-domain techniques," *IEEE Transactions on instrumentation and measurement*, vol.IM-19, pp 377-382, Nov.1970.

[5] W.B.Weir, " Automatic measurement of complex dielectric constant and permeability at microwave frequencies," *Proceedings of the IEEE*, vol.62, pp 33-36, Jan. 1974.

[6] T.W. Athey, M.A. Stuchly, S.S Stuchly, " Measurement of radio frequency permittivity of biological tissues with an open-ended coaxial line: part 1," *IEEE Transactions on Microwave Theory and Techniques*, vol.MTT-30, pp 82-86, Jan.1982.

[7] M.A Stuchly, S.S Stuchly, " Coaxial line reflection methods for measuring dielectric properties of biological substances at radio and microwave frequencies - a review," *IEEE Transactions on instrumentation and measurement,* vol.IM-29 pp 176-183, Sept.1980.

[8] G. Turner, *The influence of subsurface properties on ground penetration radar pulses*. Ph.D Thesis, Macquire University, December, 1993.

[9] H.P. Schwan, *Physical Techniques in Biological Research*, vol VIB, Academic Press pp 323-407.

[10] J.P Grant, R.N. Clarke, G.T Symm, N.M Spyrou, " A critical study of the open-ended coaxial line sensor technique for RF and microwave complex permittivity measurements," *J.Phys. E. Sci. Instru.* 22, pp 757-770, 1989.

[11] G.P Otto, W.C. Chew, "Improved calibration of a large open-ended coaxial probe for dielectric measurements," *IEEE Transactions on Instrumentation and Measurement*, vol.IM-40, pp 742-746, Aug.1991.

[12] D.L Gershon, J.P. Calame, Y. Carmel, T.M. Antonsen, Jr., R.M Hutcheon, " Open-Ended coaxial probe for high-temperature and broad-band dielectric measurements," *IEEE Transactions on Microwave Theory and Techniques,* vol.47, pp 1640- 1648,Sept. 1999.

[13] M.R. Taherian, D.J. Yuen, T.M. Habashy, J.A. Kong, " A coaxial-circular waveguide for dielectric measurement," *IEEE Transactions on Geoscience and Remote Sensing*, vol.29, pp 321-329, Mar.1991.

[14] M.D. Deshpande, C.J. Reddy, P.I. Tiemsin, R. Cravey, " A new approach to estimate complex permittivity of dielectric materials at microwave frequencies using waveguide measurements," *IEEE Transactions on Microwave Theory and Techniques*, vol.45, pp 359-365, Mar.1997.

[15] W. Barry, "A broad-band, automated, stripline technique for the simultaneous measurement of complex permittivity and permeability," *IEEE Transactions on Microwave Theory and Techniques,* vol.MTT_34, pp 80-84, Jan.1986.

[16] G. Roussy, J.A. Pearce, *Foundations and Industrial Applications of Microwave and Radio Frequency Fields*. Chichester, John Wiley & Sons, 1995.

[17] Manual for the HP4285A Precision LCR meter, Hewlet Packard.

[18] D. Misra, M. Chabbra, B.R Epstein, M. Mirotznik, K.R. Foster, " Noninvasive electrical

characterization of materials at microwave frequencies using an open-ended coaxial line: test of an improved calibration technique", *IEEE Transactions on Microwave Theory and Techniques*, vol.38, pp 8-13, Jan. 1990.

[19] S. Evans, S.C Michelson, " Intercomparison of dielectric reference materials available for calibration of an open-ended probe at different temperatures", *Meas. Sci. Technol.* pp 1721-1732, 1995.

[20] J. Baker-Jarvis, M.D. Janezic, P.D Domich, R.G. Geyer, " Analysis of an open-ended coaxial probe with lift-off for nondestructive testing", *IEEE Transactions on Instrumentation and Measurement*, vol.43, pp 711-717, Oct. 1994.

[21] G.Q. Jiang, W.H. Wong, E.Y. Raskovich, W.G. Clark , W.A Hines, J. Sanny," Measurement of the microwave dielectric constant for low-loss samples with finite thickness using open-ended coaxial-line probes", *Rev. Sci. Instrum.*, vol.64, pp 1622-1626, Jun. 1993.

[22] G. Panariello, L. Verolino, G Vitolo, " The coaxial probe for permittivity measurements. An efficient and accurate full-wave analysis", *in Proc of the 7th International Conference on Microwave and High Frequency Heating* 1999, pp 125-128.

[23] N. Marcuvitz,Ed., *Waveguide Handbook*. London, Peter Peregrinus, 1986, pp 213-216.

[24] S. Bringhurst, M.F. Iskander, " Open-ended metallized ceramic coaxial probe for high-temperature dielectric properties measurement", *IEEE Transactions on Microwave Theory and Techniques*, vol.44, pp 926-935, Jun. 1996.

[25] M. Arai, J.G.P. Binner, T.E. Cross, " Estimating errors due to sample surface roughness in microwave complex measurements obtained using a coaxial probe", *Electronics Letters,* vol.31, pp 115-117, Jan. 1995.

[26] G.Q. Jiang, W.H. Wong, E.Y. Raskovich, W.G. Clark , W.A. Hines, J. Sanny, " Open-ended coaxial-line techniques for the measurement of the microwave dielectric constant for low-loss solids and liquids", *Rev. Sci. Instrum.*, vol.64, pp 1614-1621, June, 1993.

[27] C.A. Jones, Y.Kantor, J.H. Grosvenor, M.D. Janezic, " Stripline resonator for electromagnetic measurements of materials", NIST Technical Note 1505.

[28] G.W. Hanson, J.M. Grimm, D.P. Nyquist, " An improved de-embedding technique for the measurement of the complex constitutive parameters of materials using a stripline field applicator", *IEEE Transactions on Instrumentation and Measurement*, vol.42, pp 740-745, Jun. 1993.

[29] S.B. Cohn, " Problems in strip transmission lines", *I.R.E. Transactions of Microwave Theory and Techniques*, vol. MTT-3 , pp 119-126, Mar. 1955.

[30] D.M. Pozar, *Microwave Engineering*. 2nd ed.Crawfordsville, John Wiley & Sons, 1998.

[31] E.A. Wolf, R. Kaul, *Microwave Engineering and Systems Applications.* New York, John Wiley &Sons, 1988.

[32] "In-Fixture Measurements Using Vector Network Analyzers", Hewlet Packard, AN 1287-9.

[33] G. F. Engen, C.A. Hoer, " Thru-Reflect-Line: an improved technique for calibrating the dual six-port automatic network analyzer", *IEEE Transactions on Microwave Theory and Techniques*, vol.MTT-27, pp 987-993, Dec. 1979.

[34] Materials measurement. Measuring the dielectric constant of solids with the HP8510 network analyzer", Hewlet Packard, Product Note 8510-3.

[35] "Network Analysis. Applying the HP 8510B TRL calibration for non-coaxial measurements", Hewlet Packard, Product Note 8510-8.

[36] A. Boughriet, C. Lengrand, A. Chapoto, " Noninterative transmission / reflection method for low-loss material complex permittivity determination", *IEEE Transactions on Microwave Theory and Techniques,* vol.45, pp 52-57, Jan.1997.

[37] A.G. Smith, *An Experimental Study of Artificial Isotropic Chiral Media at Microwave frequencies*. Ph.D Thesis, University of Stellenbosch, 1994.

[38] I.P. Theron, *Baker-Jarvis inversion algorithm for free-space measurement system.* Internal Report.Dept. of Electrical and Electronic Engineering, University of Stellenbosch, June, 1996.

[39] R. Meredith, *Engineers' Handbook of Industrial Microwave Heating.* London, The Institute of Electrical Engineers, 1998.

[40] H. Howe,Jr., *Stripline Circuit Design.* Dedham, Artech House, 1974.

[41] S.B. Cohn, "Characteristic impedance of the shielded - strip transmission line," *Trans. IEEE, MTT-2, pp 52 - 55, July, 1954.*

[42] H.Zhang, A.K. Datta, "Coupled Electromagnetic and Thermal Modeling of Microwave Oven Heating of Foods. *Journal of Microwave Power and Electromagnetic Energy*, Vol.35, No.2, pp 71-85", 2 000.

[43] A.R. Von Hippel, *Dielectric Materials and Applications*, Cambridge, Mass. M.I.T Press, 1954.

[44] Circuit Magnification Meter, TF 1245 (series), Instruction Manual. Marconi Instruments Limited.

[45] A.C.Bajpai, I.M.Calus, J.A.Fairley, *Numerical Methods for Engineers and Scientists: A Student's Course Book. London,* Taylor & Francis Ltd, 1975

[46] J.Barker-Jarvis, E.J.Vanzura, W.A.Kissick, "Improved Technique for Determining Complex Permittivity with the Transmission / Reflection Method", *IEEE Transactions on Microwave Theory and Techniques*, vol.38, pp 1096-1103, August, 1990.

[47] J.B. Salsman, "Measurement of Dielectric properties in the frequency range of 300 MHz to 3 GHz as a function of temperature and density", pp 203-214 in *Ceramic Transactions; Microwaves: Theory and Applications in Material Processing,* vol.21, Edited by D.E. Clark, F.D Gac and W.H. Sutton. Westerville, The American Ceramic Society, Inc.

[48] J. Baker-Jarvis, C. Jones, B. Riddle, M. Janezic, R.G. Geyer, J.H. Grosvenor, Jr., and C.M. Weil, "Dielectric and Magnetic Measurements: A Survey of Nondestructive, Quasi-Nondestructive, and Process-Control Techniques", *Res Nondestr Eval*, vol. 7, pp 117-136, 1995.

[49] R.S. Elliott, L.A Kurtz, "The Design of Small Slot Arrays", *IEEE Transactions on Antennas and Propagation*, vol.AP-26, No.2, pp 214-219, March, 1978.

[50] R.S. Elliott, "On the Design of Travelling-Wave-Fed Longitudinal Shunt Slot Arrays", *IEEE Transactions on Antennas and Propagation*, vol.AP-27, No.5, pp 717-720, September, 1979

[51] R.S. Elliott, *Antenna Theory and Design*, Englewood Cliffs, Prenice-Hall, Inc., 1981.

[52] R.S. Elliott, "An Improved Design Procedure for Small Arrays of Shunt Slots", *IEEE Transactions on Antennas and Propagation*, vol.AP-31, No.1, pp 48-53, January, 1983

[53] R.E. Collin, *Antennas and Radiowave Propagation*, New York, McGraw-Hill, 1985.

[54] T.A. Milligan, *Modern Antenna Design,* New York, McGraw-Hill, 1985.

[55] C.A. Balanis, *Antenna Theory: Analysis and Design*, New York, Harper & Row, 1982.

[56] S.B. Cohn, "Microwave Coupling by Large Apertures", Proceedings of the I.R.E., pp

696-699, June, 1952.

[57] S. Silver, *Microwave Antenna Theory and Design*, New York, McGraw-Hill, 1949.

[58] E.C. Jordan, K.G. Balmain, *Electromagnetic Waves and Radiating Systems,* 2nd ed.,Englewood Cliffs, Prentice-Hall, Inc., 1968.

[59] W.R. Stutzman, G.A. Thiele, *Antenna Theory and Design*, 2nd ed. New York, John Wiley & Sons, Inc., 1998.

[60] M.N.O. Sadiku, *Numerical Techniques in Electromagnetics*, Boca Raton, CRC Press, 1992.

[61] HFSS 7.0, Online Manual, Ansoft Corporation.

[62] P.P. Silvester, G. Pelosi, *Finite Elements for Wave Electromagnetics*, New York, IEEE Press, 1994.

[63] E.T. Thostenson, T.W. Chou, "Microwave Processing: Fundamentals and Applications",*Composites:* Part A 30, pp 1055-1071, 1999.

[64] J.R. Bows, M.L. Patrick, R. Janes, A.C. Metaxas, D.C. Dibben, "Microwave Phase Control Heating", *International Journal of Food Science and Technology*, vol. 34, pp 295-304, 1999.

[65] X. Jia, P. Jolly, "Simulation of Microwave Field and Power Distribution in a Cavity by a Three-Dimensional Finite Element Method", *Journal of Microwave Power and Electromagnetic Energy*, vol. 27, No. 1, 1992.

[66] X. Jia, "Experimental and Numerical Study of Microwave Power Distribution in a Microwave Heating Applicator", *Journal of Microwave Power and Electromagnetic Energy*, vol. 28, No. 1, 1993

[67] A.C. Johnson, R.J. Espinosa, W.A. Lewis, L.T.Thigpen, C.A. Everleigh, R.S. Garard, "Use of a Variable Frequency Microwave Furnace for Large-are, Uniform Processing", *Ceramic Transactions 36; Microwaves: Theory and Application in Materials Processing II,* pp 563-570.

[68] T.V.C.T. Chan, *Analytical, Experimental and Numerical Studies of Fields in Resonant Cavities for Microwave Dielectric Heating*, PhD thesis, University of Stellenbosch, 1998.

[69] W. Fu, A. Metaxas, "Numerical Prediction of Three-Dimensional Power Density Distribution in a Multi-Mode Cavity", *Journal of Microwave Power and Electromagnetic Energy*, vol. 29, No. 2, 1994.

[70] J.M. Osepchuk, "A History of Microwave Heating Applications", *IEEE Transactions on Microwave Theory and Techniques*, vol.32, No. 9, pp 1200-1223, September, 1984.

[71] C.A.W. Vale, P. Meyer, "A Design Technique for Co-existing Multimode Waveguide Bandstop Filters", *IEEE MTT-S Int. Microwave Symp.*, Boston, MA., pp 1189-1192, June 11-16, 2000.

[72] M.R. Milota, "Drying Wood: The Past, Present and Future", *Proceedings 6th IUFRO Wood Drying Conference*, University of Stellenbosch, pp 1-10, January 25-28, 1999.

[73] J.F. Siau, *Wood: Influence of Moisture on Physical Properties*, Virginia Polytechnic Institute and State University, 1995.

[74] J.R. Olson, S.J. Chang, P.C. Wang, "NMR Imaging of Moisture Flow in White Oak Rays", *IUFRO Wood Drying Symposium*, Seattle, pp 59-63, July 23-28, 1989.

[75] P. Perre, "Image Analysis, Homogenization, Numerical Simulation and Experiment as Complementary Tools to Enlighten the Relationship Between Wood Anatomy and Drying Behavior", *Drying Technology*, vol.15, No. 9, pp 2211-2238, 1997.

[76] F. Kayihan, "Moisture Movement", *IUFRO Wood Drying Symposium*, Seattle, pp 255-

268, July 23-28, 1989.

[77] R.J. Barbour, J.A. Johnson, "Microstructurally Based Model for Moisture Movement in Wood Below the Fibre Saturation Point", *IUFRO Wood Drying Symposium*, Seattle, pp 247-254, July 23-28, 1989.

[78] J.F. Siau, *Transport Processes in Wood*, Berlin, Springer-Verlag, 1984.

[79] H. Zhao, I.W. Turner, "The Use of a Coupled Computational Model for Studying the Microwave Heating of Wood", *Applied Mathematics Modelling*, vol. 24, pp 183-197, 2000.

[80] I.W. Turner, P. Perre, "A 3D Version of TransPore: A Comprehensive Heat and Mass Transfer Computational Model for Simulating the Drying of Wood", *Proceedings 6th IUFRO Wood Drying Conference*, University of Stellenbosch, pp 213-222, January 25-28, 1999.

[81] P. Perre, I.W. Turner, "Microwave Drying od Softwood in an Oversized Waveguide: Theory and Experiment", AIChE Journal, vol.43, No.10, October, 1997.

[82] H. Zhao, I. Turner, G. Torgovnikov, "An Experimental and Numerical Investigation of the Microwave Heating of Wood", *Journal of Microwave Power and Electromagnetic Energy*, vol. 33, No. 2, 1998.

[83] A.R. Von Hippel, *Dielectrics and Waves*, London, Artech House, 1995.

[84] J.C. Anderson, *Dielectrics*, London, Chapman and Hall Ltd., 1964.

[85] G.I. Torgovnikov, *Dielectric Properties of Wood and Wood-Based Materials*, Berlin, Springer-Verlag, 1993.

[86] C. Skaar, *Wood-Water Relations*, Berlin, Springer-Verlag, 1988.

[87] A.C. Lynch, S. Evans, "The Numerical Relationship between Permittivity and Loss Tangent" EMMA-Club: Technical Note No.1, April, 1998.

[88] M. Lehne, G.W. Barton, T.A.G. Langrish, "Comparison of Experimental and Modelling Studies for the Microwave Drying of Ironbark Timber", *Drying Technology*, vol.17, No. 10, pp 2219-2235, 1999.

[89] S. Avramidis, R.L. Zwick, J.B. Neilson, "Commercial-Scale RF/V Drying of Softwood Lumber. Part 1. Basic Kiln Design Considerations", *Forest Products Journal*, vol.46, No.5, May, 1996.

[90] S. Avramidis, R.L. Zwick, "Commercial-Scale RF/V Drying of Softwood Lumber. Part 2. Drying Characteristics and Lumber Quality", *Forest Products Journal*, vol.46, No.6, June, 1996.

[91] S. Avramidis, R.L. Zwick, "Commercial-Scale RF/V Drying of Softwood Lumber. Part 3. Energy Consumption and Economics", *Forest Products Journal*, vol.47, No1, January, 1997.

[92] A.L. Antti, H. Zhao, I. Turner, "An Investigation of the Heating of Wood in an Industrial Microwave Applicator: Theory and Practice", *Proceedings 6th IUFRO Wood Drying Conference*, University of Stellenbosch, pp 11-17, January 25-28, 1999.

[93] T.V.C.T. Chan, H.C Reader, *Understanding Microwave Heating Cavities*, Norwood, Artech House, 2000.

[94] M.A. Stuchly, T.W. Athey, G.M. Samaras, G.E.Taylor, T.W. Athey, M.A. Stuchly, S.S Stuchly, " Measurement of radio frequency permittivity of biological tissues with an open-ended coaxial line: part 11," *IEEE Transactions on Microwave Theory and Techniques*, vol.MTT-30, pp 87-91, Jan.1982.

[95] "Specifying Calibration Standards for the Agilent 8510 Network Analyser", Agilent

Technologies, Product Note 8510-5B.

[96] J.V. Quagliano, *Chemistry*, Englewood Cliffs, Prentice-Hall, Inc., 1958.

[97] C.A.W. Vale, *Growth-based Computer-aided Design Strategies for Multi-mode Waveguide Design with the Aid of Functional Blocks.* Ph.D Thesis, University of Stellenbosch, 2001.